

**Remote Electrostatic Potential Determination for  
Spacecraft Relative Motion Control**

by

**K. T. H. Wilson**

B.S., University of Florida, 2016

M.S., University of Colorado Boulder, 2019

A thesis submitted to the  
Faculty of the Graduate School of the  
University of Colorado in partial fulfillment  
of the requirements for the degree of  
Doctor of Philosophy  
Department of Aerospace Engineering Sciences  
2021

Committee Members:

Prof. Hanspeter Schaub

Prof. Jay McMahon

Prof. Zoltan Sternovsky

Prof. Robert Marshall

Prof. JR Dennison

Wilson, K. T. H. (Ph.D., Aerospace Engineering Sciences)

Remote Electrostatic Potential Determination for Spacecraft Relative Motion Control

Thesis directed by Prof. Hanspeter Schaub

While spacecraft charging has been an actively studied and managed result of spaceflight for decades, the advent of robotic servicing missions in high earth orbits prone to severe charging has opened new avenues of research. Servicing missions are already operating at GEO to extend the life of fuel depleted telecommunications satellites, while a surge of LEO launch capability motivates a need for orbital transfer vehicles and other in-orbit services requiring rendezvous.

Many nascent concepts for formation flying and debris remediation rely on electrostatic interactions to exert forces and torques on nearby objects without requiring physical contact. These concepts include Coulomb formations for propellant-less formation configuration and the Electrostatic Tractor, which utilizes electrostatic interactions to detumble and re-orbit large debris from distances of tens of meters. While a range of established technologies allow a spacecraft to measure its own electrostatic potential, all of these architectures additionally require knowledge of another body's potential. An enabling technology for these missions is therefore the development of a technique for sensing electrostatic potentials remotely.

This thesis establishes a promising method for remote electrostatic potential determination, through theoretical analysis and experimentation. Energetic electrons interacting with a surface result in the emission of x-rays, and analysis of this x-ray spectrum provides information about the incident electron energy and the surface elemental composition. If the electron source energy is known, either from an electron beam on a servicing craft or the ambient plasma, the relative potential between the spacecraft is determined. Experimental trials in the ECLIPS space environment simulation facility shows that this method is robust to incidence angles and target orientation, providing accuracies within tens of volts. Such performance enables electrostatic actuation concepts, and can also be used to monitor relative spacecraft potentials during rendezvous to mitigate arcing

threats.

In addition, the second part of this thesis explores the impact of electrostatic charging on proximity operations in high earth orbit, an increasingly popular field of operations. During rendezvous, multi-kV level electrostatic charges can impart torques on both servicer and target on the order of 10 mN-m. When approaching a disabled vehicle or debris object, these torques can accumulate to rotational rates in excess of  $1^\circ/\text{s}$ . Two guidance policies are introduced to generate approach trajectories that minimize the electrostatic perturbation, one based on a pseudospectral collocation optimized trajectory scheme that can be precomputed on the ground and the other a deterministic sampling-based approach that could be implemented onboard.

The results of this work are a significant contribution for many high earth orbit missions, as an enabling technology in improving rendezvous safety in cislunar space to touchless reorbiting and detumbling of hazardous debris objects.

## Dedication

To Toph, and Archer, for always knowing when I need a distraction, and Josh, for keeping me on track the rest of the time.

## Acknowledgements

I owe an enormous thank you to my advisor, Dr. Hanspeter Schaub, for taking me on as a student, nurturing my interest in arcane and varied topics, and pushing me to achieve at a level I had never thought possible. His guidance, teaching and encouragement carried me throughout graduate school, and will continue to carry me throughout my career.

Likewise, Dr. JR Dennison has been an invaluable resource to our group in developing chamber experiments. As the saying goes, an hour in the library can save a week in the lab, but a 20 minute conversation with Dr. Dennison can avoid weeks of mistakes and open up 5 new experimental questions at the same time. Thanks also to my committee, Dr. Zoltan Sternovsky, Dr. Robert Marshall and Dr. Jay McMahan, as great sources of guidance and knowledge.

From my earliest days, my parents have cultivated and encouraged my interests, and supported me through the decades of school that followed, and I am grateful for all they have done.

Thank you to the members of the AVS Lab and CCAR. Working and skiing alongside brilliant researchers of such diverse fields and backgrounds has been incredibly motivating, inspiring, and fun. Particular thanks go to Dr. Miles Bengtson, who has always been available to bounce ideas off as we developed complimentary sensing methods and invented a novel electron gun. Likewise, thank you to Alvaro Romero-Calvo and Julian Hammerl for being excellent lab mates, enabling rapid progress on thorny research topics.

Finally, I need to thank Josh, as an amazing support over the years. From taking a leap to Colorado with me, to making dinners and walking our dogs during late nights of paper writing, he has been a constant source of encouragement that has made this work vastly more enjoyable.

## Contents

<b>Chapter</b>	<b></b>
<b>1</b>	<b>Introduction</b> <span style="float: right;"><b>1</b></span>
1.1	Motivation . . . . . 1
1.2	Spacecraft charging and potential sensing . . . . . 3
1.2.1	Space environment and spacecraft charging . . . . . 3
1.2.2	Frequency of severe charging . . . . . 5
1.2.3	Spacecraft potential sensing . . . . . 7
1.2.4	Chamber overview . . . . . 10
1.3	Spacecraft proximity operations . . . . . 11
1.3.1	Servicing overview . . . . . 11
1.3.2	Prior charged proximity operations concepts . . . . . 12
1.3.3	Electrostatic force and torque modeling . . . . . 16
1.4	Contributions of this work . . . . . 17
<b>2</b>	<b>Fundamentals of Potential Sensing and Electrostatic Force Modeling</b> <span style="float: right;"><b>19</b></span>
2.1	Sensing requirements . . . . . 20
2.2	X-ray spectroscopic potential determination fundamentals . . . . . 21
2.2.1	X-ray emission from electron interactions . . . . . 21
2.2.2	Simulating x-ray spectra . . . . . 23
2.3	Multi-Sphere Method For Electrostatic Force And Torque Evaluation . . . . . 27

2.3.1	Multi-Sphere Model Development . . . . .	27
2.3.2	Spacecraft Models . . . . .	31
2.4	Conclusions . . . . .	33
<b>3</b>	<b>Experimental validation</b>	<b>34</b>
3.1	Chamber facility development . . . . .	34
3.1.1	Broad spectrum electron gun . . . . .	37
3.1.2	Probes . . . . .	42
3.1.3	Motion stages . . . . .	47
3.1.4	Power systems . . . . .	47
3.2	Bremsstrahlung-based potential sensing tests . . . . .	49
3.2.1	Data processing . . . . .	51
3.2.2	Rotating detector tests . . . . .	54
3.2.3	Rotating plate . . . . .	61
3.3	Conclusions . . . . .	63
<b>4</b>	<b>Remote electrostatic potential sensing in the high earth orbit x-ray environment</b>	<b>64</b>
4.1	Prior observations of environmentally induced x-rays . . . . .	64
4.2	Ambient plasma-induced x-rays . . . . .	65
4.3	Passive sensing of electrostatic potentials . . . . .	68
4.3.1	Theory . . . . .	68
4.3.2	Experimental validation of passive sensing . . . . .	70
4.4	Solar x-ray contribution . . . . .	75
4.5	Spectrum with environmental noise contributions . . . . .	77
4.6	Radiation effects within detector . . . . .	78
4.6.1	Electron trajectories in detector . . . . .	78
4.6.2	Energy deposition analysis . . . . .	79
4.6.3	Comparison to analysis in other missions . . . . .	82

4.7	Debris sensing SSA applications . . . . .	84
4.8	Conclusions . . . . .	85
<b>5</b>	<b>Comparison and fusion of methods for remote potential sensing</b>	<b>86</b>
5.1	Overview of electron spectroscopic potential determination method . . . . .	86
5.2	Comparison of touchless potential sensing methods . . . . .	89
5.3	Fusion of potential sensing methods . . . . .	93
5.4	Simulation of spacecraft servicing scenario . . . . .	96
5.4.1	Electron signal analysis . . . . .	96
5.4.2	X-Ray signal analysis . . . . .	101
5.5	Conclusion . . . . .	103
<b>6</b>	<b>Impact of Electrostatic Perturbations on Proximity Operations in High Earth Orbits</b>	<b>105</b>
6.1	Problem formulation . . . . .	105
6.2	Charged Proximity Operations Study . . . . .	107
6.2.1	Electrostatic force and torque magnitudes . . . . .	108
6.2.2	Other Perturbations . . . . .	111
6.2.3	Comparison to Solar Radiation Pressure . . . . .	112
6.2.4	Perturbed Station Keeping . . . . .	113
6.2.5	Servicer attitude control requirements . . . . .	117
6.3	Rendezvous example . . . . .	118
6.4	Conclusions . . . . .	120
<b>7</b>	<b>Constrained guidance for spacecraft proximity operations under electrostatic perturbations</b>	<b>122</b>
7.1	Motivation . . . . .	122
7.2	Problem scenario . . . . .	122
7.3	Dynamic sensitivity to estimated potential and range . . . . .	123
7.4	Control . . . . .	127

7.4.1	System frames . . . . .	127
7.4.2	Translational control . . . . .	128
7.4.3	Attitude control . . . . .	130
7.5	Guidance . . . . .	131
7.5.1	Deterministic translational guidance . . . . .	132
7.5.2	Deterministic attitude guidance . . . . .	136
7.5.3	Simulation results . . . . .	138
7.6	Optimized guidance approach . . . . .	141
7.6.1	Trajectory parameterization . . . . .	142
7.6.2	Monte Carlo Simulation . . . . .	147
7.7	Conclusions . . . . .	148
<b>8</b>	<b>Conclusions and future work</b>	<b>149</b>
8.1	Overview and contributions of this work . . . . .	149
8.2	Directions for future work . . . . .	150
	<b>Bibliography</b>	<b>152</b>
	<b>Appendix</b>	
<b>A</b>	<b>Multi-Sphere Model Geometries</b>	<b>165</b>
A.1	Servicer MSM Model . . . . .	165
A.2	Target MSM Model . . . . .	169

## Tables

### Table

2.1	Key scenarios that drive requirements for sensing accuracy, update rate and range.	20
3.1	Elemental sources of the dominant peaks in the spectrum shown in Figure 3.15, along with the relative abundance by mass of each element in the Inconel 625 sample per manufacturer's test report. The remaining 4% composition consists of trace elements without distinct peaks in this energy range and rounding in abundances. . . . .	55

## Figures

### Figure

1.1	Intelsat-901 as seen from MEV-1 during approach in first GEO servicing mission. Image credit: Northrop Grumman . . . . .	2
1.2	A spacecraft interacts with a range of environmental currents on orbit [14]. . . . .	4
1.3	Distribution of Kp index values over the last 4 solar cycles (October 1964-December 2019). . . . .	6
1.4	Selected interactions between incident electrons and atoms: backscatter (A), electron emission and inner shell vacancy formation (B), characteristic x-ray emission (C), and bremsstrahlung x-ray emission (D). . . . .	9
1.5	ECLIPS space environments test facility at the AVS Lab. . . . .	10
1.6	Concept of the operating electrostatic tractor, utilizing an electron beam to control the charge on a debris body. . . . .	13
1.7	Illustration of electrostatic interactions between a servicer and a client spacecraft. . .	15
1.8	A traditional finite element model of a spacecraft (top) and an equivalent MSM version (bottom). . . . .	16
2.1	The fundamental remote potential sensing method. If the energy of electrons emitted by the servicer is known, and the landing energy of those electrons on the target estimated from the resultant x-ray spectrum, then the potential difference between servicer and target is determined. . . . .	19

2.2	Selected interactions between incident electrons and atoms: incident electron is backscattered (A), electron emission and inner shell vacancy formation (B), characteristic x-ray emission (C), and bremsstrahlung x-ray emission (D). . . . .	21
2.3	X-ray spectrum resulting from aluminum irradiation with 5.5 keV electrons. . . . .	22
2.4	Example of curve fitting process for landing energy estimation. Line is fit to points in magenta, then extrapolated to the energy intercept. . . . .	23
2.5	Comparison of theoretical spectrum from Equation 2.3 and experimental results. Beam parameters: 10 $\mu$ A, 5.5 keV. . . . .	24
2.6	Ratio of characteristic flux to total radiation yield for aluminum. . . . .	25
2.7	Angular distribution for bremsstrahlung radiation of different energies ( $k/E_o$ ) as a function of incident electron energy. Electron is incident from left to right, interacting with particle at the origin. . . . .	26
2.8	Basic case of two conducting spheres. . . . .	27
2.9	The GOES-R spacecraft approximated as an 80-element MoM finite element model (left) and an 80-sphere MSM model (right). Spheres are colored according to surface charge density. . . . .	31
2.10	The two-panel spacecraft configuration as a MOM and MSM model, both with 92 elements. . . . .	32
3.1	The ECLIPS experimental test facility . . . . .	35
3.2	Electron beam characteristics . . . . .	37
3.3	Output spectra for broad-spectrum electron gun set to different energies. . . . .	38
3.4	Schematic of the broad-spectrum electron gun design and operation. The side view shows how the voltage gradient is applied to the stages and how the UV light is used to stimulate photoelectron emission from each stage. The rear view shows the shape of each stage with a grid to contain the electric fields on the rearmost stage only. . .	39

3.5	Electric field streamlines (blue) and electric field (orange arrows) imposed on the electron gun CAD model with 54 discrete stages. . . . .	39
3.6	Prototype of the broad-spectrum electron gun with 54 discrete stages. . . . .	41
3.7	Front view of the broad-spectrum electron gun. . . . .	41
3.8	RGA spectrum from 0-80 amu. . . . .	43
3.9	Example experimental setup in chamber. RPA and x-ray detector seen on the left, VUV light in center, and target Inconel plate connected to a HVPS on right. . . . .	45
3.10	Amptek X123 detector. . . . .	46
3.11	Rotational stage (center) with translational stage mounted atop it. . . . .	48
3.12	Power supplies and control infrastructure for the chamber. The server rack at top right contains HVPS, and controllers for the electron and ion guns. . . . .	49
3.13	Electron beam focused and aligned to center of Ti target plate. . . . .	50
3.14	Top-down view of the experimental setup with a rotating target plate. The electron gun is mounted to the top left port, just above the x-ray detector. . . . .	52
3.15	X-ray spectrum from 10 keV beam on an Inconel target, as received and after lowpass filtering. . . . .	53
3.16	Power spectrum plot for spectrum from 10 keV electrons on Inconel. Filter bandwidth was set to 0.144 to preserve the 99% occupied bandwidth, shown in blue highlight. . . . .	54
3.17	Determination of landing energy from x-ray spectrum, with characteristic peaks identified by element. . . . .	55
3.18	Experimental setup for fixed plate, rotating sensor tests. . . . .	56
3.19	X-ray spectra observed for an Inconel plate at different angles relative to the incident 10 keV beam. . . . .	57
3.20	The full set of unprocessed x-ray spectra from Inconel. Note that although the landing energy changes the curve of each spectrum, the characteristic peak positions are fixed. Electron landing energies varied from 2.5-20 keV. . . . .	57

3.21	Landing energy errors vs detector-beam separation angle. Filled circles represent mean for each angle, error bars indicate $1\sigma$ spread. . . . .	58
3.22	Efficiency of X-123 x-ray detector as a function of incident photon energy [3]. . . . .	59
3.23	Error in landing energy for unprocessed spectra (left) and spectra where flux has been scaled according to detector efficiency (right). All runs had $\leq 7\text{keV}$ beam energy, plate potentials 100-2000V. Both histograms have a 30V bin width. . . . .	60
3.24	Relation between true landing energy and normalized error in the landing energy estimate. The slope of a linear regression to the data is 0.35 percent per keV. . . . .	60
3.25	Spectra resulting from rotating target plate, fixed detector position for 5 keV beam on Ti target. . . . .	62
3.26	Errors in landing energy estimation for rotating titanium target plate. The $0^\circ$ reference is perpendicular to the incident beam; interference with the chamber wall occurs at $> 40^\circ$ . . . . .	62
4.1	The electron flux at GEO for IGE-2006 model lower, mean and upper fluxes. Points from the model are illustrated by the markers, the lines are for illustrative purposes only. . . . .	67
4.2	X-ray spectrum due to mean electron flux conditions at GEO. . . . .	67
4.3	Electron flux from the IGE-2006 mean flux and that observed by a spacecraft charged to -10 kV. . . . .	68
4.4	Change in total x-ray photon emission due to plasma electron bremsstrahlung as a function of spacecraft potential. . . . .	70
4.5	Experimental setup in chamber . . . . .	71
4.6	Integral electron flux of the broad-spectrum electron gun up to 3.3 keV, measured by the retarding potential analyzer. . . . .	72
4.7	Change in total x-ray photon emission due to ambient plasma as a function of plate potential. . . . .	74

4.8	Error of the estimated plate potential for the set of points shown in the left plot. . .	74
4.9	Change in characteristic x-ray photon emission due to ambient plasma as a function of plate potential. . . . .	75
4.10	Error of the estimated plate potential for the set of points shown in the left plot. . .	75
4.11	The solar x-ray spectrum observed by MinXSS-1. July 23 was the date of 2016's most significant flare event, an M7.6, and illustrates enhanced x-ray flux relative to the quiet August 20th spectrum [2]. . . . .	76
4.12	Simulation of sensed x-ray spectrum for a 10 $\mu$ A electron beam and ambient plasma electron fluxes, using the IGE-2006 mean flux. The target is assumed to be an isotropically emitting point source equivalent to a 5 m <sup>2</sup> aluminum spacecraft. . . .	78
4.13	Twenty electrons (250 keV initial energy) incident on a simulated detector structure. The top two layers represent the top and bottom faces of the 25 $\mu$ m beryllium window, while the bottom layer represents the top face of the silicon diode. 100 $\mu$ m of vacuum separate the materials. . . . .	80
4.14	Electron, proton and GCR spectra and the relative energies required to penetrate the beryllium detector window. . . . .	81
5.1	Example electron spectrum generated by a 10 keV, 10 $\mu$ A electron beam incident on an aluminum plate. The top panel shows the collected current as a function of discriminating grid voltage. The lower panel shows the electron distribution, Gaussian fit, and estimated voltage (dotted vertical line). The dashed vertical line gives the actual plate voltage. . . . .	88
5.2	Experiment to collect electron and x-ray spectra simultaneously. The x-ray detector is mounted atop the RPA (left), just under the electron gun feedthru (top left). The target plate (right) is mounted to a rotary stage (bottom right) to control its angle.	90
5.3	Uncertainty in plate potential determination as a function of target plate angle. . . .	91

5.4	Mean SEE signal as a function of angle between the plate normal and the instrument location for various voltages. . . . .	92
5.5	Application of adaptive filter to simulated data with eclipse-like transients. . . . .	95
5.6	Target spacecraft body. . . . .	96
5.7	Close-up view of electrons emitted from target surface. The solar panel is located to the right of box. . . . .	98
5.8	Views of electrons (black lines) emitted from target surface and servicer craft measurement points (red dots) in the target body frame. . . . .	99
5.9	Sensed secondary electron yield from target, assuming 1 $\mu$ A beam at 20 keV. . . . .	101
5.10	Photons observed by servicer, with 1 $\mu$ A, 30kV electron beam impacting target. . . . .	102
5.11	Photon flux sensed at servicer as a result of target-plasma interactions. . . . .	103
6.1	Electrostatic force and torque interactions between spacecraft in close proximity. . . . .	106
6.2	Initial position of the servicer (right) and uncooperative target (left). Red dots indicate hold points along a nominal rendezvous trajectory. . . . .	108
6.3	Sample points of constant distance (10 meters) to the spacecraft used to evaluate electrostatic torque on a target as a function of azimuth and elevation. . . . .	109
6.4	Force and torque for different servicer locations, with the servicer at 10 meters from the target. All evaluated at 10 kV, with a servicer based on the symmetric two-panel MSM model, and a target based on the GOES-R model. . . . .	110
6.5	Torque magnitude acting on target as a function of servicer azimuth and elevation, with all positions located 10 meters from the target. All points evaluated at 10 kV. . . . .	110
6.6	Maximum electrostatic torque between servicer and target as a function of distance. . . . .	111
6.7	Results of servicer holding a fixed position relative to a target for a 5 hour hold, shown in the Hill frame. Electrostatic torques result in a significant tumble being imparted to the target, despite it having no initial rotation. . . . .	115
6.8	Variation in target parameters with changing servicer position. . . . .	116

6.9	Increase in control effort (as a multiple of the $\Delta V$ for the 0V, SRP-only case) required to hold a fixed 10 meter offset from the target for different servicer $\hat{z}$ positions. . . . .	117
6.10	Torque required by servicer to maintain a relative orientation to the GOES-R target while holding a 10 meter offset position and 10 kV on each spacecraft. . . . .	118
6.11	Perturbed rendezvous trajectory with -10 kV potential on each spacecraft. . . . .	119
7.1	Reference frames for the proximity operations scenario. $\mathcal{H}$ is the Hill frame, taken to be inertial for this scenario, $\mathcal{S}$ is a frame fixed to the servicer and $\mathcal{T}$ is fixed to the target's docking port. . . . .	123
7.2	Illustration of two-sphere system evaluated. . . . .	125
7.3	Sensitivity of electrostatic force to errors in $\Delta V_{T,s}$ and $V_S$ . . . . .	128
7.4	Servicer attitude error during a 180° slew maneuver. . . . .	130
7.5	Constraint cone fixed to target docking port, and selected test positions at a fixed distance to the target port. . . . .	133
7.6	Conceptual illustration of four updates of iterative guidance strategy. Best solution at each time step shown in red, black line represents the servicer trajectory between each pair of points. . . . .	133
7.7	The nominal approach trajectory from the two-panel servicer to the one panel target at the origin. Hold points are shown in red. . . . .	134
7.8	Position and velocity of the target-frame desired rendezvous trajectory. . . . .	134
7.9	Torque acting on a GOES-R target due to electrostatic interactions at a 10 meter distance as a function of azimuth and elevation. Circled region corresponds to a 25° approach cone. . . . .	137
7.10	Electrostatic torque imparted to the target as a function of servicer attitude, where the servicer is only rotated about the line of sight (LOS) vector. . . . .	138
7.11	Rendezvous trajectory perturbed by 10 kV electrostatic potential on each spacecraft, with no guidance accounting for electrostatic interactions. . . . .	140

7.12 Rendezvous trajectory perturbed by 10kV electrostatic potential on each spacecraft, with guidance accounting for electrostatic interactions. . . . .	140
7.13 Sensitivity of $L_{T,\text{electro}}$ to target attitude estimation errors . . . . .	141
7.14 Pre-computed optimal trajectory, initial states. . . . .	146
7.15 Pre-computed optimal trajectory, final result. . . . .	146
7.16 Target final rotational rate through 500 runs of a monte carlo simulation. . . . .	147

# Chapter 1

## Introduction

### 1.1 Motivation

After decades of research, robotic orbital servicing is finally moving from a promising, albeit futuristic, concept to reality. The Mission Extension Vehicle (MEV-1) from Northrop Grumman's SpaceLogistics subsidiary launched as the first commercial satellite servicing mission in 2019. MEV-1 successfully rendezvoused with Intelsat 901 in the geostationary orbit (GEO) graveyard as seen in Figure 1.1, physically latching onto Intelsat 901 and assuming station keeping and attitude control responsibilities for the fuel-depleted communications satellite. This adds years of useful life to the otherwise functional communications satellite, and introduces the era of commercial orbital servicing [38]. Similarly, NASA is planning a robotic refueling demonstration of the Landsat 7 spacecraft, a vehicle which was never designed for servicing, within 3 years [128]. These missions, as well as a range of related concepts from servicers to space tugs, illustrate a rapid maturation of robotic servicing technologies dependent on automated rendezvous operations.

In a field related to orbital servicing, the need for active debris removal (ADR) in all orbital regimes is becoming more pressing with every collision and near miss. The addition of tens of thousands of spacecraft in mega-constellations will only further heighten the need to remove potentially hazardous debris objects [80]. Such operations, whether for servicing or debris mitigation, will inevitably require automated rendezvous. However, few servicing operations have ever been conducted on orbit, though space stations such as the ISS and Mir, as well as crewed servicing missions for spacecraft like the Hubble Space Telescope are notable exceptions. Even fewer missions have

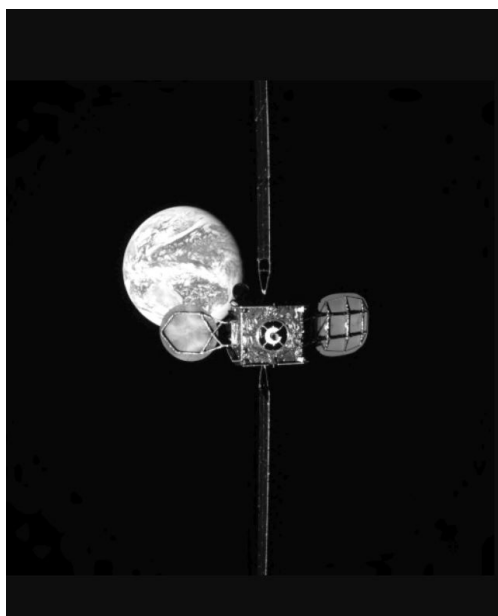


Figure 1.1: Intelsat-901 as seen from MEV-1 during approach in first GEO servicing mission. Image credit: Northrop Grumman

utilized robotic servicing, and none other than MEV-1 have occurred in GEO. Additionally, all of these rendezvous maneuvers occurred with well characterized, cooperative targets, which cannot be assumed for a debris remediation or repair mission.

The GEO regime is particularly valuable, with limited orbital slots available providing the backbone of many earth observing and telecommunications networks. Spacecraft in GEO tend to be larger and more valuable than their LEO counterparts, and therefore particularly attractive from a servicing perspective. These range from multi-billion dollar satellites NOAA uses to improve weather forecasts to telecommunications satellites with construction costs in the hundreds of millions of dollars [4, 94]. In-orbit services are expected to become a multi-billion dollar market in the coming decade, driven in large part by missions requiring rendezvous and proximity operations in high earth orbits.<sup>1</sup>

Critical phases of these servicing/ADR missions in high earth orbits face challenges from electrostatic charging. Contact between differentially charged spacecraft results in arcing that can

---

<sup>1</sup> <https://spacenews.com/in-orbit-services-poised-to-become-big-business/>, accessed March 3, 2021.

damage electronics, and even spacecraft at equal potentials will be subject to perturbing forces and torques during proximity operations. Rather than always acting as an obstacle, a range of missions propose to leverage electrostatic charging in high earth orbits to impart forces and torques, allowing remote control over the attitude and orbit of debris objects. However, these missions require the ability to measure electrostatic potentials remotely for effective charge hazard mitigation or feedback control of forces and torques.

## 1.2 Spacecraft charging and potential sensing

Objects in space charge through interactions with a variety of currents throughout their orbits, as illustrated in Figure 1.2. Solar hard-UV light (also known as Vacuum Ultra Violet, or VUV) drives photoelectron emission, and is typically the dominant current in sparse plasma environments [91]. Additional plasma interactions can drive either positive or negative currents depending on the plasma properties. Each current is a function of spacecraft potential, which floats until the currents are in equilibrium. This equilibrium potential varies depending on the ambient space environment, and spacecraft material properties. Spacecraft typically reach an equilibrium potential within seconds, as the environmental currents are large relative to the spacecraft self-capacitances, leading to short charging time constants [102, 117].

### 1.2.1 Space environment and spacecraft charging

For spacecraft operating in the relatively cold, dense plasma present in Low Earth Orbit (LEO), potentials are typically a few volts positive in sunlight due to the photoelectric currents, and a few tens of volts negative in eclipse [91]. While these mild potential levels are typically seen in LEO, some orbits passing through auroral zones can briefly experience potentials greater than -2 kV [9, 31]. The dense low-energy plasma present in low earth orbits leads to a small Debye length, which is a measure of screening of electrostatic charges in a plasma. A short Debye length corresponds to a high shielding effect, limiting the range over which electrostatic charges can interact; for LEO, this value is generally on the order of centimeters [144].

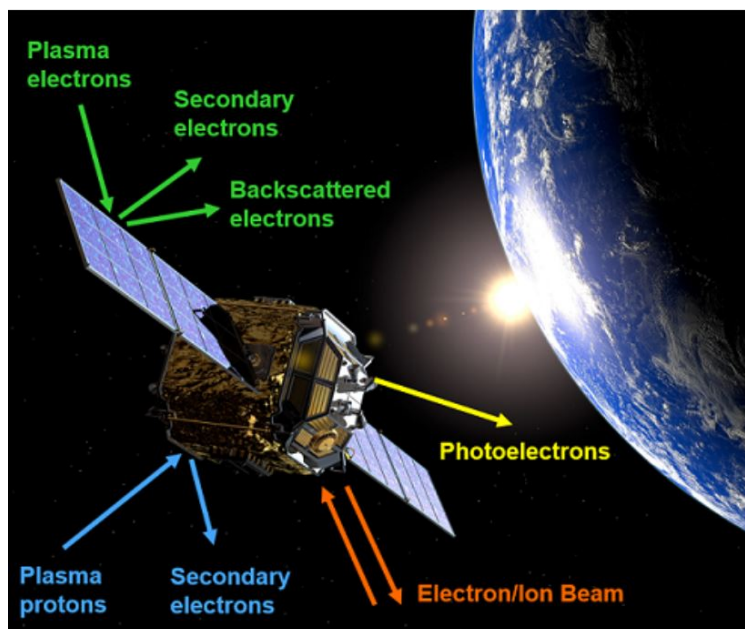


Figure 1.2: A spacecraft interacts with a range of environmental currents on orbit [14].

In the sparser, hotter plasma environment found at geostationary orbit (GEO), objects still generally charge only a few volts positive in daylight. However, large potentials are common in eclipse, and spacecraft can naturally charge to magnitudes of up to -20 kV during significant geomagnetic events [116]. This charging can cause significant problems relating to electrostatic discharges, including damaged solar arrays and potential loss of spacecraft [49, 82, 91]. Furthermore, while guidelines for spacecraft design recommend that all components be grounded to the frame, this may not always apply. Some spacecraft may have been launched without such continuity, while others may have had components degrade in the space environment to no longer be conducting. References [125, 118] find that periods of low charging with  $< |20|V$  frame potentials could still result in ungrounded components, such as pieces of Kapton or Mylar, experiencing several kV-level potentials. The presence of dielectrics can also lead to spacecraft charging to kV-level negative potentials even in sunlight, due to potential barrier effects that develop on the spacecraft [90, 107, 160]. Therefore, some spacecraft components can charge to significant levels even when the spacecraft frame potential is negligible.

The low plasma density and higher plasma temperatures of the GEO environment lead to

large Debye lengths on the order of 100m for common space weather conditions [144]. This enables electrostatic charges on objects to interact over ranges of tens of meters in GEO, which enables a range of electrostatically-actuated mission designs.

For this work, continuously conducting spacecraft are assumed, so all surfaces hold an equal potential. This is a suitable assumption for high Earth orbit or geosynchronous spacecraft as their construction guidelines require a continuously conducting outer surface to avoid differential charging among components [52, 126].

Regardless of orbit, spacecraft charging can create dangerous situations as differential charging can result in arcing and potential electronics damage. Differentially charged spacecraft components lead to arcing hazards that damage spacecraft electrical systems and frequently damage solar panels [51, 49, 81]. Reference [29] found half of satellite insurance claims to be the result of solar panel anomalies, motivating a need to better understand charge distributions on spacecraft to mitigate such issues. Internal dielectric charging on board spacecraft at GEO has been linked to reaction wheel failures and mission loss [168].

Potential threats also exist for rendezvous and servicing missions, as bodies charged to different potentials may experience damaging arcing as they contact [91]. Spacecraft during rendezvous are likely to carry different potentials due to differences in material properties, leading to the risk of arcing during contact which can damage electronics and other systems [56]. While many operational concepts include plasma contactors and other mechanisms to equilibrate two spacecraft to the same potential prior to docking to minimize arcing risk [31, 56], there can still be significant  $> 10$  mN forces acting between the spacecraft due to electrostatic interactions. These forces can be significant perturbations during rendezvous, and may need to be taken into account by the GNC system.

### 1.2.2 Frequency of severe charging

Spacecraft charging in the GEO region is known to occur more frequently during enhanced electron fluxes associated with geomagnetic storm time conditions [120]. The global  $K_p$  index is

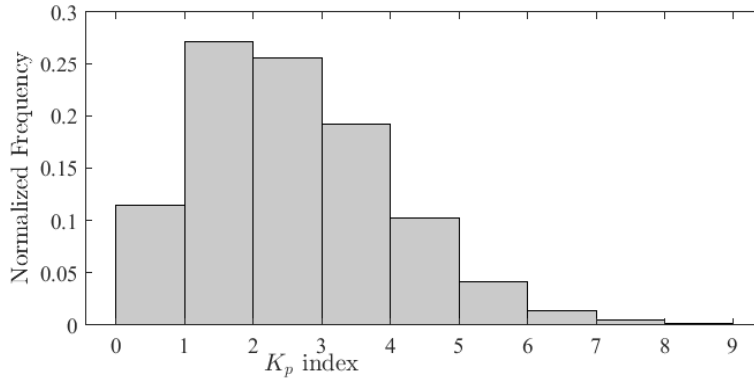


Figure 1.3: Distribution of  $K_p$  index values over the last 4 solar cycles (October 1964-December 2019).

a widely used measure of geomagnetic disturbance. It is evaluated based on terrestrial magnetic field measurements every 3 hours on a 0-9 scale, with higher values indicating a more disturbed magnetic field. Data for the  $K_p$  index every 3 hours for the last 4 solar cycles, spanning October 1964 to December 2019, was obtained from Reference [113].

For the majority of measurements over the last 4 solar cycles, the  $K_p$  index was  $K_p < 3$  as seen in Figure 1.3, indicating relatively quiet geomagnetic conditions. However, 36% of measurements recorded  $K_p = 3$  or higher, indicating a somewhat disturbed geomagnetic environment, with approximately 6% of measurements exceeding  $K_p = 5$ , indicating a storm condition. These events are concentrated around periods of solar maximum, and a 30-day sliding window applied to the data reveals 30 day periods with over 15% of measurements at  $K_p = 5$  or higher. Charging events can still occur during periods of quiet ( $K_p < 3$ ), but tend to be less likely, less intense and less prolonged [120].

Reference [120] finds that times of elevated  $K_p$  are associated with a 30% chance of experiencing charging events, compared with low single-digit probabilities during low  $K_p$  periods. Ultimately, this suggests that, while severe electrostatic charging that could result in significant perturbations during proximity operations are rare, periods with frequent charging events can occur, warranting further consideration of the impacts of electrostatic charging on proximity operations.

### 1.2.3 Spacecraft potential sensing

The spacecraft potential sensing problem can be viewed as two parts. One, a spacecraft must be able to measure its own potential relative to the surrounding plasma environment. Two, there is an additional need to remotely characterize the potential on an uninstrumented spacecraft or object remotely during proximity operations.

#### 1.2.3.1 Spacecraft potential self-sensing

Several methods have been developed to enable a spacecraft to sense its own potential relative to its surrounding plasma environment. The potential of a spacecraft relative to the ambient plasma environment can be sensed through the use of a range of instruments, including compact plasma instruments or deployable booms with electric field and wave instruments [105]. Boom-based instruments for potential monitoring in high earth orbits are often tens of meters long, seeking to reach beyond the spacecraft's Debye sheath and into the surrounding ambient plasma. A conducting probe at the end of the boom can then be used to determine the relative potential of the spacecraft to the plasma [105].

Another common method for measuring the potential of a spacecraft relative to the ambient plasma is to use an ion energy spectrometer to determine the evolution of a stable reference line in the background plasma ion population. If a given proton population is known to have an energy of, for instance, 5 eV, then the observed energy of that population provides a measure of negative charging relative to the plasma. Similar methods can be used with electron populations to measure positive potentials. These methods are limited in accuracy by the energy resolution of the instrument used, but can typically resolve spacecraft potentials to within  $< 5\%$  [132].

#### 1.2.3.2 Proposals for remote potential sensing

One approach to estimating the potential on a co-orbiting spacecraft is simply to use a spacecraft charging simulation to compute the anticipated equilibrium potential as a function of the spacecraft's composition and the space environment conditions.

A range of numerical models and programs exist for modeling the charge on a spacecraft as a function of its material composition and space environment conditions, including NASCAP, MSUCAT, SPARCS and SPIS [40, 108, 114]. However, these methods are highly sensitive to spacecraft material properties and even temperatures, particularly the secondary and backscatter electron yields. Unfortunately, these properties are highly sensitive to material condition, surface finish, the presence of contaminants or oxidation layers and even weathering effects in space, leading to variation of up to a factor of 5 between measurements of yield coefficients for aluminum [95]. These mismatches in material properties can lead to significant multi-kV differences in modeled potentials when compared to flight datasets [36].

Beyond uncertainty in material properties for a target spacecraft, additional complications are introduced in the ambient plasma environment by the presence of multiple highly charged bodies in close proximity [109, 144].

The combination of these uncertainties results in a scenario which is highly challenging to model with any degree of confidence, which limits the utility of these methods for estimating the potential on a nearby object in a proximity operations scenario. Therefore, a method for directly measuring the potential on nearby objects during proximity operations is required.

A few prior proposals exist for determining the charge on an object remotely. Reference [21] suggests determining the relative charge on a space object by comparing its orbital motion to that of a nearby object of known charge; by examining how the object's motion is perturbed over a period of minutes or hours, it is possible to determine a single point estimate of the relative potential on the unknown body. This method is limited in temporal resolution to updates on the order of hours, limiting its utility in a proximity operations scenario and is highly sensitive to modeling of other potential perturbation sources like SRP.

Reference [46] proposes measuring electric fields in the vicinity of a space craft to determine the electrostatic potential and charge distribution on a nearby object. This work focuses on generating a multisphere representation of the charge on the target object from sensed electric fields, however, it neglects the challenges of electric field sensing in a sparse plasma environment.

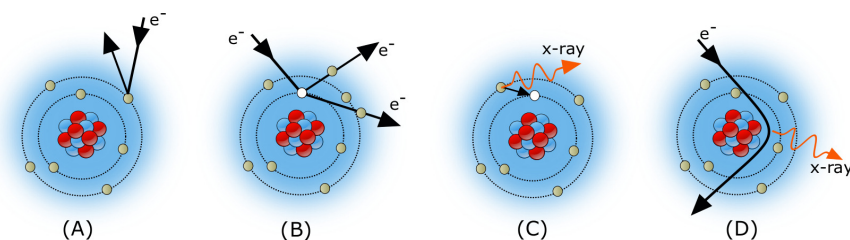


Figure 1.4: Selected interactions between incident electrons and atoms: backscatter (A), electron emission and inner shell vacancy formation (B), characteristic x-ray emission (C), and bremsstrahlung x-ray emission (D).

Reference [53] offers a series of methods to remotely detect signatures of charging events. Among these methods, the authors suggest that it may be possible to detect periods of high energy electron fluxes by looking for bremsstrahlung x-rays from a co-orbiting observatory, which would provide an indication of a charging event remotely. However, this method would not provide any information on the magnitude of charging, and could at best be a proxy indicator for local space weather at a satellite.

The electron microscopy field has long had challenges associated with surface charge buildup as a result of electron bombardment, and have consequently developed a range of methods to determine the surface potential of a sample without physically contacting it [11, 64, 34]. One method is that of examining the electron energy spectra to find a peak generated by secondary electrons, which are born on the target surface with near zero energy. Therefore, the energy the electrons acquire prior to capture is equivalent to the potential difference between the surface and the detector. This method is applied to sense lunar surface charging by [58], and is examined in spacecraft scenarios by [15] and experimentally by [17, 14].

Another approach outlined for microscopy applications by [11] leverages the x-ray spectra generated by bremsstrahlung radiation as seen in Figure 1.4 D. As electrons interact with atoms, the energy lost in each interaction is emitted as an x-ray photon through bremsstrahlung radiation. These x-rays form a continuum in energy with an upper limit as the landing energy of the incident electrons. Therefore, this spectrum can be used to establish the landing energy of the electrons. If the initial energy of the electrons leaving the gun are known, then the change in energy to

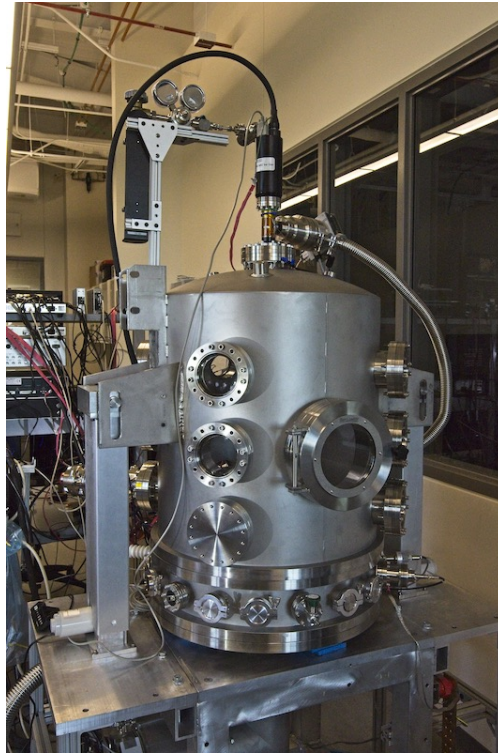


Figure 1.5: ECLIPS space environments test facility at the AVS Lab.

landing can be used to determine the potential difference between the source and the target. The application of this method to spaceflight scenarios is the focus of this work.

Additionally, characteristic x-rays shown in Figure 1.4 C have unique energies that can be used to identify the specific element they come from, which enables material identification as well as surface potential determination.

#### 1.2.4 Chamber overview

The complexities of the space environment and enormous cost and difficulty involved in in-situ experimentation necessitate the development of terrestrial facilities to explore interactions of interest to spacecraft charging and potential sensing. To this end, the Autonomous Vehicle Systems (AVS) Laboratory at the University of Colorado Boulder has developed the Electrostatic Charging Laboratory for Interactions between Plasma and Spacecraft (ECLIPS), a vacuum chamber facility seen in Figure 1.5 and designed for conducting spacecraft charging experiments.

While facilities designed to simulate thermal and vacuum (TVAC) environments in space have become commonplace as a pre-flight requirement for any spaceflight mission, experimental facilities intended to study spacecraft charging are fairly rare. A notable example is the JUMBO chamber at the Air Force Research Laboratory (AFRL) in Albuquerque, New Mexico. Chambers such as this one, and similar facilities at Aerospace Corporation, are primarily used to evaluate the impact of the space environment on materials, electronics and other components intended for orbital use [1]. The Sirene facility at ONERA in France likewise provides a sophisticated testbed for characterizing material properties under space environment exposure [122]. Another facility at Utah State University is also focused on spacecraft charging impacts, and uses a variety of photon, electron and ion sources to evaluate the electronic properties of materials [42].

Rather than focusing on fundamental material science or flight qualification questions as many other facilities do, the ECLIPS chamber aims to focus on charged astrodynamics phenomena such as remote sensing of electrostatic potential or plasma wake dynamics. Charged astrodynamics has been studied for over 20 years to explore how touchless actuation enables novel methods of close proximity control of space objects [39, 84]. The chamber's unique capabilities have many uses beyond charged astrodynamics, including applications to plasma wakes, environment simulation and rendezvous and proximity operations. However, no current vacuum chamber research facility specializes in the study of electrostatic actuation and touchless sensing of electrostatics in a space environment. Thus the idea of the ECLIPS chamber was formed to explore these exciting research directions with experimental support.

## **1.3 Spacecraft proximity operations**

### **1.3.1 Servicing overview**

Operational servicers, like the Northrop Grumman Mission Extension Vehicle, are designed to operate with a well-characterized and cooperative target spacecraft. This constraint ensures that the target spacecraft will behave in a predictable manner, avoiding risky proximity operations

with a tumbling object. These missions are a key method for extending the lifetime of currently operating assets in GEO, but are not capable of addressing the need for debris remediation missions. In addition to being a highly valuable orbital regime, GEO is also becoming increasingly congested. Reference [8] evaluates the frequency of near-miss events between operating spacecraft and debris objects in the GEO region, and finds that the frequency of such events strongly motivates the need to begin active debris removal operation to preserve the future capacity and utility of the region.

A range of proposals exist for capturing debris objects, but a major complication is introduced by the high rotational rates these objects accumulate. References [80] and [22] find GEO debris objects can have rotational rates of tens of degrees per second, far in excess of the  $< 1^\circ/\text{s}$  limit of many rendezvous proposals [26, 77]. Such high rotational rates make target capture dangerous to attempt with traditional mechanical grappling approaches, which has spurred the investigation of other solutions. These solutions include harpoons [146] and nets [153], though both of these methods may result in the generation of additional space debris. Alternative methods include the touchless ion shepherd approach, which directs an ion plume towards a debris object to impart a net force or torque [86]. Inertial thrusting by the servicer could then enable the debris object to be gently pushed into a desired orbit. However, this method is highly susceptible to target attitude and accurate plume-object interaction models.

An alternative approach is to use electrostatic forces and torques for relative motion control, including detumbling and re-orbiting a debris object, which forms a core motivation for this work.

### 1.3.2 Prior charged proximity operations concepts

The original concepts of charged astrodynamics focus on formation flight [83, 84], ranging from creating charged virtual static structures [24, 133, 25, 155], rendezvous and docking strategies [112, 110, 111], to controlling spinning sets of charged spacecraft [157, 156, 67, 66].

Linear charged relative motion control is experimentally explored in the AVS Lab using an air-bearing hover track built out of non-conducting material [142, 143, 141]. To study the charged relative rotation, References [150, 149] develop a different atmospheric test bed, utilizing

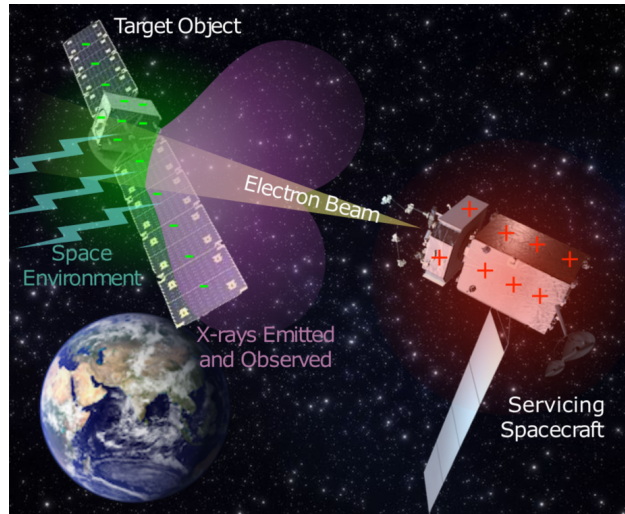


Figure 1.6: Concept of the operating electrostatic tractor, utilizing an electron beam to control the charge on a debris body.

a custom rotating bearing which could transfer a charge onto a spinning test object. However, both of these charged relative motion dynamics facilities impart a potential onto the object using an electrostatic power supply and have to contend with the ionization of the local atmosphere. To explore touchless actuation in a vacuum or space like environment a new test facility was required. Further, as identified in Reference [68], knowledge of the nominal charging both of the servicer and the second space object is critical when performing charged relative position station keeping. If the charge uncertainty is too large, then the resulting closed loop motion undergoes a bifurcation in its behavior leading to a collision. This requirement motivates a need for touchless potential sensing methods.

In addition to cooperative formation control, concepts have been recently developed to harness electrostatic forces and torques between spacecraft for touchless detumbling or re-orbiting uncooperative targets.

The Electrostatic Tractor (ET) for active debris detumbling and re-orbiting in GEO uses an electron gun to charge the space tug positively and the space debris negatively, creating an attractive electrostatic force [12, 135, 136]. The ET concept in Figure 1.6 relies on a servicing spacecraft using an electron beam to control both its electrostatic charge and the charge of a debris

object 10s of meters away. By maintaining a significant potential difference in the range of  $\pm 20$  kV between the objects, forces on the order of 10 mN can be generated [137]. While small, these forces are several times larger than other dominant perturbations at GEO, enabling this method to be reliably used for control [20]. Over a period of weeks a large multi-ton debris object can be gently tugged into a graveyard orbit – all without requiring the servicer to approach within 10s of meters of a tumbling debris object [140]. Instead of creating a fixed electrostatic force between the spacecraft, References [138, 20, 18, 19] explore the use of modulated electrostatic force fields to detumble a spinning space object.

This concept requires knowledge of the target’s charge for feedback control, and the ability to measure the charge on a space object remotely would also benefit servicing or rendezvous scenarios which may otherwise risk dangerous arcing hazards. The ability to measure spacecraft potentials touchlessly could also contribute to the overall understanding of spacecraft charging through changing environments, as current methods only measure the potential on an instrumented craft itself, without determining any charging properties of an uninstrumented object.

While many of these concepts require electrostatic charge on multiple objects to be actively controlled to attain desired dynamics, a less considered complication is the effect of natural spacecraft charging on proximity operations. Spacecraft in the GEO region can charge to 10s of kilovolts depending on local space weather conditions [116]. While such charging events are relatively infrequent, proximity operations during these times are significantly perturbed by the electrostatic forces and torques acting between the spacecraft; cases with an uncontrolled target body, such as a servicing or debris remediation mission, are particularly affected. Reference [83] finds that significant torques are generated by inter-craft electrostatic forces, as a result of natural charging in a formation flying context. With the increasing popularity and necessity of proximity operations missions in high earth orbits, there is a need to consider these induced dynamical effects which can impart target tumble rates exceeding a degree per second to an uncontrolled target during rendezvous. Such rotational rates significantly complicate rendezvous, imposing high propellant usage demands on the servicer and posing a much more challenging navigation scenario than rendezvous

with a non-rotating target body.

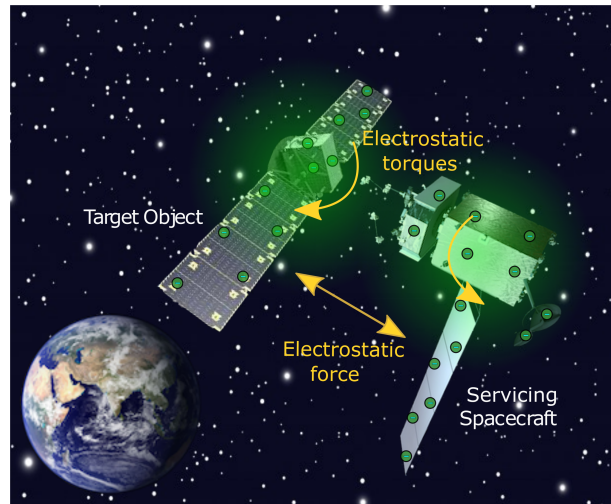


Figure 1.7: Illustration of electrostatic interactions between a servicer and a client spacecraft.

The system dynamics between two charged spacecraft are highly nonlinear, with mutual forces and torques dependent on the positions and attitudes of both spacecraft, as well as their geometries (which dictate charge distributions) and electrostatic potentials. Two innovations make rapid guidance and control in these scenarios possible: the development of methods to accurately and remotely determine the potential on a co-orbiting object, and a method for rapidly evaluating the electrostatic forces and torques between nearby bodies. The electrostatic potential sensing method is based on observations of x-ray and electron spectra excited during energetic electron bombardment of the target, either in a controlled manner using an electron gun mounted to the servicer, or by relying on hot electrons present in the ambient plasma environment [166]. Force and torque computations can then be performed using the multi-sphere method (MSM)[35], a computationally efficient means of approximating the electric fields around a body to within a few percent, given knowledge of the target’s geometry and electrostatic potential [72].

With increasing interest in rendezvous in high altitude orbits prone to charging – particularly from GEO to cislunar space – it will become necessary to assess the impact of charging on relative motion dynamics to ensure mission success during proximity operations and rendezvous.

### 1.3.3 Electrostatic force and torque modeling

Modeling of electric fields around an object is a challenging process, requiring either sophisticated, computationally demanding finite element analyses, or enormous simplifying assumptions (such as spherical geometry). Analytic expressions exist for the electric field resulting from a charged sphere, a straight wire and other prototypical shapes, but more complicated structures require finite element models and computational methods to accurately evaluate.

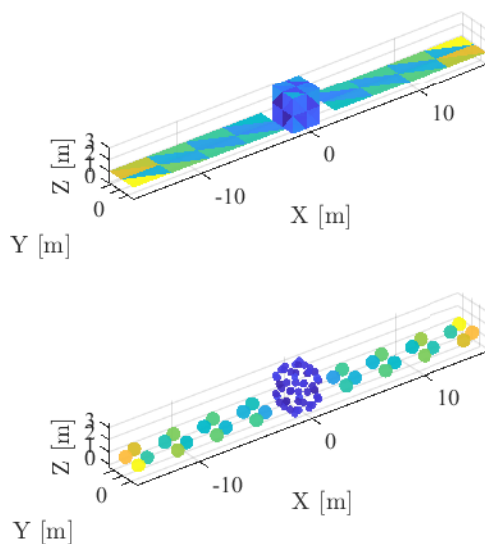


Figure 1.8: A traditional finite element model of a spacecraft (top) and an equivalent MSM version (bottom).

A recent innovation enables faster-than-realtime simulation of electrostatic interactions between bodies. The Multi-Sphere Method (MSM) discretizes a body into a series of spheres, for which the self-capacitance is a function only of the sphere radius. For multiple spheres, mutual capacitance effects are also significant, and can be found as a function of the set of sphere positions.

While computationally efficient, the MSM formulation still requires initialization using a finite element model, which provides a truth capacitance used to tune each sphere position and radius to accurately capture the charge distribution across the surface. The method of moments (MOM) is used here, as seen in Figure 1.8 and described in detail by Reference [35, 61, 72]. For comparison,

a high fidelity MoM finite element setup required approximately 1000 seconds of computation time to find the forces and torques acting between two spacecraft composed of 500 elements each. The equivalent fidelity MSM model required less than 0.2 seconds, for a  $10^4$  speed up; lower fidelity models can be evaluated much faster still with minimal loss of accuracy [72]. The finite element truth model only needs to be computed once for a structure, and the resulting multisphere model is then valid for any future case, including with flexible or time-varying structures, or multiple spacecraft operating in close proximity [101]. This makes MSM ideally suited for faster-than-realtime dynamics propagation, or real-time guidance.

Rigid bodies are assumed for the MSM structures here. However, the MSM formulation can be readily applied to time-varying geometries, such as servicer solar arrays rotating to track the sun or extending robotic arms [101]. These time-varying structures can be solved without requiring an update of the computationally-intensive finite element computation step, but can instead be updated using only the MSM formulation.

#### 1.4 Contributions of this work

The contributions of this work lie in two primary areas: developing a novel method for determining the electrostatic potential on an object in space remotely, and evaluating the dynamical impact of spacecraft charging on proximity operations.

The goal of this work is to combine these innovations in a guidance and control framework to meet proximity operation goals while minimizing the impact of electrostatic perturbations, either in positional errors, fuel consumption, or tumble rates imparted to the target. These electrostatic perturbations are unique and different compared to electromagnetic interactions which can arise in cases with alternating currents. Combining touchless potential sensing and MSM will allow for rapid evaluation of the anticipated forces and torques, suitable for implementation aboard flight hardware. This work will enable safer, more robust proximity operations during periods of heightened electrostatic charging, which in turn could enable expanded opportunities for engaging in proximity operations.

Two main areas are pursued in this work:

- (1) Measure electrostatic potentials remotely, which includes:
  - Theoretical development of sensing concept (Chapter 2)
  - Experimental validation of sensing concept to determine limitations (Chapter 3)
  - Examine impact of space environment on sensing method in space, and explore other outgrowths of this work including SSA applications and new space simulation technologies (Chapter 4)
  - Fuse complimentary potential measurements from dissimilar sensors to provide a more accurate and robust potential estimate (Chapter 5)
  
- (2) Explore the effects of electrostatic interactions on proximity operations and rendezvous, particularly in an uncooperative servicing scenario. This includes:
  - Evaluate dynamic impacts of electrostatic forces and torques on relative motion (Chapter 6)
  - Develop guidance strategies to mitigate the dynamic effects of charging during proximity operations (Chapter 7)

The development of a method for remote potential sensing represents a significant contribution to the safety of rendezvous in regions of geospace prone to high levels of charging, and is an enabling technology for the Electrostatic Tractor and other electrostatic actuation concepts. Additionally, evaluation of a previously unconsidered perturbation can provide safer, more efficient proximity operations in high earth and cislunar orbits.

## Chapter 2

### Fundamentals of Potential Sensing and Electrostatic Force Modeling

The fundamental potential sensing method developed in this work relies on observing the x-ray spectra that are emitted from a surface when energetic electrons strike it. This spectrum contains information about the landing energy of the incident electrons. If the initial energy of the electrons is known, such as those emitted by an electron beam on a servicing craft, then the change in energy of those electrons between emission and landing on the target is used to infer the relative potential difference. This is shown conceptually in Figure 2.1.

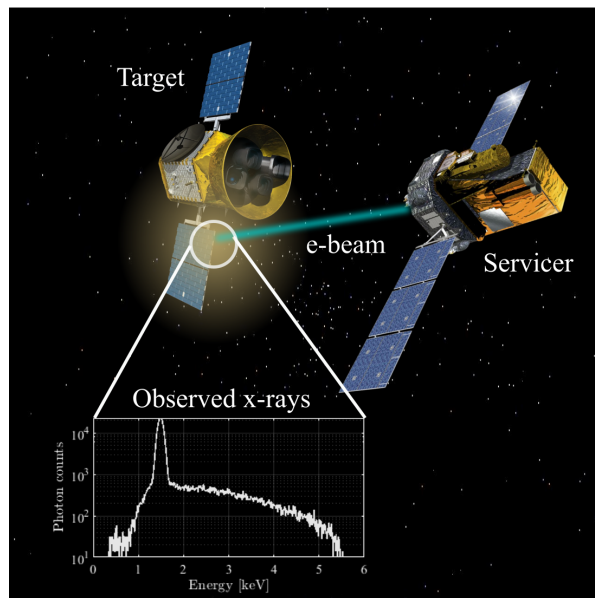


Figure 2.1: The fundamental remote potential sensing method. If the energy of electrons emitted by the servicer is known, and the landing energy of those electrons on the target is estimated from the resultant x-ray spectrum, then the potential difference between servicer and target is determined.

Scenario	Potential Resolution [V]	Update Frequency [s]	Range [m]
Determine hazardous potential differentials prior to rendezvous	1000	10	5
Evaluate force and torque perturbations (RPO or ET)	1000	100	5-50
Improve understanding of spacecraft charging	100	100	>50

Table 2.1: Key scenarios that drive requirements for sensing accuracy, update rate and range.

This chapter lays out the fundamentals of the proposed sensing method, and the techniques used to evaluate intercraft electrostatic forces and torques during proximity operations.

## 2.1 Sensing requirements

Most spacecraft built for rendezvous operations are designed with resistors or plasma contactors to provide a high resistance path for the spacecraft to equalize charge without damaging electronic components [56, 31]. However, estimating the resistance required for a first contact resistance is a challenging field, and a potential difference larger than accounted for in the design baseline is highly damaging [56]. Therefore, an estimate on the order of 1000V accuracy is sufficient for gauging discharge risk at contact, and only needs to be measured at relatively close range. Likewise, the electrostatic force and torques acting between objects are estimated to sufficient accuracy if given an estimate of 1000V or better, and these forces are significant at ranges of tens of meters [69, 165]. There is currently no method for estimating the potential of an object remotely *in situ*, but any method capable of resolving a target potential on the order of 100V would provide valuable insight into spacecraft charging dynamics and the spacecraft interaction with the surrounding environment [106, 91].

Ultimately, a sensing method that can resolve a target’s potential to within hundreds of volts at ranges of tens of meters with an update frequency of tens of seconds or better would meet the requirements for all three of these scenarios.

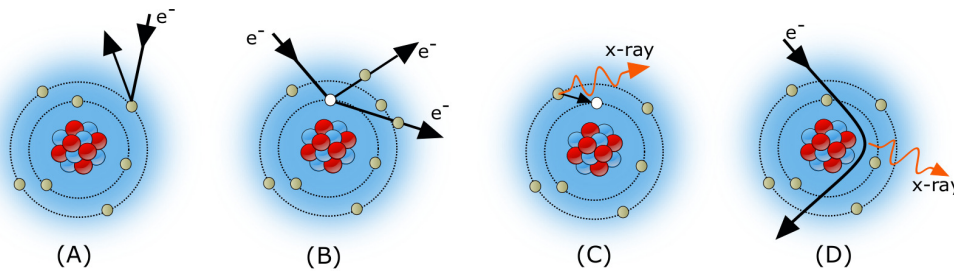


Figure 2.2: Selected interactions between incident electrons and atoms: incident electron is backscattered (A), electron emission and inner shell vacancy formation (B), characteristic x-ray emission (C), and bremsstrahlung x-ray emission (D).

## 2.2 X-ray spectroscopic potential determination fundamentals

### 2.2.1 X-ray emission from electron interactions

Energetic electrons, those with energies above a few hundred eV, can interact with atoms through a few dominant mechanisms. These electrons will undergo a series of interactions with different atoms before expending their kinetic energy. Backscatter, as seen in Figure 2.2(A), results in an incident electron preserving most of its initial kinetic energy but being deflected out of the material. When inner shell electrons are removed by interaction with an incident electron in Figure 2.2(B), the resultant electron configuration is energetically unstable. An outer shell electron then relaxes to fill the vacancy, and the energy difference between the shells is released as a characteristic x-ray specific to the element of origin, as in Figure 2.2(C). An alternative pathway results in ejection of a second electron with the characteristic energy, referred to as Auger electron emission [129].

Of particular interest to this work, bremsstrahlung radiation (Figure 2.2(D)) occurs primarily when an electron passes close to an atomic nucleus and is slowed by the interaction. The energy lost in this interaction is emitted as an x-ray. Because there are an infinite number of paths for an electron to take in the vicinity of the nucleus, the energy loss and resultant x-rays form a continuum. The upper energy limit for this spectrum is given by the Duane-Hunt law (Equation (2.1)), as the largest energy change is the case where an incident electron is fully stopped in a single interaction [45]. This limit is shown in Equation (2.1), where  $\lambda_{\min}$  represents the minimum photon wavelength

(or, equivalently, highest photon energy),  $c$  is the speed of light,  $e$  is the electron charge,  $V$  is the accelerating potential for the electron and  $h$  is Planck’s constant. Therefore, the bremsstrahlung x-ray spectrum will have no photons above the landing energy of the electrons, a property of energy conservation that is utilized to determine the electron’s landing energy.

$$\lambda_{\min} = \frac{hc}{eV} \quad (2.1)$$

If the initial energy of the electrons—either emitted from the electron gun or present in the ambient plasma—are known, then the change from initial energy to landing energy is used to establish the potential difference between the source and the target.

An example spectrum generated by a 5.5 keV, 10  $\mu$ A electron beam incident on an aluminum target plate is shown in Figure 2.3. This spectrum was collected at an angle of 45° between the incident beam and the detector, with the beam impacting the target plate perpendicularly.

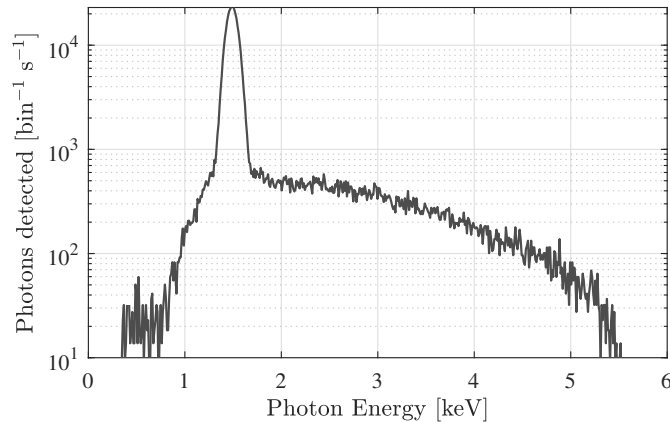


Figure 2.3: X-ray spectrum resulting from aluminum irradiation with 5.5 keV electrons.

The direct approach to determining the landing energy is to observe the highest energy photon detected, and use this as the landing energy. However, this direct method is not particularly robust, as the case where an electron is fully stopped and converts its entire landing energy to a single photon is exceedingly rare, providing few references to estimate the landing energy. A more robust method for determining the landing energy of a monoenergetic electron beam is put forward by

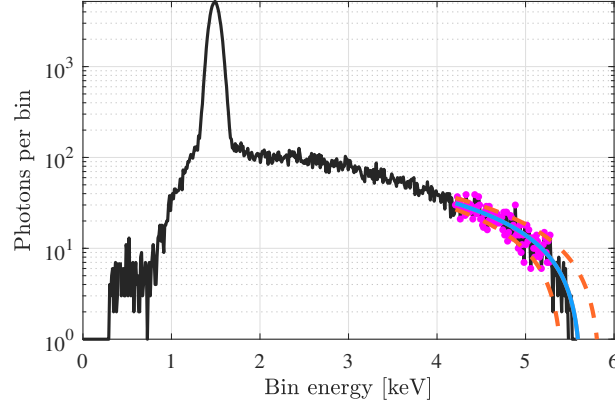


Figure 2.4: Example of curve fitting process for landing energy estimation. Line is fit to points in magenta, then extrapolated to the energy intercept.

Reference [97] in the context of high energy plasma facilities. Reference [97] propose fitting a line to the upper energy portion of the photon counts vs photon energy spectrum. The interception of this line of fit with the photon energy axis represents the landing energy.

An implementation of this method is shown in Figure 2.4, where photon counts for bins with energy  $> 0.8E_e$  are used, with  $E_e$  representing the incident electron beam energy.

### 2.2.2 Simulating x-ray spectra

Two components of the x-ray spectrum require separate calculations to simulate the complete electron-induced x-ray spectrum: the discrete energy emission of characteristic radiation, and the bremsstrahlung continuum spectrum.

Characteristic radiation occurs when an incident electron removes an inner shell electron from an atom. At this point an outer shell electron relaxes to fill the vacancy. The energy difference between the two orbitals is released as an x-ray, as in Figure 2.2 C. The binding energy of the two atomic states are unique to the element, so the energy difference between two orbitals, and therefore the energy of the emitted photon, is characteristic to a specific element and are used for elemental identification. The characteristic radiation yield, defined as the number of photons of characteristic radiation from the dominant  $K_\alpha$  transitions generated per incident electron of a

specific incident energy is estimated as

$$I_p = N \left( \frac{E_e}{E_k} - 1 \right)^\alpha \quad (2.2)$$

where, for aluminum,  $N = 1.4 \times 10^{-5}$ ,  $\alpha = 1.63$  and the energy of characteristic emission  $E_k = 1.49$ , while  $E_e$  represents the incident electron energy. Electrons with energy less than  $E_k$  are not capable of generating characteristic emission in this transition, so  $I_p$  for these cases is zero. For a given number of incident electrons  $N_e$  of a specific energy  $E_e$ , the expected number of characteristic photons is estimated [103].

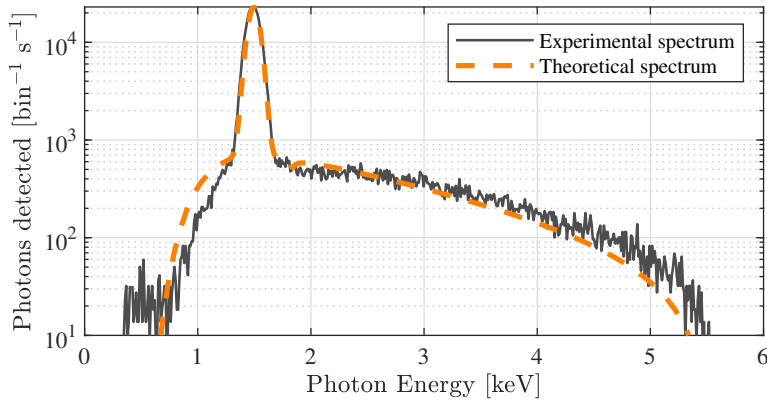


Figure 2.5: Comparison of theoretical spectrum from Equation 2.3 and experimental results. Beam parameters:  $10 \mu\text{A}$ ,  $5.5 \text{ keV}$ .

A variety of models are available to simulate the bremsstrahlung spectrum from monoenergetic electrons on thick targets, many of which are provided in review by Reference [152]. The electron is assumed to be fully stopped in the target, so a thick target model is used. These models can be divided into two main categories: analytic expressions, often empirically derived from sample data sets, and Monte Carlo-based simulations. While the Monte Carlo simulations are more accurate than the analytic expressions, they have the disadvantage of requiring significantly more computational resources; the analytic expressions are generally accurate to within 20%, which is not much worse than Monte Carlo simulations, and adequate for the analysis performed here [152]. The equation selected for use here is an empirical fit valid for photons in the 0.5-20 keV range and elements from atomic number  $Z = 4$  to  $Z = 83$ , while covering electron energies up to 38 keV.

While some electron energies considered in this work exceed this value and are subject to reduced accuracy (particularly in Chapter 4), the results are still considered sufficient for the accuracy desired here [33].

$$\Delta I = C\sqrt{Z}\frac{E_o - E}{E} \left( -73.90 - 1.2446E + 36.502 \ln Z + \frac{148.5E_o^{0.1293}}{Z} \right) \times \left[ 1 + (-0.006624 + 0.0002906E_o)\frac{Z}{E} \right] \Delta E \quad (2.3)$$

Here,  $C$  is a scaling factor that is specific to the element, while  $\Delta I$  is the change in photon emission intensity per change in energy  $\Delta E$ .

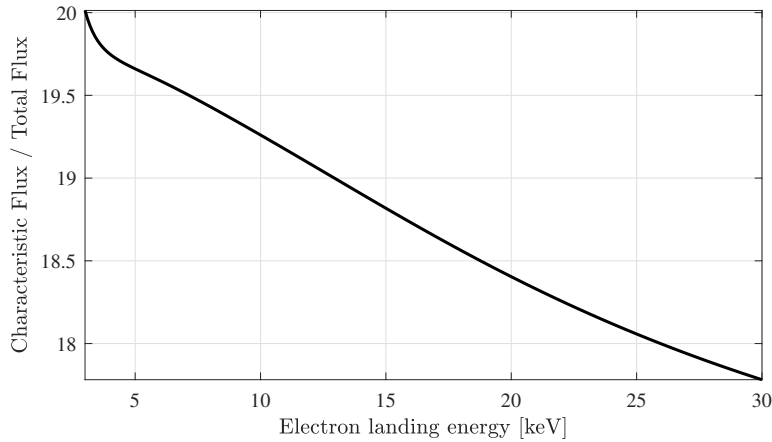


Figure 2.6: Ratio of characteristic flux to total radiation yield for aluminum.

While equation (2.3) provides a means for estimating the x-ray spectrum generated by an incident electron, it is an angle-integrated spectrum. In practice, the photon emission direction is a function of, among other things, the photon energy. Reference [85] provides shape functions for bremsstrahlung production as a function of detector angle  $\theta$ , incident electron energy  $E_0$ , and the emerging photon energy  $k$ . These shape functions are provided as a material and electron energy dependent coefficient  $A$ , and a further series of coefficients  $B_i$  which are resolved by photon energy. The  $P_i$  coefficients are used to scale Lagrange polynomials,  $P_i$ , with the coefficients for the first 6 Lagrange polynomial coefficients provided in Reference [85]. These shape functions are plotted in Figure 2.7 for an aluminum target with incident electrons of energy 5, 50 and 100 keV. The

magnitudes for each curve are normalized to allow for direct comparison of the general direction of photon emission.

$$S(E_0, k/E_0, Z, \theta) = \frac{A}{4\pi(1 - \beta_0 \cos \theta)^m} \sum_{i=0}^N B_i P_i \cos \theta \quad (2.4)$$

At low energies where relativistic effects are negligible, the predominant direction of photon emission is orthogonal to the velocity vector of the incident electron. At  $E_0 = 5$  keV, photons with energy of  $0.95E_0$  have a maximum emission at approximately  $91^\circ$ . As the incident electron energy increases the predominant direction of emission becomes more peaked in the forward direction, with a maximum at an emission angle of  $102^\circ$  for photons with energy of  $0.95E_0$  at  $E_0 = 100$  keV. There is also a significant fraction of the photon emission appearing at an angle near  $0^\circ$  for the 50 and 100 keV cases, associated with backscattered electrons. Because the emission direction is a function of incident electron energy and emitted photon energy, it is possible that a detector in a poorly chosen location may observe a spectrum that would result in a poor estimate of the electron landing energy.

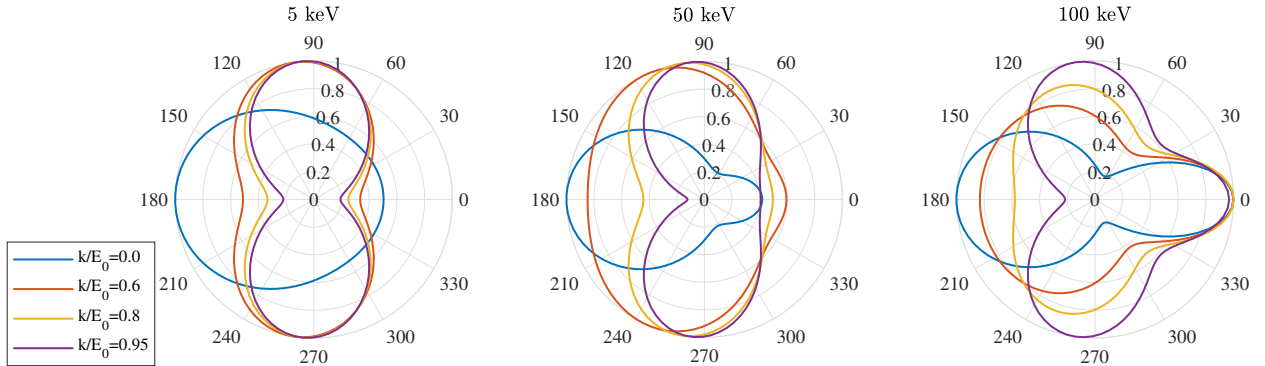


Figure 2.7: Angular distribution for bremsstrahlung radiation of different energies ( $k/E_0$ ) as a function of incident electron energy. Electron is incident from left to right, interacting with particle at the origin.

Alternative methods may be implemented to evaluate the landing energy if the upper energy portion of the spectrum is unavailable. For example, the characteristic radiation yield (Equation (2.2)) and bremsstrahlung yield (Equation (2.3)) are both dependent on elemental properties and

the incident electron energy, but follow significantly different functions. Therefore, it is feasible to use information about the ratio of characteristic flux to the total observed x-ray flux (which would include both bremsstrahlung and characteristic fluxes) to determine the landing energy of an incident electron beam, using a relation like that shown in Figure 2.6. This is particularly helpful in cases where the x-ray detector is not capable of resolving the highest energy portion of the spectrum, such as the case where a detector has a spectral range of 1-10 keV, but the incident electron beam is operating at 20 keV. However, this method requires knowledge of the material composition and requires very accurate models of bremsstrahlung and characteristic radiation yields.

### 2.3 Multi-Sphere Method For Electrostatic Force And Torque Evaluation

Charged objects operating in close proximity will exert mutual forces and torques. Evaluating the intercraft electrostatic forces and torques in a computationally efficient way is accomplished through the multi-sphere method (MSM) [35].

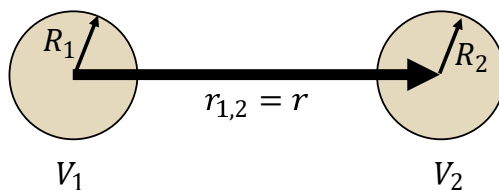


Figure 2.8: Basic case of two conducting spheres.

#### 2.3.1 Multi-Sphere Model Development

The electrostatic force for the simplest case between two point charges is provided by Coulomb's law, where forces are proportional to the product of the charge magnitudes ( $q_1$  and  $q_2$ ), and inversely proportional to the square of the distance between the charges ( $r$ ) as

$$F_c = k_c \frac{q_1 q_2}{r^2} \quad (2.5)$$

where  $k_C$  is Coulomb's constant, defined as  $k_c = 1/4\pi\epsilon_0 \approx 8.99 \times 10^9 \text{ Nm}^2/\text{C}^2$ .

The charge  $q$  of a physical object is related to the capacitance,  $C$ , by the voltage,  $V$ :

$$q = VC \quad (2.6)$$

Therefore, if the voltage of an object is known, then the capacitance is used to determine charge on the object. Electrostatic charges can then be used to determine the force acting between to bodies. However, objects in close proximity exhibit mutual capacitance effects, which must be accounted for to accurately determine the total charge on each object. For the simplest 3D case with two spheres in a pure vacuum, seen in Figure 2.8, the potentials ( $V_1$  and  $V_2$ ) are used to determine the total charge on each sphere using the relation [148]

$$\begin{bmatrix} q_1 \\ q_2 \end{bmatrix} = \underbrace{\frac{d}{k_c(d^2 - R_1R_2)}}_{C_V} \begin{bmatrix} dR_1 & -R_1R_2 \\ -R_1R_2 & dR_2 \end{bmatrix} \begin{bmatrix} V_1 \\ V_2 \end{bmatrix}. \quad (2.7)$$

where  $d$  is the distance between each sphere center, and  $R_1, R_2$  are the sphere radii.

If the capacitance of a spacecraft is known, then a spherical approximation is applied to find a radius that results in an equivalent capacitance. The self-capacitance of a sphere is given by the analytical expression:

$$C_{\text{sphere}} = 4\pi\epsilon_0 R. \quad (2.8)$$

However, two spheres only roughly approximate the electrostatic forces between two spacecraft, and fail to capture any of the torques associated with the bodies; these limitations are overcome with the use of multiple spheres. The Multi-Sphere Method (MSM) quickly and accurately approximates the distribution of electric charge on a body through the use of a series of spheres [101]. Given the potential on each sphere and its location relative to all other spheres, it is possible to analytically compute the charge on each sphere:

$$\begin{pmatrix} V_1 \\ V_2 \\ \vdots \\ V_n \end{pmatrix} = k_c \begin{bmatrix} 1/R_1 & 1/r_{1,2} & \dots & 1/r_{1,n} \\ 1/r_{2,1} & 1/R_2 & \dots & 1/r_{2,n} \\ \vdots & \vdots & \ddots & \vdots \\ 1/r_{n,1} & 1/r_{n,2} & \dots & 1/R_n \end{bmatrix} \begin{pmatrix} Q_1 \\ Q_2 \\ \vdots \\ Q_n \end{pmatrix}, \quad \mathbf{V} = [S]\mathbf{Q} \quad (2.9)$$

Here  $[S]$  denotes the elastance matrix, which is also the inverse of the capacitance matrix [72].

The total force acting on body 1, composed of charges  $q_j$ , is computed by summing the forces of each sphere in body 2 (charges  $q_i$ ) on each sphere in body 1:

$$\mathbf{F} = k_c \sum_{j=1}^{n_1} q_j \left( \sum_{i=1}^{n_2} \frac{q_i}{r_{i,j}^3} \mathbf{r}_{i,j} \right) \quad (2.10)$$

With the force between each pair of charges known, this formulation is readily extended to find the torque acting on each body:

$$\mathbf{L}_O = k_c \sum_{j=1}^{n_1} q_j \left( \sum_{i=1}^{n_2} \frac{q_i}{r_{i,j}^3} \mathbf{r}_i \times \mathbf{r}_{i,j} \right) \quad (2.11)$$

Two variations of MSM exist, one based on distributing spheres through an object's volume, and another which distributes spheres over an object's surface [148]. The surface MSM requires more spheres to achieve an equal level of electric field modeling accuracy, but does not require numerical optimization for sphere locations and radii as volume MSM does [37, 74, 72]. Surface MSM models are used in this work due to improved fitting to small surface features like booms, and a previously validated pipeline for generating MSM from finite element electrostatic models [72].

The surface MSM method requires initialization with a truth value for the object's self capacitance, which is a function of a body's geometry. Spheres are placed and their radii adjusted to match the total self capacitance of the MSM model to the truth value. Increasing the number of spheres improves the accuracy of the model, but at increased computational cost. Analytic solutions for the self capacitance of an object are available for only a select few shape primitives, such as spheres or infinite wires. Therefore, a finite element scheme is used to find the self capacitance of the spacecraft, which is then used to establish a MSM model that is fast enough for dynamic computations.

The Method of Moments (MOM) is a finite element method which is used to determine the self capacitance of an arbitrary shape. The shape is first discretized into a triangular mesh, and the capacitance of each triangular area calculated. Then, the mutual capacitance effects of all other

triangular areas in the body on the initial triangle are computed. Repeating this process for each element allows the elastance matrix for the object to be computed [72]. Spheres are then placed at the centroid of each finite element, and the radii tuned to match the total self capacitance of the object.

While the MoM simulation required on the order of 100 seconds to evaluate the spacecraft model shown in Figure 2.9, the equivalent MSM model required less than 0.01 seconds, for a  $10^4$  speed up with negligible loss of accuracy.

While a significant body of work explores variations of the multisphere method, including references [72, 37, 46, 148], this work involved the overall MSM model changing significantly with time, as the two spacecraft approached from tens of meters to tens of centimeters. The MSM formulation is validated for time-varying shapes and structures in [101]. The results of that work means that the true capacitance of each spacecraft only needs to be computed once, and the MSM model tuned from that truth capacitance is valid across a wide range of conditions.

For the case with two interacting bodies, the elastance matrix  $[S]$  is written in block form as

$$\begin{bmatrix} V_1 \\ V_2 \end{bmatrix} = \begin{bmatrix} S_1 & S_M \\ S_M^T & S_2 \end{bmatrix} \begin{bmatrix} Q_1 \\ Q_2 \end{bmatrix} \quad (2.12)$$

where the  $S_M$  terms refer to the mutual capacitances, the components which vary with the relative positions of the two bodies. Only the mutual capacitances need to be updated at each timestep as the spacecraft move relative to each other, so the MSM sphere radii and the self-capacitance matrices  $S_1$  and  $S_2$  do not need to be recomputed, which saves significant computational effort.

It is again important to note that the structures considered here are assumed to be continuously conducting, as is recommended in design guidelines for mitigating electrostatic charging. However, if the structure were not fully conducting, sections of the spacecraft could develop significantly different potentials, with differential charging resulting in several kV differences across the spacecraft [118].

### 2.3.2 Spacecraft Models

The prototypical scenario considered here involves a servicer with two solar arrays, loosely based on the Northrup Grumman MEV-1 GEO servicing vehicle, and referred to as the “two-panel model” and shown in Figure 2.10. This servicer performs proximity operations with an uncooperative target. One of NOAA’s next-generation GOES spacecraft (the GOES-R) is chosen as an example target; these craft are crucial for weather forecasting both in space and on Earth, and cost over \$2.5 billion each [4]. They also operate on traditional chemical propellants, so it is reasonable that NOAA may want to service or refuel them to extend their service lives. Significant public data is available for this spacecraft, allowing a better estimation of inertia and mass properties than is achieved for most commercial spacecraft. The two-panel model is considered as an alternative spacecraft with symmetry about the docking axis. These spacecraft shapes are chosen because they contain representative geometries that might be encountered on orbit, and they provide both a symmetric and asymmetric configuration. The latter argument about symmetry is important because the center of charge and center of mass are very different in a non-symmetric configuration, increasing the net torque acting on the body due to electrostatic interactions.

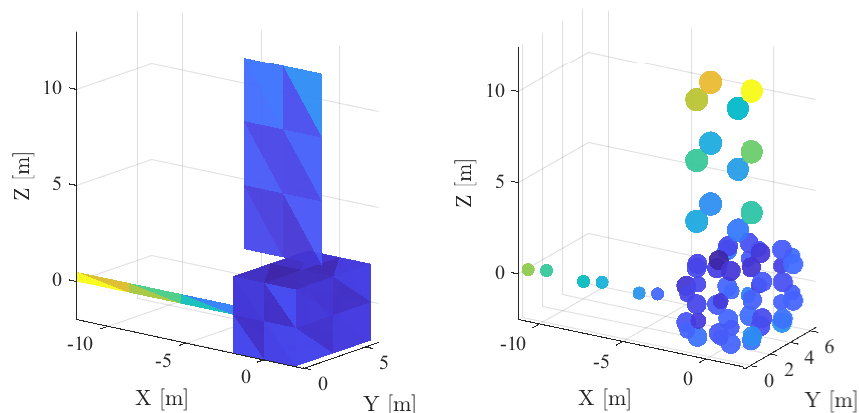


Figure 2.9: The GOES-R spacecraft approximated as an 80-element MoM finite element model (left) and an 80-sphere MSM model (right). Spheres are colored according to surface charge density.

Publicly available photographs and published dimensions of each craft are used to construct Method of Moments or MoM models [72], with an example GOES-R spacecraft model shown in

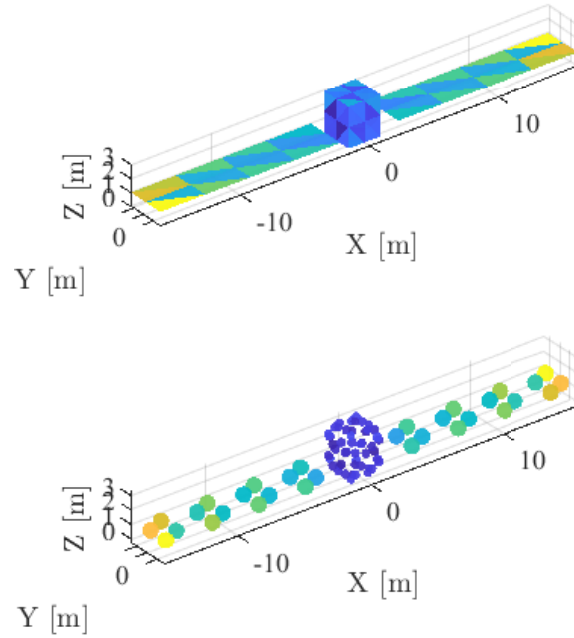


Figure 2.10: The two-panel spacecraft configuration as a MOM and MSM model, both with 92 elements.

Figure 2.9 [4]. However, inertia properties are rarely published, and knowledge of the center of mass and the inertia matrix of the uncontrolled target are necessary to accurately model the impact of electrostatic forces and torques. Therefore, these properties are estimated using the following process.

A CAD model of the GOES-R spacecraft is developed using approximate vehicle and fuel tank dimensions from Reference [4]. Published fueled and dry masses are used to determine the mass of fuel on board, which is then modeled as evenly distributed through each tank volume. The remaining dry mass is assumed to be evenly distributed through the spacecraft, excluding the tanks. This model is then used to calculate inertia properties as:

$$[I] = \begin{bmatrix} 15597 & -335.17 & 7070 \\ -335.17 & 23277 & -188.63 \\ 7070 & -188.63 & 23407 \end{bmatrix} \text{ kg-m}^2 \quad (2.13)$$

While approximate, these numbers reflect a reasonable starting point for this analysis, where

the goal is not to determine how a *specific* object will respond to electrostatic forces and torques, but instead to evaluate the *general impact* of these perturbations. For this end of life servicing mission, the fuel tanks are assumed to be depleted.

The MSM sphere locations and radii for both spacecraft models are provided in Appendix A.

## 2.4 Conclusions

The methods developed here demonstrate the physical viability of touchless potential sensing in a space environment. The analytic expressions for x-ray emission are necessarily low order approximations for the complex underlying physics, but demonstrate the soundness of the concept. The MSM models developed enable rapid and accurate modeling of intercraft forces and torques, ideally suited for simulating rendezvous and proximity operations trajectories.

## Chapter 3

### Experimental validation

While simulation and analytic spectrum modeling is an effective method for rapidly determining the basic validity of the electrostatic potential sensing concept, experimentation enables a more thorough investigation of the real-world performance of this method. Experimentation is particularly important given the large uncertainties present in simulations of bremsstrahlung spectra, and the complex physical processes underlying x-ray generation and detection.

This chapter outlines development of an experimental facility to enable testing of remote electrostatic sensing concepts. The execution and analysis of potential sensing experiments is then presented.

#### 3.1 Chamber facility development

A bell jar-style vacuum chamber, 60 cm in diameter and 1 meter in height as illustrated in Figure 3.1a, was donated to the AVS Laboratory by the Air Force Research Lab in 2016. The chamber is made of stainless steel and has an o-ring interface between the bell and the base, which has a  $1/4 - 20$  hole grid to allow mounting within the chamber. General vacuum chamber best practices are followed whenever possible, including ultrasonic cleaning of components in isopropyl alcohol prior to installation, minimization of any materials known to outgas contaminants such as many plastics, and use of vented screws in any blind holes to avoid virtual leaks.

The chamber includes a two-stage pumping system, with an Agilent IDP-15 scroll pump and an Agilent 1001 turbomolecular pump, capable of achieving pressures in the  $10^{-7}$ - $10^{-6}$  Torr range.



(a) Original chamber, as received from AFRL



(b) Current chamber configurations

Figure 3.1: The ECLIPS experimental test facility

This chamber has been significantly modified, with the addition of a range of KF and CF flanges of varying diameters, which are used to accommodate a range of view ports, sources, probes and feedthroughs. The viewports facilitate visual observations of electrostatic actuation and related processes as in Reference [101]. A current view of the ECLIPS chamber is shown in Figure 3.1b.

Sudden power failures could prove catastrophic for the turbomolecular pump, as well as electron and ion guns. To guard against this eventuality, the facility is connected to an Uninterruptible Power Supply (UPS), which provides up to 20 minutes of battery-based runtime in the event of a power failure. This is more than adequate to allow the building's backup power generators to come online and continue to provide support power to critical systems. All mechanical parts and electronic components are connected to a common ground and checked before the execution of a chamber experiment. The common ground is established by a copper grounding bar, which in turn is connected to the building ground.

The top of the bell jar is raised and lowered by two column lift mechanisms that provide

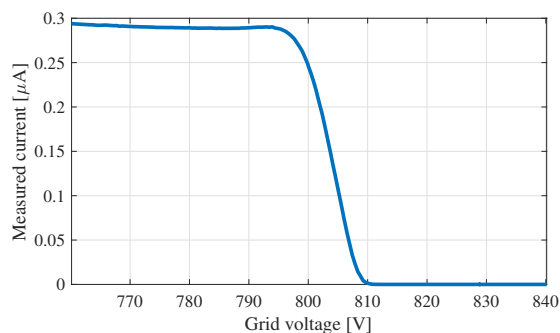
access to the chamber. These units, the FLT-12 from Progressive Automations, can provide up to 30 cm of vertical actuation with 2600 lbf (11500 N) of lifting capacity, and are controlled via wired remote programmed to specific heights. Slotted flanges welded to the exterior of the chamber enable interaction with the column lift, and also ensure that the full weight of the chamber lid rests on the o-ring interface with the base for optimal sealing. Additionally, the two lifts are electronically controlled to ensure that the chamber lid is always lifted level, and the fully-constrained nature of the system ensures that the chamber lid is repeatably positioned between runs.

### 3.1.0.1 Electron sources

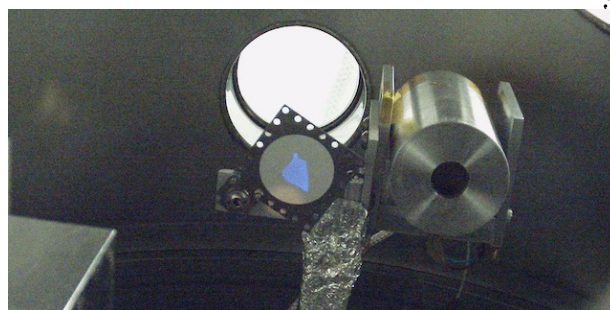
A series of sources for magnetic fields, photons, electrons and ions are integrated into the chamber, enabling various components of the space environment to be simulated. Two electron sources are particularly relevant for this work, a commercially-sourced monoenergetic electron gun and another developed through this work capable of generating broad electron energy spectra.

### 3.1.0.2 Electron gun

The primary electron gun for the facility is a Kimball Physics EMG-4212D, capable of accelerating electrons up to 30 keV. A Kimball Physics Rugged Phosphor Screen, with a diameter of 3.8 cm is used for visual identification of the beam position, as seen in Figure 3.2b. The beam location and focus are adjusted through optics integrated in the electron gun. Figure 3.2a illustrates the energy spectrum of the electron gun as observed by the facility's electron spectrometer, a retarding potential analyzer (RPA), for a nominal electron beam energy of 800 V. The energy spreading visible in this plot is a result of some energy spreading within the electron gun, but primarily due to effects within the RPA. Reference [14] describes an analysis of in-RPA energy spreading, and finds that  $\approx 20$  V of spread is expected at potentials of 1000 V. The results shown in Fig. 3.2a are therefore consistent with a well-homogenized beam, with very little energy spreading not explained by the detector physics.



(a) RPA trace of electron beam set to 800V



(b) Phosphor screen illustrating the size and shape of the electron spot in blue. The RPA is mounted to the right of the screen [131].

Figure 3.2: Electron beam characteristics

### 3.1.1 Broad spectrum electron gun

A unique capability of the facility here is a broad spectrum electron gun, capable of mimicking the electron environment in a space plasma. This device was developed in the course of this work along with Miles Bengtson. Unlike traditional electron guns which generate monoenergetic beams, this device is designed to emit electrons at a range of energies simultaneously, currently at energies up to 14 keV. The physics, mode of operation and design of the system are described in detail in Reference [13]. This capability enables valuable investigations that cannot be adequately simulated through the use of monoenergetic electron beams, such as evaluating the emission of x-rays from a target due to the plasma environment, or investigating the charging behavior of a material under space-like electron environments.

Figure 3.3 illustrates sample spectra generated from this electron gun, distributing electrons in a wide range of energies compared with the rapid drop seen for the monoenergetic spectrum in Figure 3.2a. This generates an electron flux approximately two orders of magnitude greater than a comparable orbital environment, enabling material aging and exposure studies to be conducted in an accelerated manner. The spectra can be tuned to match a desired curve shape, and the maximum energy can likewise be adjusted. Work is underway to test the device at up to 30 keV emission energies, with plans for a maximum energy of 200 keV in future iterations.

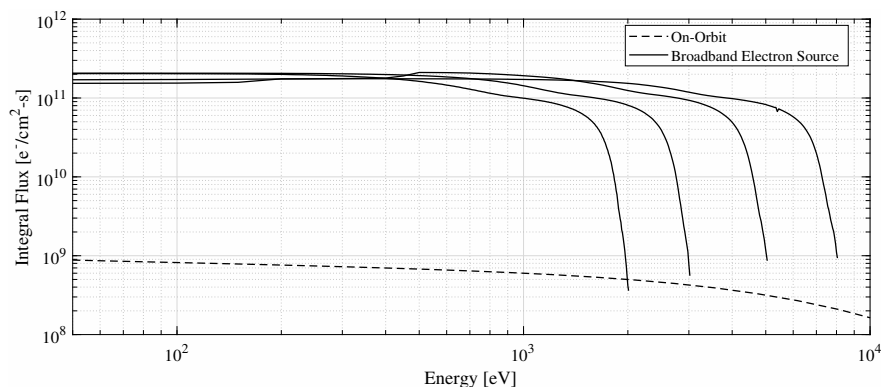


Figure 3.3: Output spectra for broad-spectrum electron gun set to different energies.

### 3.1.1.1 Principle of operation

Figure 3.4 shows a schematic of the electron gun design. Ultraviolet light is used to stimulate photoelectron emission from inside a hollow tube, which consists of a series of  $n$  individual circular stages. The stages are each held at different potentials and are stacked together with thin insulators in between each stage for electrical isolation. The circular shape of each ring acts like an Einzel lens to focus the electrons toward the center of the device and into a beam. Each stage being held at a different potential sets up an electric field along the length of the device that accelerates the electrons toward the aperture. The forward most stage is at zero potential, which contains the electric fields within the device. The rearward most stage has a grid placed over the aperture which allows the UV light to shine in while also containing the electric fields. Each electron is generated on a stage at a given negative voltage, then accelerated toward the front of the device which is grounded. Therefore, the final energy of each electron is equal to the negative voltage of the stage on which it was generated. This design enables the device to emit an electron beam with a total number of energies equal to the number of stages.

In theory, the maximum energy electron capable of being produced by the broad-spectrum source is limited only by the maximum voltage which a power supply can provide. Commercially-available power supplies are available which output voltages up to the hundreds of kV range. Linacs, cyclotrons are other types of accelerators that do not rely on static electric fields to accelerate charged

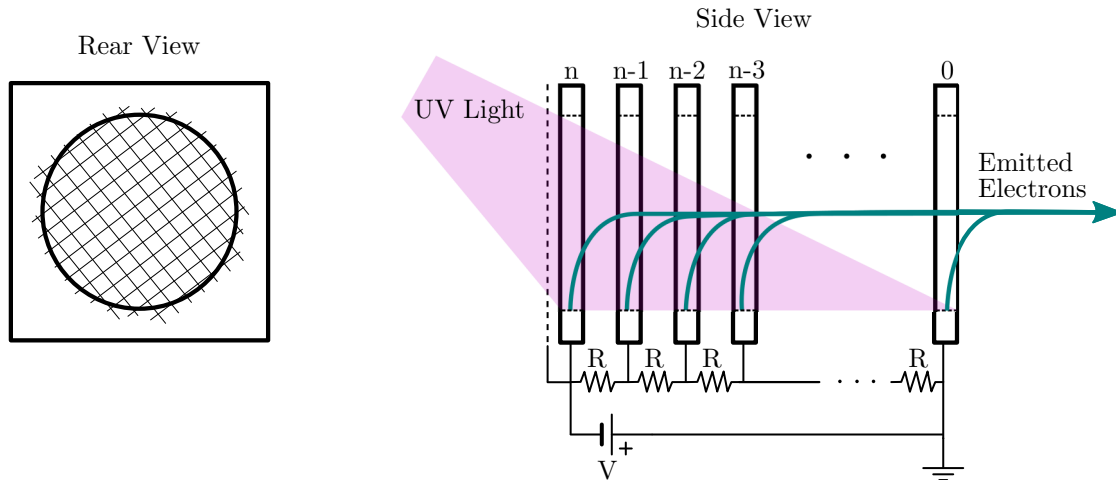


Figure 3.4: Schematic of the broad-spectrum electron gun design and operation. The side view shows how the voltage gradient is applied to the stages and how the UV light is used to stimulate photoelectron emission from each stage. The rear view shows the shape of each stage with a grid to contain the electric fields on the rearmost stage only.

particles are generally required to generate particle fluxes in the MeV range [158]. Therefore, it is expected that the broad-spectrum gun design would be capable of producing electrons in the range from eV to hundreds of keV. This range is highly relevant for spacecraft surface charging, material degradation, and instrument calibration purposes.

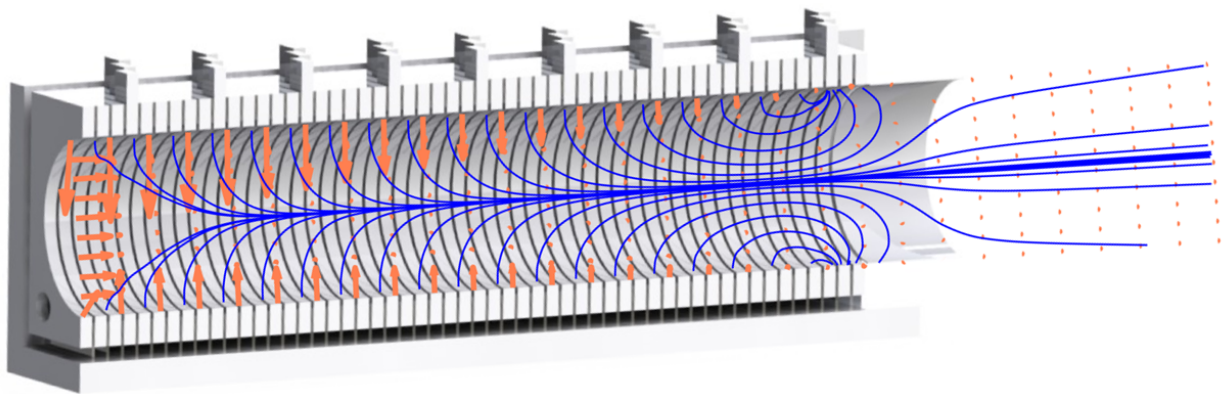


Figure 3.5: Electric field streamlines (blue) and electric field (orange arrows) imposed on the electron gun CAD model with 54 discrete stages.

### 3.1.1.2 Device prototype

A prototype has been constructed which consists of 54 aluminum stages with thin Delrin insulators in between each stage, yielding a near-continuous approximation of a spectrum. A CAD model of the broad-spectrum source is shown in Figure 3.5, with orange arrows indicating electric field vectors and blue lines indicating electric field streamlines. Pictures of the device are shown in Figure 3.6 and 3.7. 10 M $\Omega$  space-rated resistors are used in the voltage divider circuit. The large resistances were selected to keep the current draw from the power supplies low. A Hamamatsu L10706 vacuum ultraviolet light with a deuterium bulb (not pictured) is used to stimulate photoemission inside the tube. This source emits across a distribution from 115 to 400 nm, with a primary peak at 161 nm or 7.70 eV [60].

The broad-spectrum gun outputs a series of discrete electron energies, and using more stages leads to a better approximation of a fully-continuous spectrum. Using more stages also reduces the voltage step in between each stage, therefore reducing the likelihood of arcing between stages. For example, if a maximum voltage of 30 kV is applied to the rearmost stage and only 10 stages are used, there is a 3 kV potential difference between adjacent stages if all resistors are sized equally. However, if 100 stages are used, the potential difference between stages is only 300 V, which significantly reduces the risk of arcing between stages. The downside to adding more stages is that it increases the mechanical design and integration complexity, though compared to many scientific sources and detectors, the broad-spectrum electron gun is still a relatively straightforward device. The 54 stage prototype is approximately 33 cm long with a 6 $\times$ 6 cm cross section. In its current form, the entire device must fit inside the vacuum chamber. Future iterations will be flange-mountable so that the gun will be installed on the outside of a vacuum chamber.

A patent for this device is currently pending.

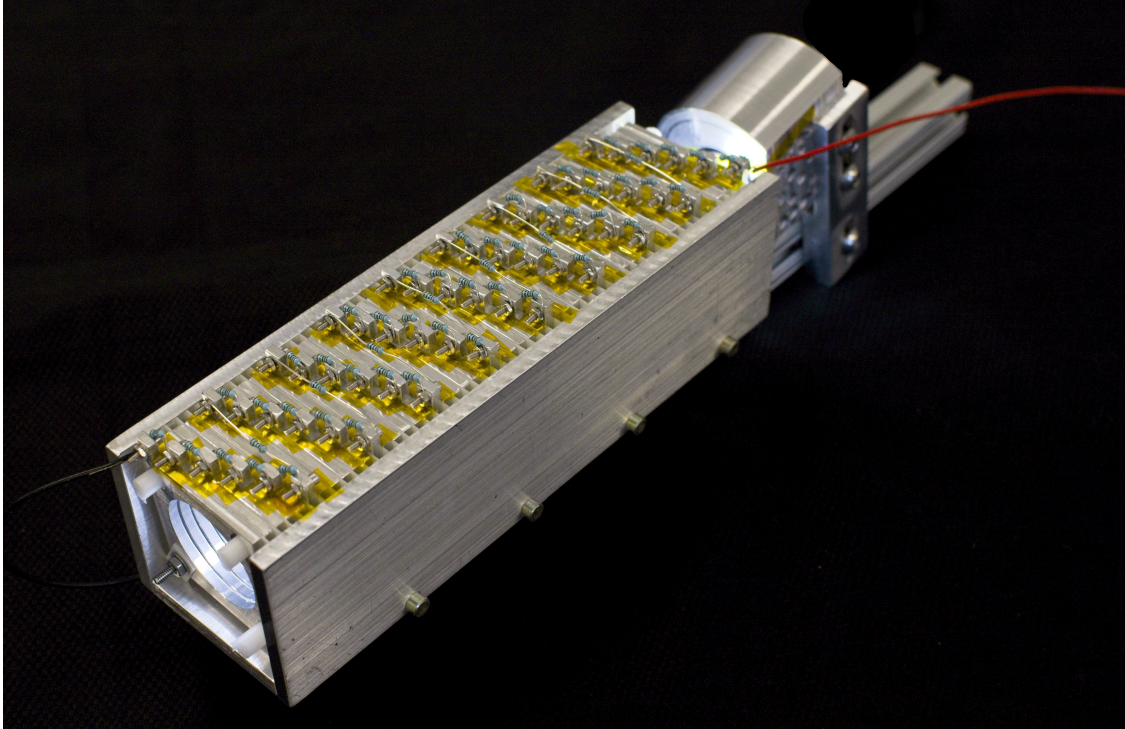


Figure 3.6: Prototype of the broad-spectrum electron gun with 54 discrete stages.

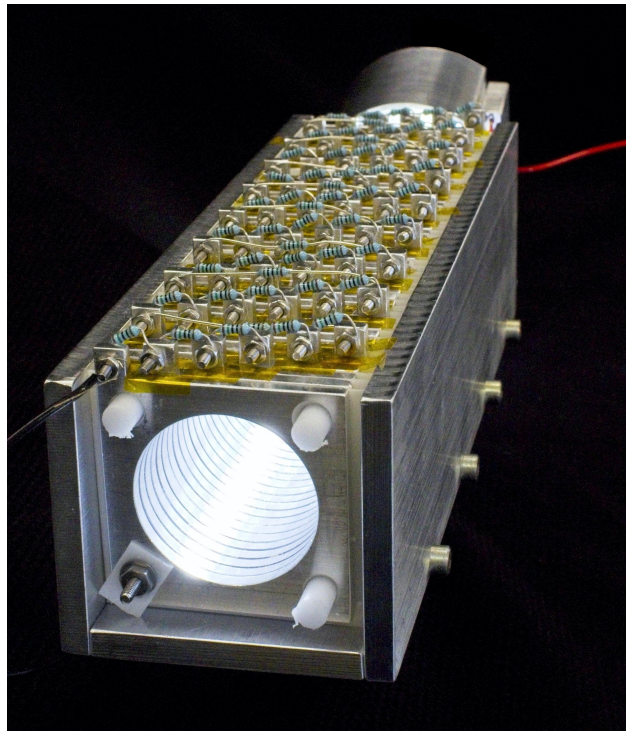


Figure 3.7: Front view of the broad-spectrum electron gun.

### 3.1.2 Probes

A series of sensors are used to ensure nominal operation of the chamber, and are not specific to any particular experimental configuration. These include an Agilent IMG-100 for high vacuum pressure measurement below  $10^{-3}$  Torr, and an Agilent ConvecTorr gauge for high pressure measurement from atmosphere to  $10^{-4}$  Torr. Both gauges are controlled by dedicated cards in an Agilent XGS-600 gauge controller, and in tandem can provide accurate measurements of chamber pressure for the full range of obtainable pressures. Pressure gauges are complimented by a residual gas analyzer to monitor species in the chamber. Additionally, cameras are used to monitor and provide feedback on the position of in-chamber elements, while a phosphor screen is used for visual validation of electron beam alignment.

A Stefan-Mayer 3-axis FLC3-70 fluxgate magnetometer is used to measure magnetic fields in the range of  $\pm 200$   $\mu$ T and DC to 1 kHz. This instrument is compact, a cylinder just 3 cm in length and 1 cm in diameter, and vacuum rated for operation within the chamber. A full characterization of the magnetic field environment in the chamber is planned.

In addition to these system-level instruments, there are three probes which are used extensively in the course of conducting experiments in the chamber, and so are treated in more detail: a residual gas analyzer, an electron energy analyzer, and an x-ray spectrometer. The translation system used to position components in the chamber is also discussed here.

#### 3.1.2.1 Residual gas analyzer

A Stanford Research Systems residual gas analyzer with a 200 amu range (SRS RGA-200) is used to monitor the molecular environment in the chamber during operations, and can provide useful diagnostic information in cases of high outgassing. This case is observed during extended stepper motor operation, as the motors heat up. Figure 3.8 illustrates a sample spectrum collected during nominal chamber operation after using the turbomolecular pump for 12 hours. Chamber base pressure at this time was  $1.6 \times 10^{-6}$  Torr; the lowest chamber base pressure observed has been

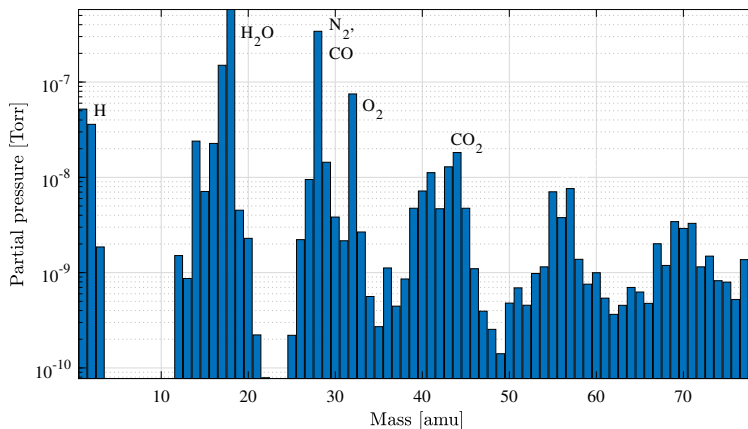


Figure 3.8: RGA spectrum from 0-80 amu.

$\sim 5 \times 10^{-7}$  Torr after an extensive remodel and cleaning process. Several significant contaminant species are labeled on the RGA spectrum, with air constituents ( $N_2$ ,  $O_2$ ,  $CO_2/CO$ ) and water vapor ( $H$  and  $H_2O$ ) being the most significant. These species account for over 70% of the residual partial pressure in the chamber at this time. Partial pressure contributions for species over 80 amu are typically on the order of  $10^{-9}$  Torr, and have a relatively uniform pattern consistent with a “hydrocarbon forest” of high mass species. These are likely the result of residual oils from machining processes, as well as oils from pumps and off gassing plastics, which are used only sparingly.

The residual carbon-bearing species have been observed resulting in brown discoloration on the phosphor screen, a result of Electron-Beam Induced Deposition (EBID) of those species onto the screen. This effect has also been observed after extended, low-energy use of the electron gun on aluminum target plates.

The pumps used for this system enable pumping down from atmosphere to  $\sim 10^{-6}$  Torr in under 3 hours, enabling rapid advancement of experimental campaigns. While these pressures are acceptable for any equipment in the chamber, the occasional EBID of carbon-bearing species during electron beam use may lead to the addition of getter plates in the future to reduce the partial pressure of high mass residual species. Alternatively, a bake out system may be used to improve pump down performance instead, and reduce residual contaminants in the chamber.

### 3.1.2.2 Electron spectrum measurement

A custom electron energy analyzer has been built for the ECLIPS facility. The electron energy analyzer is a gridded Faraday cup design with a 1.2 cm diameter circular aperture. The device consists of a front grounded grid and a second discriminating grid to which high voltages are applied. The discriminating grid creates an approximately equipotential plane and the front grid contains the electric fields inside the instrument. When no voltage is applied to the discriminating grid, an electron with any energy can pass through the instrument and into the detector. As a negative voltage,  $V$ , is applied, electrons with energies less than  $eV$  cannot overcome the potential barrier and thus are repelled from the detector. Thus, by sweeping through voltages applied to the grid, the electron energy distribution is obtained. The collector itself is a hollow cylinder closed at the back which helps to prevent secondary or backscattered electrons generated on the collector surface from escaping out the front of the instrument [14]. The current is recorded using a Keithley 2401 SourceMeter picoammeter and one of the high-voltage power supplies is used to apply voltages to the discriminating grid. Several noise floor measurements have been taken in which the electron energy analyzer is installed in the chamber, but none of the sources are turned on, so there is no source of electrons. The measured noise current of the electron energy analyzer and picoammeter system has a mean of 0.01 nA and a standard deviation of 0.03 nA. A full description of this system and its performance is available in Reference [14].

### 3.1.2.3 X-ray spectrometer

X-ray spectrum measurement is achieved through the use of an Amptek X123 X-ray spectrometer with a 6 mm<sup>2</sup> Si-PIN diode sensor. This unit is compact as seen in Figure 3.10, lightweight and low-power, which reduces the amount of heat that must be removed from the system when operating in the vacuum chamber. In addition, this detector has spaceflight heritage as the primary instrument on the Mini-XSS solar observatory mission [104]. Detector calibration was accomplished in atmospheric conditions with an Fe-55 radioisotope source. This isotope emits X-rays at two ener-

gies, 5.89 and 6.49 keV, which are used to create a linear calibration for the detector under specific operating settings. The detector also has a 0.0254 mm thick beryllium frontal window. This beryllium window prevents stray photons from entering the detector, effectively attenuating any photons below 0.9 keV. In addition, the detector efficiency also decreases as the energy increases above 12 keV, due to photons passing through the active volume of the Si-PIN detector without depositing all of their energy [3]. Photon saturation and spectral distortion due to pile up effects can occur in the detector for count rates above  $\sim 20000$  photons per second, so the electron beam currents are minimized during tests to avoid this count region. The effective sensing region for the detector is approximately 1-30 keV, with an energy resolution of 140 eV FWHM at 5.9 keV [3].

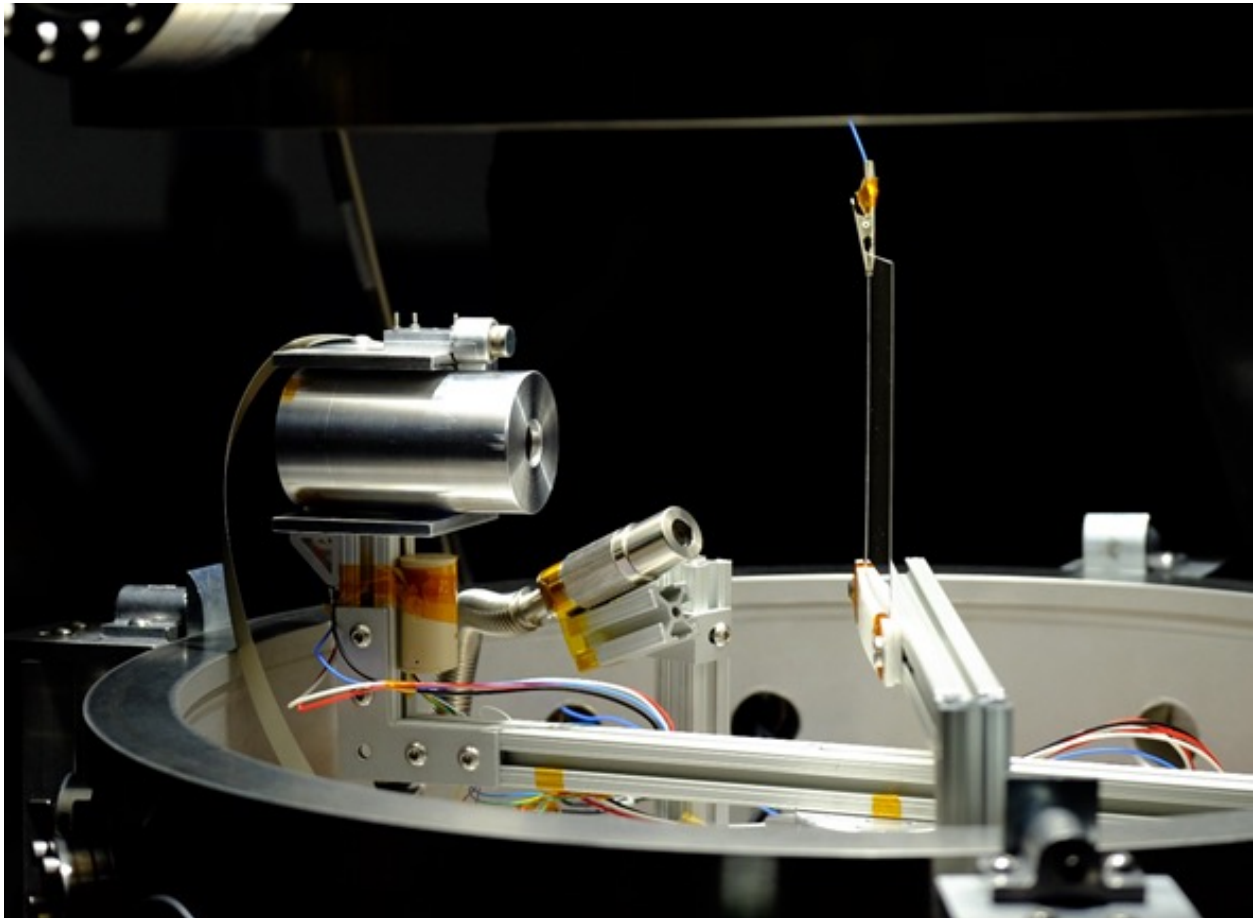


Figure 3.9: Example experimental setup in chamber. RPA and x-ray detector seen on the left, VUV light in center, and target Inconel plate connected to a HVPS on right.

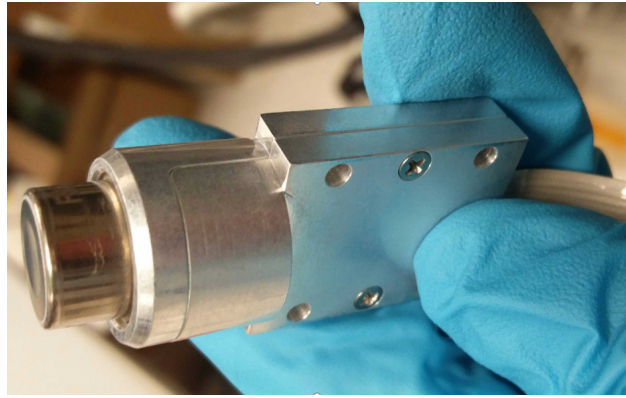


Figure 3.10: Amptek X123 detector.

A significant challenge in operating in a vacuum environment is thermal dissipation, due to the lack of convection. Additionally, experimental setups which require a sensor to be mobile typically have poor thermal conductive pathways to the chamber walls or other large heatsinks. The noise threshold of the detector increases with increasing temperature, so an integrated thermoelectric cooler is used to maintain acceptably low noise levels. However, larger temperature differentials between the diode and the ambient environment requires higher amounts of power, which in turn increases the amount of heat which must be dissipated.

For these experiments a temperature of 240 K was maintained at the diode. While this represented somewhat higher noise and reduced resolution relative to the minimum achievable temperature of 210 K, the temperature could be maintained for over 1 hour at a time in the vacuum environment without running into thermal saturation of the heat sink. In most experimental configurations, the relatively massive 200 g aluminum housing of a retarding potential analyzer serves as a heat sink while enabling simultaneous electron and x-ray spectrum measurements. Therefore, long duration sweeps and experiments could be conducted without detector characteristics varying during testing.

### 3.1.3 Motion stages

Many experiments conducted in the ECLIPS facility have geometrical dependencies, whether a desire to sample electron populations at different points relative to a target, or examine the structure of a spacecraft wake under different charging conditions. This led to the development of a unique 3-axis translation system, with axes moving according to cylindrical coordinates, shown in Fig. 3.11. A Newmark Systems RM-3 rotational stage is mounted on the base. Custom-built linear stages using the same vac-safe stepper motors as the Newmark Systems RM-3 rotary stage are mounted horizontally or vertically on the rotational stage, allowing for any arbitrary movement of be conducted in the chamber. The cylindrical design was chosen to maximize the use of space within the cylindrical chamber, allowing translations right up to the chamber walls in each direction. The position of each stage is measured by linear and rotary high-vacuum Renishaw Tonic encoders<sup>1</sup> with 5  $\mu\text{m}$  resolution. The encoders are connected to the LabView interface, and feed a closed-loop position control.

The steppers quickly warm up during operation in vacuum, outgassing primarily water with some contribution from carbon dioxide. For this reason, an Agilent XGS-600 vacuum gauge controller<sup>2</sup> connected to the IMG pressure sensor keeps track of the pressure in the chamber and disconnects the steppers when a predetermined threshold is reached. This is important to ensure a safe operation of delicate components, such as electron or ion sources, rated for use only below  $10^{-6}$  Torr.

### 3.1.4 Power systems

A major focus of chamber research is on spacecraft charging, and in particular the detection of charging remotely. This requires the ability to control the potential of a range of systems, from the RPA grids to a target plate, simultaneously. Therefore, a series of power supplies are integrated into the chamber facility, as seen in Figure 3.12. Two Matsusada AU-30R1 high voltage power

---

<sup>1</sup> <https://www.renishaw.com/en/tonic-encoder-series--37824> (Consulted on 11/23/2020)

<sup>2</sup> <https://www.agilent.com/en/product/vacuum-technologies/vacuum-measurement/gauge-controllers/xgs-600-vacuim-gauge-controller> (Consulted on 11/23/2020)

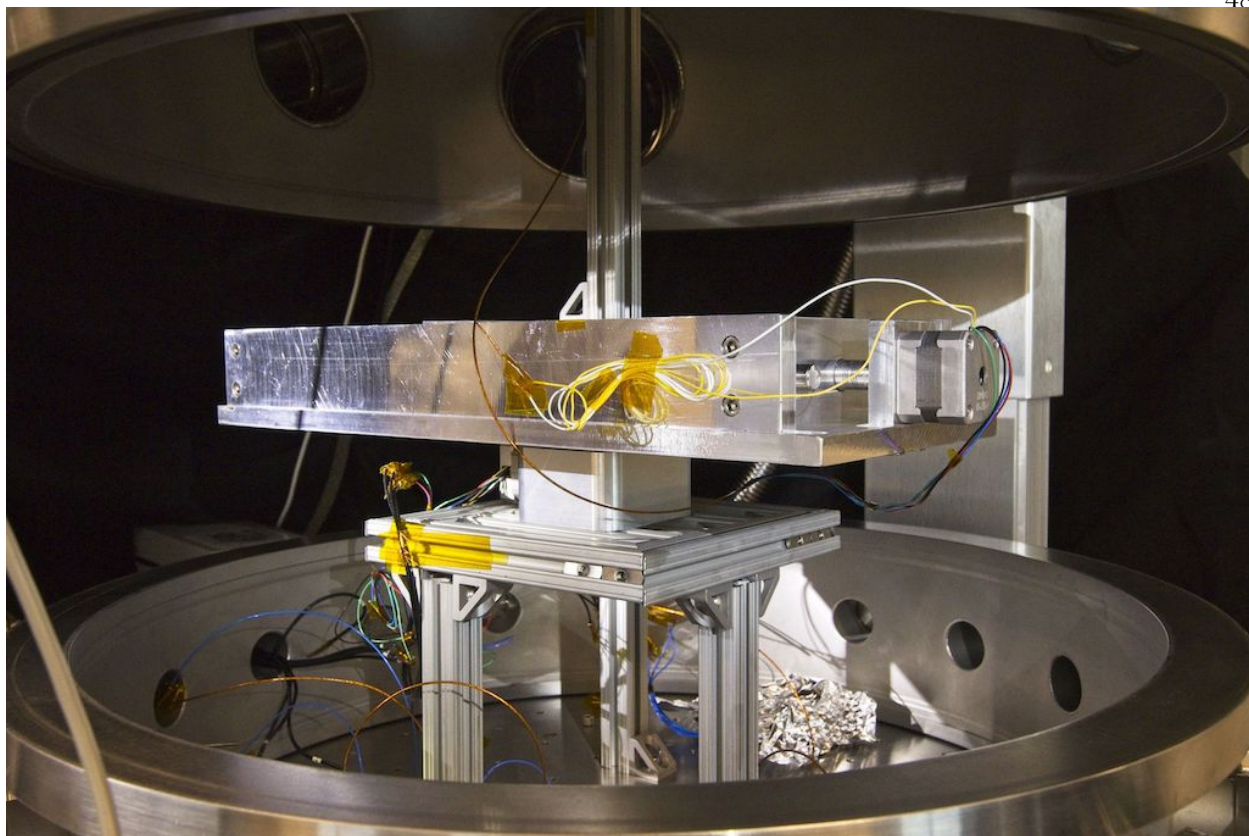


Figure 3.11: Rotational stage (center) with translational stage mounted atop it.

supplies (HVPS) provide high quality potentials up to 30 kV. These units are controlled via fiber optic connections to the primary computer, reducing the potential for interference. In addition to the Matsusada power supplies, several other HVPS units are available for experiments, including two Spellman CZE2000 units with a maximum voltage of 30 kV, and two SL300 high current power supplies with a maximum voltage of 3 kV at up to 300 Watts.

Monitoring of potentials up to 1000 V is achieved through a Kiethly DMM6500, while a Keithley 2401 SourceMeter picoammeter is used to monitor current. Both are computer controlled, enabling rapid measurements and development of control VIs that can feedback on detected currents or potentials. Additionally, a low-voltage power supply, Keysight E3631A, is used to provide power for stepper motors.

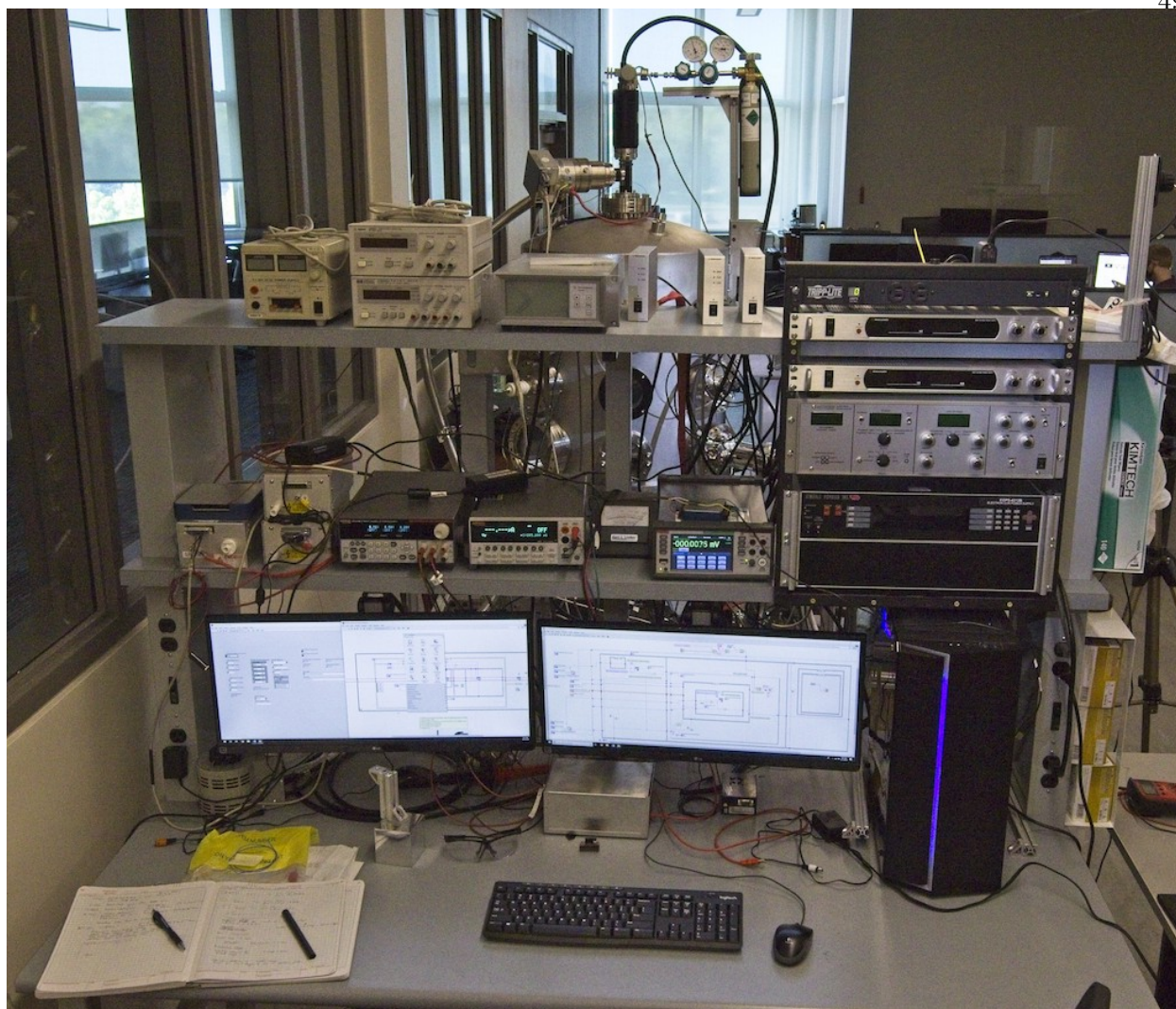


Figure 3.12: Power supplies and control infrastructure for the chamber. The server rack at top right contains HVPS, and controllers for the electron and ion guns.

### 3.2 Bremsstrahlung-based potential sensing tests

Two major test campaigns are conducted in the ECLIPS facility to evaluate the efficacy of the bremsstrahlung-based potential sensing method experimentally. Both test setups consist of an electron beam impinging on a target plate while the x-ray spectrometer observes the resulting x-ray flux. The potential of the target plate is controlled by a Matsusada AU series, 0-30 kV range high voltage power supply. The first set of tests involve the x-ray detector moving in an arc relative to a stationary target plate and electron beam, providing a measure of the x-ray spectrum

at a series of positions, which prior literature suggests could have a significant impact on the sensed spectrum [7, 89]. This effect is due to the directional nature of bremsstrahlung radiation, as discussed previously in Chapter 2.



Figure 3.13: Electron beam focused and aligned to center of Ti target plate.

The second test involves the plate rotating while the positions of the electron gun and spectrometer are held fixed. This is analogous to a scenario where a target body may be rotating relative to a servicing spacecraft, but the servicer electron beam and sensor are both in fixed positions.

The phosphor screen is fixed to the center of the plate, which is mounted to a motorized rotary stage. This stage enables 360° rotation of the plate while angular position feedback is provided by a rotary encoder with an accuracy better than 0.01°. This enables highly accurate, repeatable positioning of the plate. The phosphor screen allows the electron beam focus and positioning parameters to be dialed in to ensure the beam hits the center of the plate when the plate is normal to the beam. However, the plate is held at an elevated potential between -100 V and -2000 V for these tests, which results in a deflection of the electron beam as the plate is rotated away from a perpendicular orientation. The electron beam is focused to an approximately 1 cm diameter spot size, as seen in Figure 3.13.

Reference [131] provides both a theoretical and experimental investigation into electron beam deflection in the region of charged bodies, but is beyond of the scope of this work. Instead, characteristic peaks are monitored to evaluate if the electron beam is properly impacting the target plate, or radiation characteristic to the stainless steel chamber walls is generated instead. Runs contaminated with stainless steel characteristic peaks are therefore discarded, as such false readings

are an artifact of the experimental setup.

For data collection, the target plate is rotated at 10 degree increments from  $-60^\circ$  to  $+80^\circ$ , where the plate perpendicular to the incident electron beam is taken as  $0^\circ$ . Because of the relative orientation of the electron beam, the plate, and the x-ray detector, angles beyond this range resulted in spectra contaminated with x-rays generated either at the chamber walls, or the wrong side of the target plate for the x-ray detector to observe. The relative geometry of this experimental configuration is shown in Figure 3.14. Electron beam energies ranging from 3 keV to 20 keV are used, while beam currents were kept at 1-5  $\mu\text{A}$  to avoid detector saturation and pileup effects.

The materials tested in this work consist of 15 cm square samples of titanium, 6061 aluminum, and 625 Inconel, all materials commonly found in spaceflight applications. Each of the elements in these materials contains unique characteristic x-ray peaks, which have a fixed energy. In addition to evaluating elemental composition of the target, these peaks are used to evaluate detector performance, which is affected by diode temperature, detector gains, or other calibration parameters.

### 3.2.1 Data processing

An example spectrum from an Inconel target collected by the X-123 detector is shown in Figure 3.15. As previously discussed, the characteristic peaks are used to provide elemental composition information, while also providing insight into detector performance. Additionally, the line of fit method for landing energy estimation must be fit to bremsstrahlung spectra, and becomes less accurate if characteristic radiation is included as well. These peaks are identified through peak finding algorithms. These algorithms are sensitive to noise, which effectively imposes a series of peaks through the spectrum, so a smoothing algorithm is used to improve SNR prior to evaluating peaks.

A frequency analysis of the raw spectrum data taken from the spectrometer revealed that, as with many instruments, the signal is predominantly low-frequency while the noise is a high-frequency contribution. While frequency is typically used to refer to samples taken in time, in

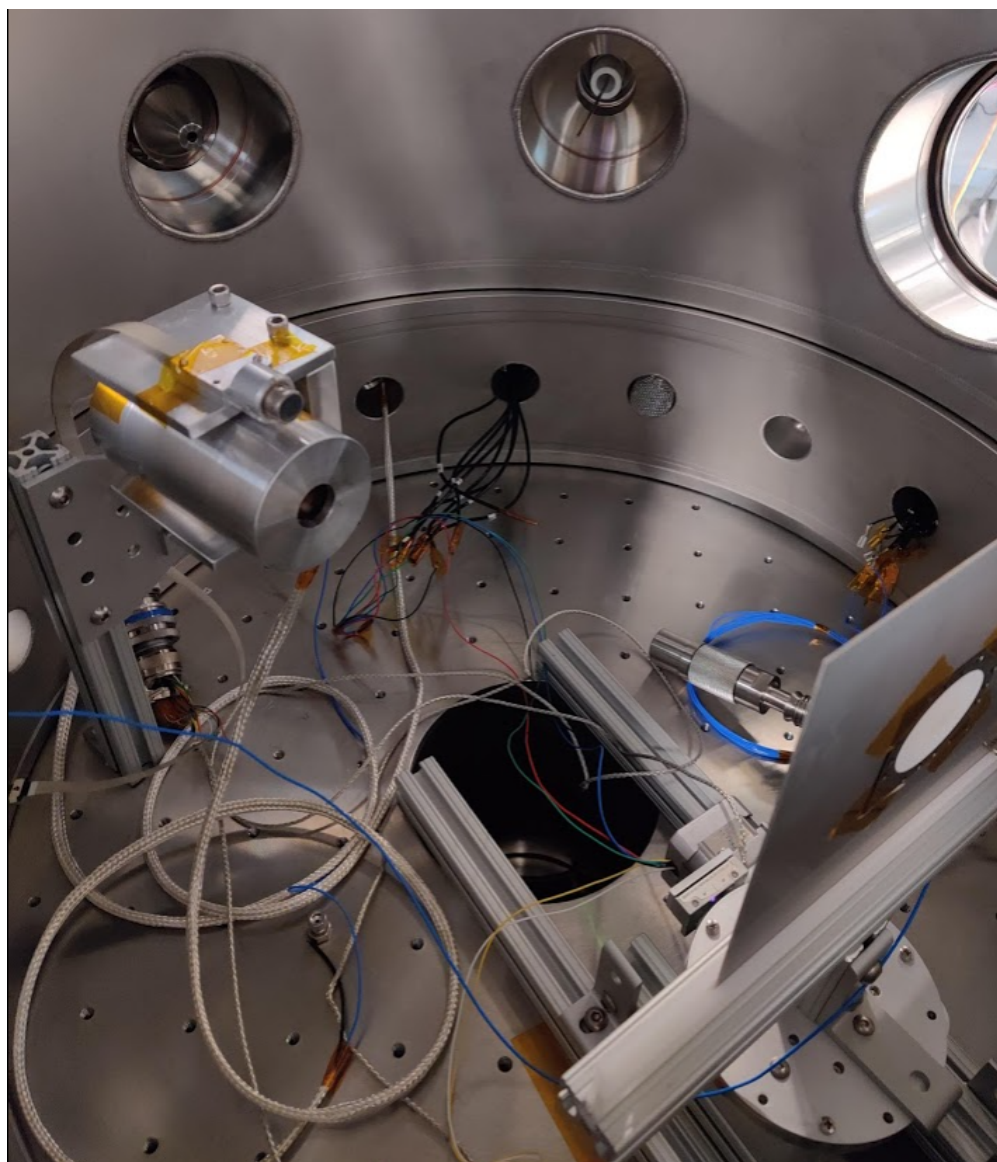


Figure 3.14: Top-down view of the experimental setup with a rotating target plate. The electron gun is mounted to the top left port, just above the x-ray detector.

this case the samples are taken in energy, with a high variability between adjacent bins indicating high frequency noise contribution. Longer-scale evolution in the underlying signal that span a series of bins, such as characteristic peaks and the bremsstrahlung continuum, are low frequency by comparison. Therefore, a low pass filter became an evident choice for smoothing the data, with a passband evaluated based on the frequency-space plot shown in Figure 3.16. A normalized frequency cutoff of 0.144 is used to preserve the 99% occupied bandwidth. The integrated Matlab filter design functions were used to design a low pass filter with a 0.1 relative frequency cutoff, and with zero phase to ensure the filter output would not lag the sampled data to preserve peak locations.

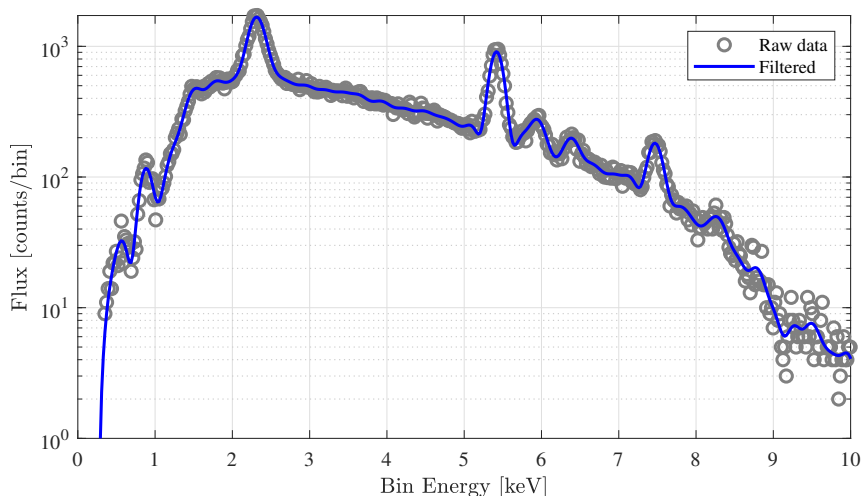


Figure 3.15: X-ray spectrum from 10 keV beam on an Inconel target, as received and after lowpass filtering.

A peak finding algorithm is then used to determine the locations of characteristic peaks in the smoothed spectrum, with a minimum prominence requirement to reduce the incidence of false positives. For a spectrum of an alloy like Inconel, there are a range of peaks from different elemental constituents as seen in Figure 3.15, which can be used either for material identification or detector validation if the material is known. Table 3.1 illustrates the identities of the major peaks in the Inconel spectrum, along with the source element and the composition of that element in the sample. Although this experimental setup is not optimized for material analysis, it is still readily capable

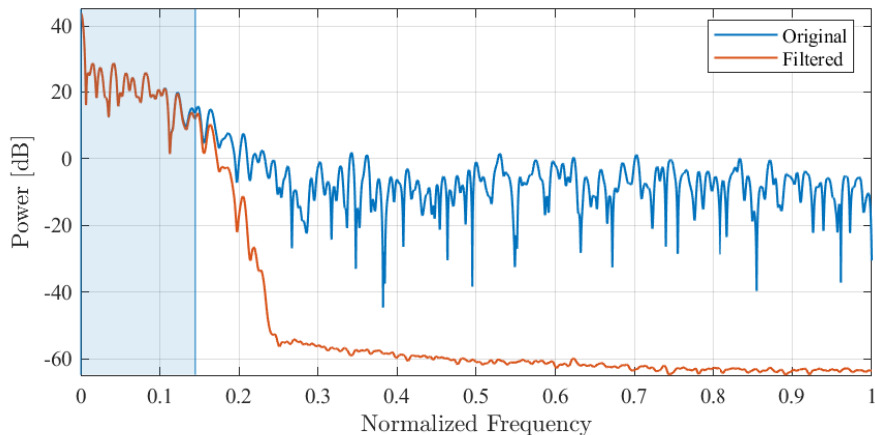


Figure 3.16: Power spectrum plot for spectrum from 10 keV electrons on Inconel. Filter bandwidth was set to 0.144 to preserve the 99% occupied bandwidth, shown in blue highlight.

of identifying constituent elements with concentrations of under 1% in the sample.

After removing the characteristic radiation peaks from the data, it is possible to use the remaining bremsstrahlung continuum to determine the landing energy of the electrons, and thus infer the relative potential of the surface. As discussed in Chapter 2, the landing energy is determined by fitting a line to the upper energy portion of the spectrum, as seen in Figure 3.17. The interception of this line of fit with the energy axis represent the landing energy, while the statistical uncertainty in the fitted line provides a measure of uncertainty in the landing energy estimate.

### 3.2.2 Rotating detector tests

The driving motivation for conducting such an extensive set of tests was the expectation through the literature of a dependence between detected bremsstrahlung spectrum and the angular separation between the detector and electron beam. In a flight implementation of this system, minimizing the angular separation between the detector and the electron source avoids complexities associated with deployable structures, but prior work and existing bremsstrahlung literature suggested large separations may be necessary to achieve accurate spectral measurements.

The experiment was configured as seen in Figure 3.18, with the x-ray sensor mounted on

Element	Energy [keV]	Transition	Relative abundance in target [%]
Cr	0.57	$L_{\alpha}, L_{\beta}$	20
Ni	0.85-0.87	$L_{\alpha}, L_{\beta}$	58
Mo	2.29-2.39	$L_{\alpha}, L_{\beta}$	9
Nb	2.16-2.25	$L_{\alpha}, L_{\beta}$	4
Cr	5.41	$K_{\alpha}$	20
Cr	5.94	$K_{\beta}$	20
Fe	6.40	$K_{\beta}$	5
Ni	7.47	$K_{\alpha}$	58
Ni	8.26	$K_{\beta}$	58

Table 3.1: Elemental sources of the dominant peaks in the spectrum shown in Figure 3.15, along with the relative abundance by mass of each element in the Inconel 625 sample per manufacturer's test report. The remaining 4% composition consists of trace elements without distinct peaks in this energy range and rounding in abundances.

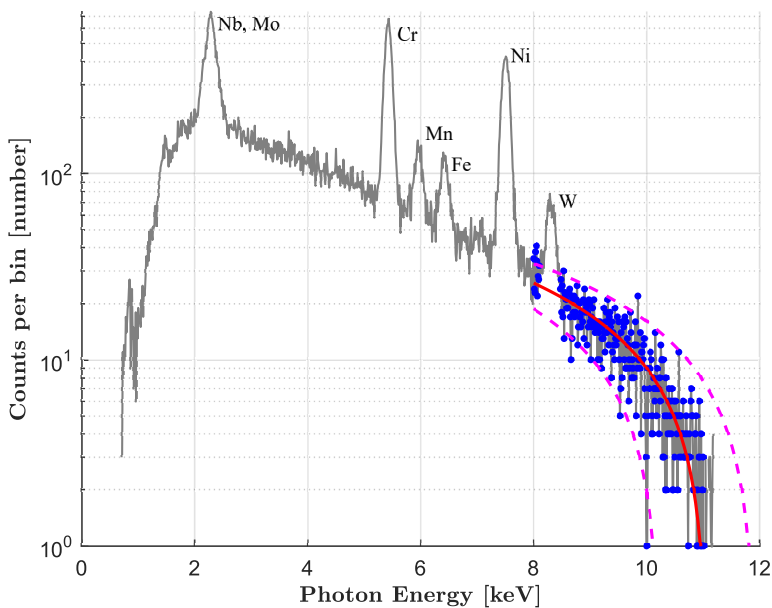


Figure 3.17: Determination of landing energy from x-ray spectrum, with characteristic peaks identified by element.

the end of a 20 cm long aluminum arm attached to the rotary stage. The rotational axis of the stage passes through the center of the target plate. The reference position is found when the x-ray detector is perpendicular to the target plate, aligned with its center. The electron beam is likewise aligned to the center of the target plate, and the plate is oriented perpendicular to the beam. The



Figure 3.18: Experimental setup for fixed plate, rotating sensor tests.

detector is located  $\sim 2$  cm below the centerline of the beam, and is wrapped tightly in aluminum foil to avoid interference from the beam; the detector is grounded to the chamber structure, which in turn is connected to the building ground.

The aluminum foil shielding for the detector cable and housing is essential to achieving reliable spectra at beam energies above 5 keV. Prior testing without the shielding resulted in highly distorted spectra above 5 keV, a nonlinear distortion effect which rendered many of these tests unusable. Electron beam interference is the suspected cause of these anomalies, and is successfully mitigated through proper shielding.

The range of angles that could be tested in this configuration is limited by the length of the detector ribbon cable. A range of  $-30^\circ$  to  $+30^\circ$  to each side of the electron beam is readily achieved.

No statistically significant relation ( $p = 0.45$ ) is found between angle of the detector and landing energy estimation error, using a Kruskal–Wallis test for analysis of variance of the data shown in Figure 3.21. This is an interesting finding, as the directional nature of bremsstrahlung

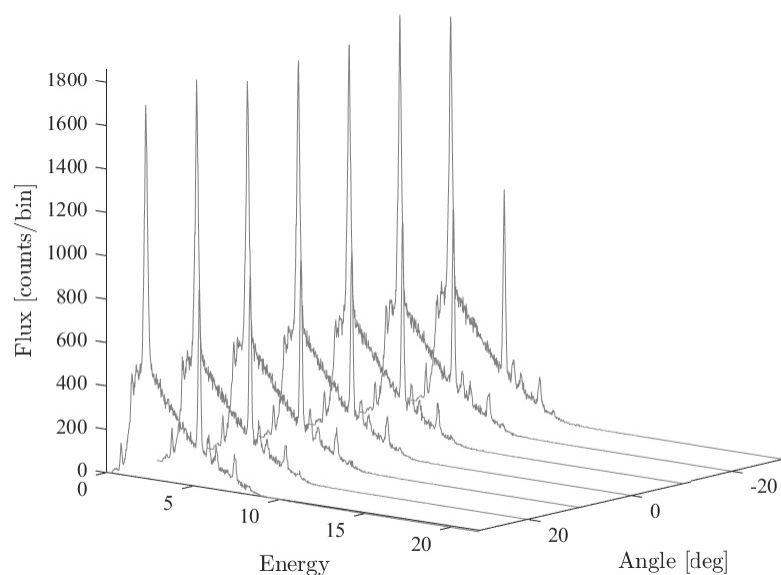


Figure 3.19: X-ray spectra observed for an Inconel plate at different angles relative to the incident 10 keV beam.

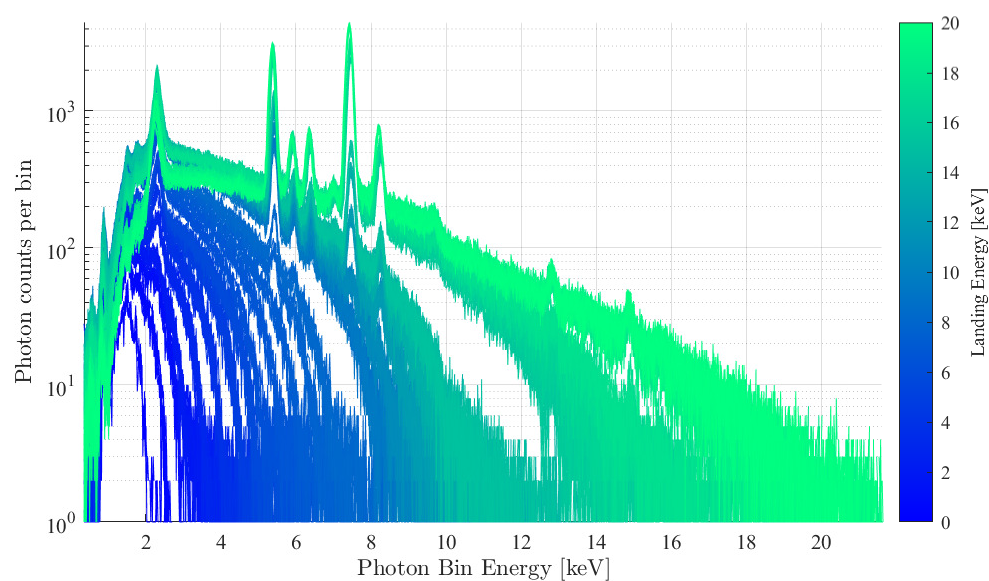


Figure 3.20: The full set of unprocessed x-ray spectra from Inconel. Note that although the landing energy changes the curve of each spectrum, the characteristic peak positions are fixed. Electron landing energies varied from 2.5-20 keV.

radiation is well established in the literature, as discussed in Chapter 2. However, much prior

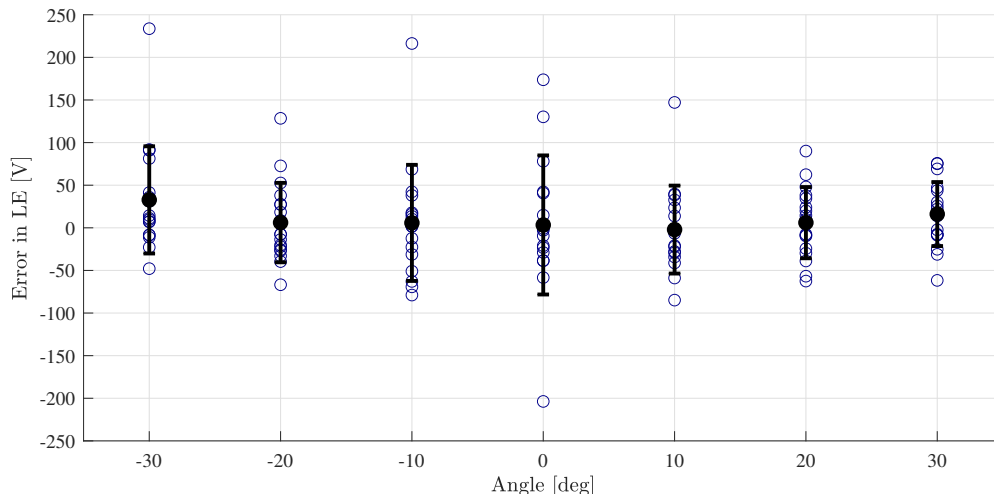


Figure 3.21: Landing energy errors vs detector-beam separation angle. Filled circles represent mean for each angle, error bars indicate  $1\sigma$  spread.

work has focused on thin films of material, where incident electrons experience only one interaction with the material prior to exiting the film. In contrast, this work focuses on comparatively thick samples, on the order of 1 mm, where the electron will be fully stopped in the material. In thick targets, Reference [55] finds that the resultant bremsstrahlung radiation to be near-isotropic, which agrees with the findings here. Reference [55] specifically finds that the bremsstrahlung directional anisotropy is significantly reduced as the photon energy falls below the limit where  $E_{\text{photon}} \approx E_{\text{electron}}$ . This work generalizes that conclusion further, to find that the angular anisotropy is statistically insignificant for determining the landing energy of an electron beam on a thick target in this observer range. This is a significant finding as early work on this topic including Reference [163] had suggested it may be necessary to utilize lengthy booms to achieve sufficient angular separation between the detector and the electron beam in order to characterize the electrostatic potential of the target. From these experimental results it is apparent that even in a co-linear case, sufficient spectral information is available for this method to be viable.

One possibility is that the admission angle of the x-ray detector is large relative to the range of angular positions evaluated in this experiment, negating any impact of the angle on landing energy estimation. The x-ray detector has a field of view of approximately  $45^\circ$  full width. However, the

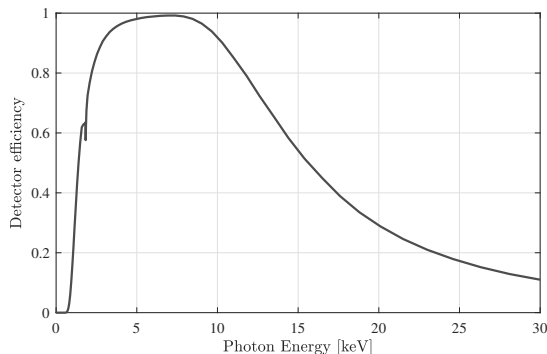


Figure 3.22: Efficiency of X-123 x-ray detector as a function of incident photon energy [3].

actual detector area is just  $6 \text{ mm}^2$ , which corresponds to a solid angle of  $1.5 \times 10^{-4} \text{ sr}$ . Therefore, despite the large field of view of the detector, the solid angle covered by the actual diode provides a high resolution assessment of the spectrum observed at a given angle.

Accuracy degrades at higher energies, as detector resolution decays and noise becomes more significant. Additionally, the detector efficiency decays with increasing energy above  $\sim 12 \text{ keV}$ , leading to an under count of high energy photons. However, the detector is still capable of returning spectra sufficient to achieve an accuracy of  $300 \text{ V}$  with a  $1\sigma$  resolution of  $\pm 550 \text{ V}$  for a  $20 \text{ keV}$  landing energy.

Detector efficiency curves are well known and provided by the manufacturer, as shown in Figure 3.22. This curve is used to scale the observed x-ray flux counts in each energy bin, account for known losses in the detector. This reduces mean errors from  $69 \pm 57\text{V}$  ( $1\sigma$ ) to under  $10 \pm 57\text{V}$  ( $1\sigma$ ), as seen in Figure 3.23.

There is a statistically significant relationship between the true landing energy and the percentage error in the estimate of landing energy. An ANOVA model is used to check for variance between the input variable, true landing energy, and the response variable, percent error in landing energy. These variables are shown graphically in Figure 3.24. The critical F-statistic for significance in this case, with 27 independent variable levels and 296 observations, is 1.679. The F-statistic returned by the ANOVA test is 126, indicating that there is a statistically significant relationship between the two variables ( $p < 10^{-5}$ ). The  $R^2$  statistic for a linear fit to the data is 0.3, indicating

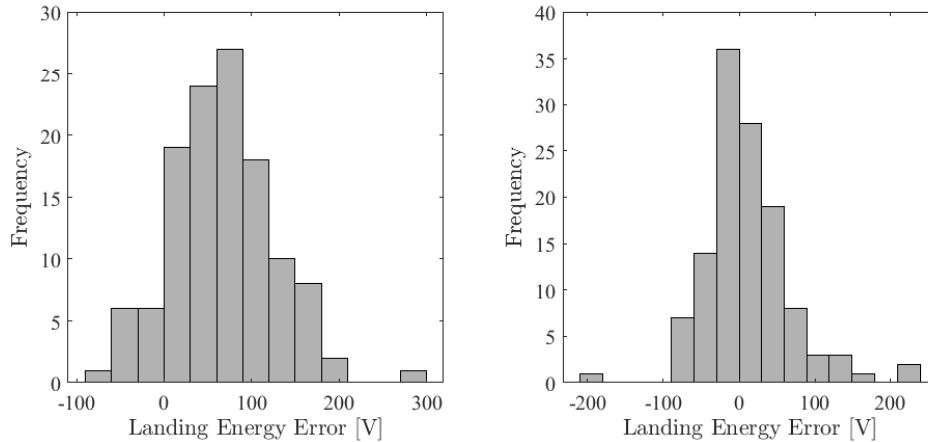


Figure 3.23: Error in landing energy for unprocessed spectra (left) and spectra where flux has been scaled according to detector efficiency (right). All runs had  $\leq 7\text{keV}$  beam energy, plate potentials 100-2000V. Both histograms have a 30V bin width.

only  $\sim 30\%$  of the variance in error is explained by a linear relation between the variables. This indicates that the normalized error in landing energy estimate changes as a function of the underlying landing energy, leading to less certain potential estimates as the electron landing energy increases. Despite this trend, the landing energy estimation accuracy is sufficient for proximity operations or rendezvous and docking applications according to the sensing requirements outlined in Section 2.1.

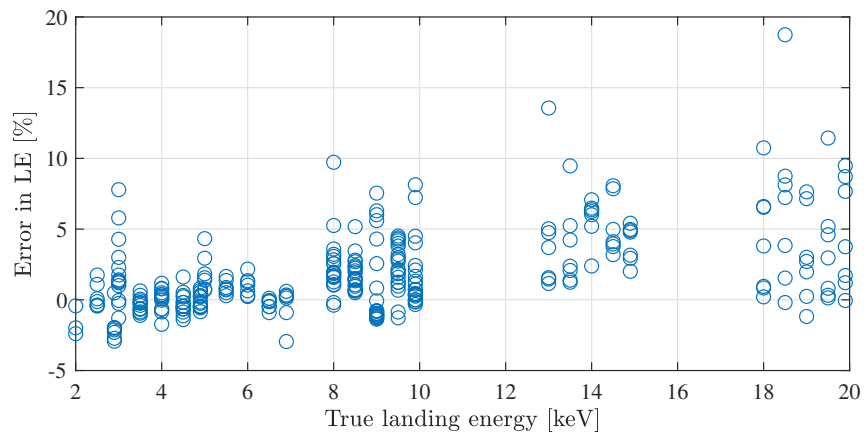


Figure 3.24: Relation between true landing energy and normalized error in the landing energy estimate. The slope of a linear regression to the data is 0.35 percent per keV.

Ultimately, the accuracy of the measurement method is  $10 \pm 57\text{V}$ ,  $1\sigma$  across the runs shown

in Figure 3.23, which covers 122 spectra collected at 3-7 keV, 1  $\mu\text{A}$  across the full angular range. Above 7 keV the method accuracy degrades, but even at 20 keV errors were found to be  $165 \pm 400\text{V}$ ,  $1\sigma$ . As shown in Figure 3.24, landing energy is a significant determinant in the accuracy of the estimation method. Ensuring that the landing energy is  $< 7$  keV for this detector can provide a better estimate of the landing energy, and therefore of the relative potential between the objects. This can be achieved by modulating the electron beam energy as a function of the relative potentials between the objects to maintain a consistent landing energy and therefore consistent potential estimation statistics.

### 3.2.3 Rotating plate

While the case with the rotating detector served to explore the impact of underlying bremsstrahlung emission on the accuracy of the sensing method, a case with a fixed detector and a rotating target is a more flight-like scenario, akin to a target rotating relative to an approaching servicer. Therefore, this scenario deserves experimental evaluation.

While the x-ray spectrum is not expected to evolve with angle, at grazing incidence angles the electron beam may miss the bulk of the plate and instead deliver significant current to the chamber walls. While the chamber is well grounded and the  $\mu\text{A}$ -level beam currents are unlikely to have any impact on the chamber potential, the resultant x-ray spectrum will be generated from a grounded target rather than the potential controlled plate. The spectra resulting from these interactions will be a combination of x-rays emitted from the potential controlled plate and the grounded chamber walls, encompassing multiple potentials that the methods presented here cannot account for.

For this test, the x-ray detector is mounted at a small ( $\sim 15^\circ$ ) angular separation from the electron beam, but at the same vertical height as the beam. The plate is rotated between  $+60^\circ$  and  $-80^\circ$ , a range which avoided the worst effects of beam deflection and chamber irradiation. The relative positions of the electron beam, sensors, and target plate are shown in Figure 3.14.

Much like the case with the rotating detector, an ANOVA regression did not find any statistically significant relation between angle and landing energy estimation error, supporting the null

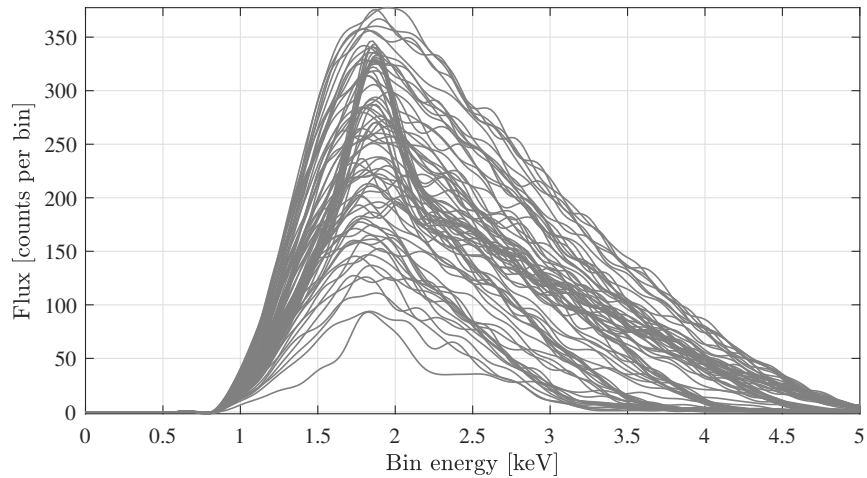


Figure 3.25: Spectra resulting from rotating target plate, fixed detector position for 5 keV beam on Ti target.

hypothesis that there should be no dependence (F-statistic of 0.875, corresponding to  $p = 0.354$ ). Therefore, an equivalent landing energy solution is found for any target orientation where signal is available. For this case limited by the geometry of the chamber and the near 2D plate, a usable signal was obtained for over  $100^\circ$  of the plate's  $180^\circ$  rotation, with the signal from another  $60^\circ$  contaminated by chamber wall interactions.

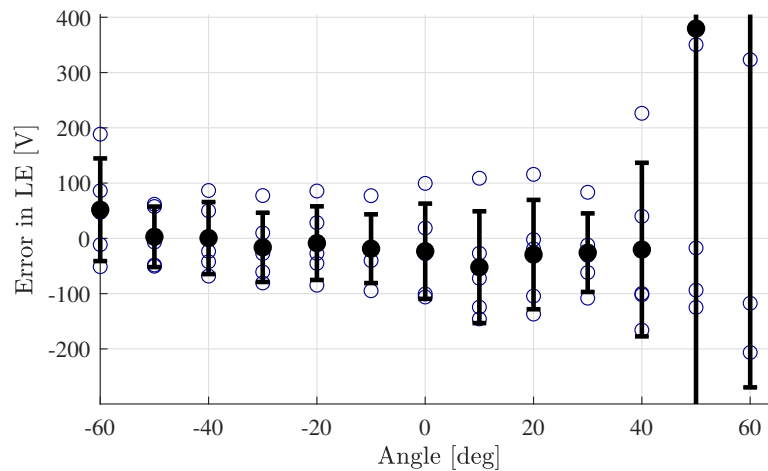


Figure 3.26: Errors in landing energy estimation for rotating titanium target plate. The  $0^\circ$  reference is perpendicular to the incident beam; interference with the chamber wall occurs at  $> 40^\circ$ .

In a flight scenario with minimal separation between the detector and beam, these results show that an equivalently usable signal is available for  $> 75\%$  of the rotation of a flat plate, with near-continuous availability for 3D structures.

### 3.3 Conclusions

Developing an experimental test facility capable of investigating the electrostatic potential sensing method, and a range of space charging tests more broadly, has been a significant multi-year undertaking by a team of researchers. However, this has resulted in a facility uniquely suited to the needs of this work.

Two test campaigns discussed here evaluated the performance of the electrostatic potential sensing method under a range of geometries. No angular dependence was found in the range of sensor locations tested, which enables an accurate potential estimate to be found when the sensor is located near the electron beam. Likewise, no relationship was found between the target plate orientation and landing energy error, indicating that any region with signal availability, over  $> 75\%$  of a target body's rotation, will provide an equally accurate potential estimate. This accuracy for the given detector configuration is found to have a mean value of just  $10 \pm 57\text{V}$ ,  $1\sigma$  for landing energies below 7 keV. However, increasing landing energy increases the normalized error in landing energy estimation, so the landing energy should be limited based on the detector to ensure best performance.

## Chapter 4

### Remote electrostatic potential sensing in the high earth orbit x-ray environment

Previous chapters demonstrate the theoretical and experimental viability of the remote potential sensing concept. However, these analyses apply only for the case of an electron beam in a pure vacuum and neglect environmental interactions introduced by ambient plasmas and other x-ray sources. This chapter extends the prior analysis to look at the impact of GEO electron fluxes, which can generate additional bremsstrahlung radiation on a target or in an x-ray detector, and other x-ray contributions. Additionally, a method for estimating the potential of an object using only x-rays generated by the ambient plasma is discussed and experimentally evaluated.

#### 4.1 Prior observations of environmentally induced x-rays

Bremsstrahlung is frequently observed in orbital x-ray detectors due to energetic electrons in the plasma environment. These observations generally come from one of three sources: energetic particles interacting with atmospheres or surfaces of airless bodies, bremsstrahlung occurring on the spacecraft in view of the sensor, or occurring within the sensor itself.

Reference [73] presents a general overview of observations of bremsstrahlung generated by energetic electrons precipitating into the atmosphere, while Reference [169] examines these bremsstrahlung spectra to determine the energy distribution of the source electron population. Bremsstrahlung from energetic plasma electrons has also been observed on the lunar surface [79].

Gamma ray burst observatories, the BATSE instrument on the Compton Gamma Ray

Observatory, detected many examples of x-ray bursts which were ultimately traced to electron bremsstrahlung on the spacecraft surfaces or in the instrument [70]. Instrument design, such as that for the Nancy Grace Roman IR telescope, requires an evaluation of electron-induced bremsstrahlung when assessing instrument performance in regions with populations of energetic electrons [154, 88].

## 4.2 Ambient plasma-induced x-rays

Bremsstrahlung radiation in the x-ray spectrum is generated by electrons with energies above  $\sim 1$  keV, with no upper limit. However, energy dispersive detectors work only in finite energy regions. For the Si-PIN diode in the Amptek X123 spectrometer, the detection efficiency begins to fall off above 12 keV, and limits the overall detection energy to approximately 1-30 keV [3].

Bremsstrahlung radiation is generated as a continuum up to the energy of the incident electron, so even a 1 MeV electron would be expected to have some photon contribution in the 1-30 keV range. However, the flux of electrons with a given energy decreases rapidly as energies increase, so the contributions electrons  $> 100$  keV are neglected. Geospace plasma, particularly in the geostationary orbit region, is dominated by electrons and protons capable of generating bremsstrahlung radiation. However, the much higher mass of protons means they require orders of magnitude more kinetic energy than electrons to achieve significant bremsstrahlung yields, resulting in a negligible contribution to the x-ray spectrum. Additionally, the electron flux at GEO is assumed to be isotropic [43, 88]. Even though bremsstrahlung has strong directional components depending on the angle of the incident electron, prior work on plasma-generated bremsstrahlung indicates the resultant thick target spectrum is assumed to be isotropic [103].

The bremsstrahlung yield, defined by the number of photons emitted per incident electron, is dependent on the energy of the incident electron and the atomic number of the target material. Increasing electron energies and increasing atomic number both result in higher yields, as discussed in Chapter 2. Spacecraft generally make extensive use of aluminum alloys in their construction, and aluminized coatings are a major component of the multi-layer insulation typically used to insulate spacecraft, so an aluminum coated spacecraft is assumed for this work. In practice, a spacecraft

would contain surfaces coated in thermal control paint such as AZ-93, and solar arrays covered in glass should be coated with a conductive film such as indium tin oxide [170]. While the elemental composition of AZ-93 is not available in the literature, it is known to use a silicate-based binder [151]. Silicon has atomic number 14, while aluminum is 13, so the silicate binder will have similar bremsstrahlung and characteristic radiation efficiencies to aluminum. The specification provides for application of AZ-93 to a depth of 5 mils, or 0.127 mm [151].

According to the NIST ESTAR database of electron stopping powers in various materials, a 20 keV electron will be stopped in 7.5  $\mu\text{m}$  of aluminum [23]. Assuming an incident electron flux that is isotropically distributed across  $2\pi$  steradians, the mean stopping distance should fall within 4.5  $\mu\text{m}$  of the material surface. The random walk nature of successive electron-atom interactions also serves to reduce this distance, such that electrons will deposit their energy very close to the surface. Therefore, the assumption that only coatings and surface materials will interact with incident electrons is valid for this approximation.

Section 2.2.2 describes methods for simulating the x-rays generated through bremsstrahlung and characteristic radiation, and those techniques are applied here. However, computation of the resultant x-ray flux requires an electron flux model as an input. A year-averaged GEO flux was obtained from SPENVIS, using the IGE-2006 model for trapped electron fluxes [145]. This model provides 3 flux outputs: a mean, and a lower and upper bound, as seen in Figure 4.1. The electron energies are sorted into logarithmically spaced bins, and the 16 bins from 0.92 keV to 130 keV are used here. Though the model includes electron fluxes for energies up to 5 MeV, the diminishing numbers of electrons at increasing energies means the contribution of those electrons to the 0-30 keV x-ray spectrum is limited.

From this set of electron energy distributions, combined with Equations 2.2 and 2.3, the emitted x-ray spectrum can now be approximated. This is done iteratively, with the assumption of all electrons in a given bin having the mean energy of that bin (i.e., all electrons in the 0.92-1.2 keV bin are assumed to have an energy of 1.06 keV). Figure 4.2 illustrates the x-ray spectrum contributions of each energy bin, and the total x-ray flux that would be generated for the IGE-2006

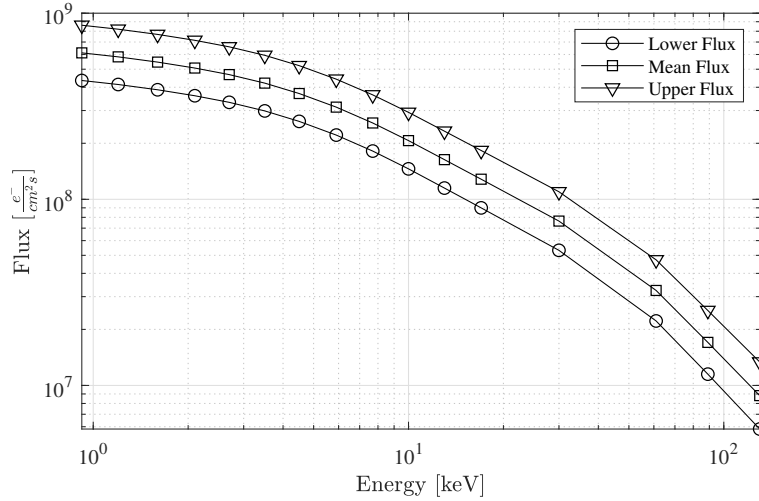


Figure 4.1: The electron flux at GEO for IGE-2006 model lower, mean and upper fluxes. Points from the model are illustrated by the markers, the lines are for illustrative purposes only.

mean electron flux case. The lower electron flux case from the IGE-2006 model resulted in a 31% reduction x-ray photon generation relative to the mean case. The upper electron flux case resulted in a 46% increase in photon emission relative to the mean.

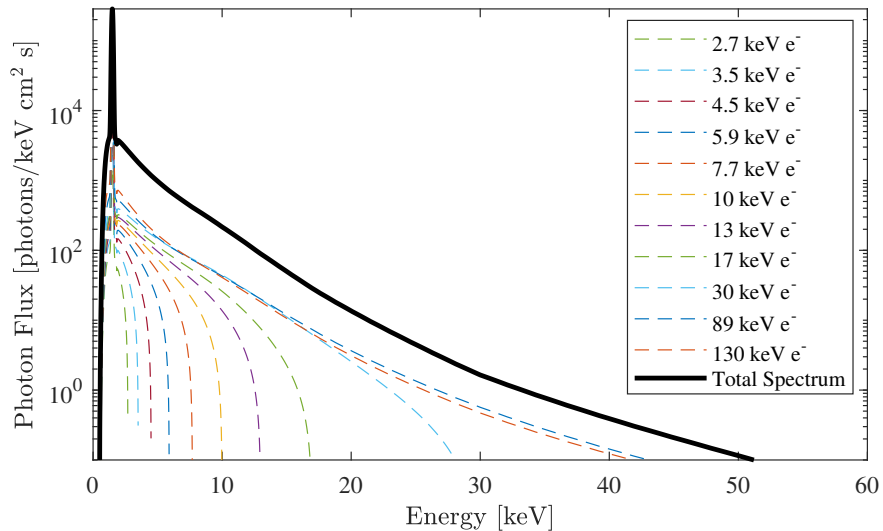


Figure 4.2: X-ray spectrum due to mean electron flux conditions at GEO.

## 4.3 Passive sensing of electrostatic potentials

### 4.3.1 Theory

The ultimate goal of this work is to determine the electrostatic potential on a co-orbiting object touchlessly. The x-ray spectrum from ambient electrons impacting a surface provides an intriguing option for doing so without requiring an active electron beam to excite x-ray emission.

As a spacecraft charges, it will effectively shift the energy of incident electrons by either accelerating them if it accumulates a positive charge, or repelling them at negative potentials. A spacecraft charged to -10kV, for example, will repel any incident electrons with less than 10 kV. Therefore, the electron spectrum will be shifted by 10 kV, as seen in Figure 4.3, which in turn results in reduced photon fluxes. The anticipated drop in photon fluxes can be computed for any spacecraft potential, assuming a steady electron environment, which leads to the spacecraft potential versus x-ray flux curve shown in Figure 4.4. This effect generalizes to positive target spacecraft potentials.

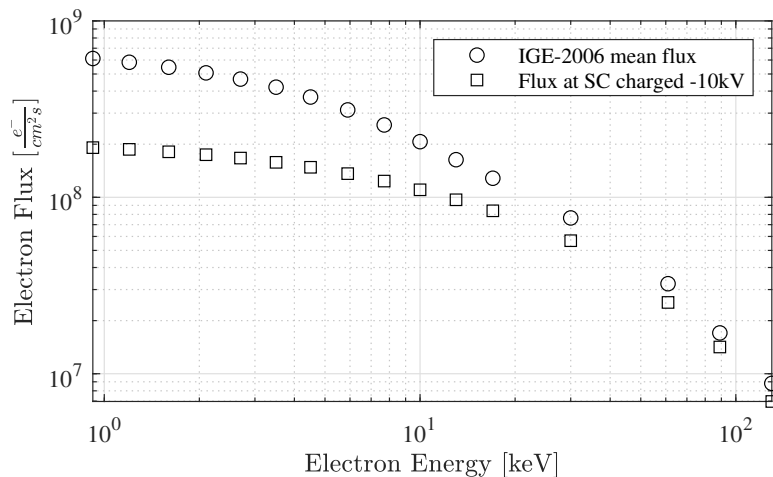


Figure 4.3: Electron flux from the IGE-2006 mean flux and that observed by a spacecraft charged to -10 kV.

The change in emitted x-ray quantities provides a means of determining the charge state of an object without requiring spectrum-based analysis. If the servicing craft can measure the local electron population, then the potential of the target is inferred by examining the change in x-ray

emission. For a case with consistent local plasma properties, a decrease in x-ray emission would indicate negative charging, while positive spacecraft potentials would be marked by increases in x-ray emission. Therefore, this method is useful in indicating changing surface potentials in cases where the plasma remains relatively constant. Such circumstances are found naturally when a spacecraft crosses from sunlight to eclipse conditions, or in a rendezvous scenario, when the servicer eclipses the sunlight on the target. Additionally, a small x-ray detector could instead be used as a proxy for an electron spectrum monitoring instrument; a significant change in x-ray flux could be used as an indicator of changing environmental conditions, which increases charging risks.

An example of such a scenario occurs during rendezvous of the Orion crew module with NASA's planned Lunar Gateway, when the Orion capsule will be shadowed by Gateway during the terminal rendezvous phase. Reference [56] shows that the change in photoelectric current could result in potential differences of several kV between the two bodies, posing electrostatic discharge risks at contact. The ability to measure the relative potentials between the objects, or the change in potential of the Orion module as it moves into eclipse, could help indicate the presence of hazardous potential differences. Time-varying plasma conditions require recomputation of the expected x-ray flux from the target, however this is feasible if the local plasma conditions are monitored.

It is worth noting that the indication of charging found here, that the x-ray flux decreases as a spacecraft potential increases, runs somewhat counter to the conclusions of Reference [50] in their analysis of using x-ray fluxes as proxy indicators of charging events. However, these two analyses apply to fundamentally different scenarios: here it is assumed that the plasma conditions are near steady state, while the work of Reference [50] assumed the spacecraft were charging due to severe geomagnetic storm events. The authors therefore examined high energy bremsstrahlung emitted by the high energy electrons (40 to 180 keV) associated with geomagnetic storm conditions, but neglected the contributions of more numerous lower energy electrons that dominate low energy x-ray emission even in quiet conditions. Additionally, Reference [50] focuses on high energy x-rays, while this work is concerned with x-ray energies approximately an order of magnitude lower.

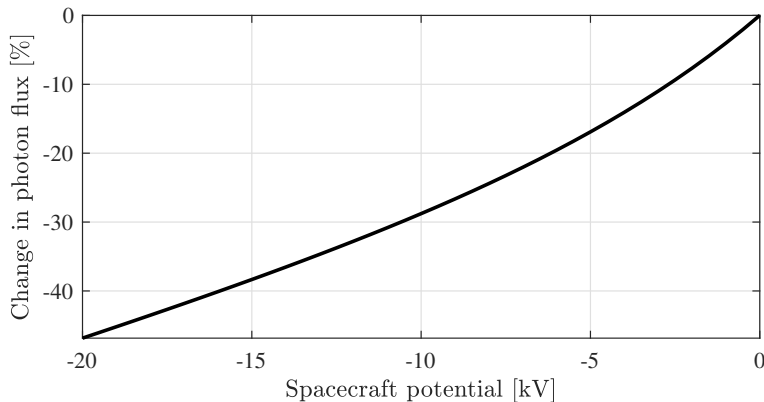


Figure 4.4: Change in total x-ray photon emission due to plasma electron bremsstrahlung as a function of spacecraft potential.

### 4.3.2 Experimental validation of passive sensing

A series of experiments have been carried out to validate this passive sensing method. All experiments have been conducted in the ECLIPS facility discussed in Chapter 3. The experimental setup includes four main components: a broad-spectrum electron gun aimed at a target plate, a custom-built retarding potential analyzer (RPA) to measure the electron flux, and an x-ray detector to observe the resulting x-ray spectra (Figure 4.5). The 6061 aluminum target plate includes a 5 mm hole to allow the RPA, which is situated directly behind the plate, to measure the electron spectrum.

In contrast to monoenergetic electron beams, the broad-spectrum electron gun described in Section 3.1.1 emits electrons at a wide range of energies, enabling the experimental simulation of the electron populations in the space environment [13]. The maximum energy of the emitted spectrum corresponds to the voltage provided by a power supply, a Matsusada AU series high-voltage power supply. The RPA is described in detail in Reference [167] and consists of a grounded front grid, a discriminating grid with variable voltage, and a collection cup connected to a picoammeter. An Amptek X123 x-ray spectrometer with a 6 mm<sup>2</sup> Si-PIN diode sensor is used to detect the generated x-rays. The plate potential is controlled by a Spellman SL300 high-voltage power supply, and chamber pressure is kept below  $1 \times 10^{-6}$  Torr for all experiments. The maximum energy of the

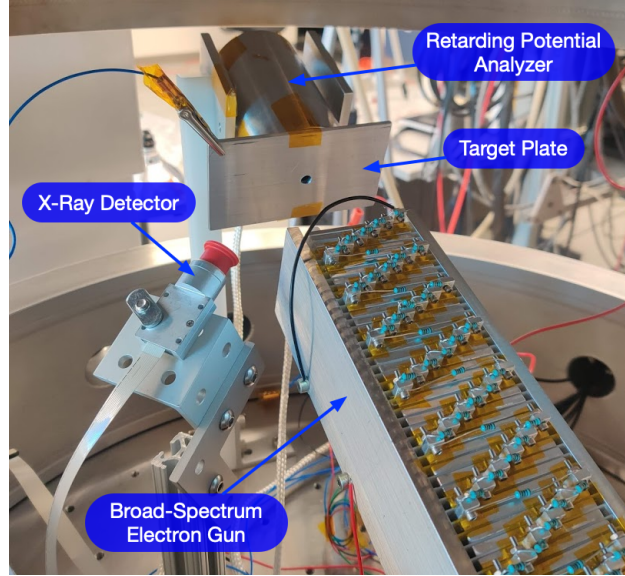


Figure 4.5: Experimental setup in chamber

spectrum created by the broad-spectrum electron gun is set to 3.3 kV, and the observed integral electron flux for a plate potential of 0V is shown in Figure 4.6.

The experiment procedure is as follows: Prior to starting the electron gun, the target plate potential is set to the desired voltage. Once the electron gun is started and emits electrons onto the plate, the resulting x-ray spectra are measured by the x-ray detector, which records for 20 seconds such that a sufficient number of photons is detected. The RPA measures the electron flux only if the plate potential is equal to 0 V. This procedure is repeated five times for each target plate potential.

The total number of photons  $I_{\text{ph}}$  observed is determined for each plate potential by adding up the detected photons in every energy bin of the experimental spectrum. To obtain the change in total x-ray emission, the number of detected photons is compared to the total number of photons for a 0V plate potential,  $I_{\text{ph},0}$ :

$$\Delta I_{\text{ph}} = \frac{I_{\text{ph}} - I_{\text{ph},0}}{I_{\text{ph},0}} \quad (4.1)$$

The theoretical change in total x-ray emission is obtained with Equations 2.2 and 2.3, using the mean electron spectrum of the 0V potential tests. As described above, the electron flux is

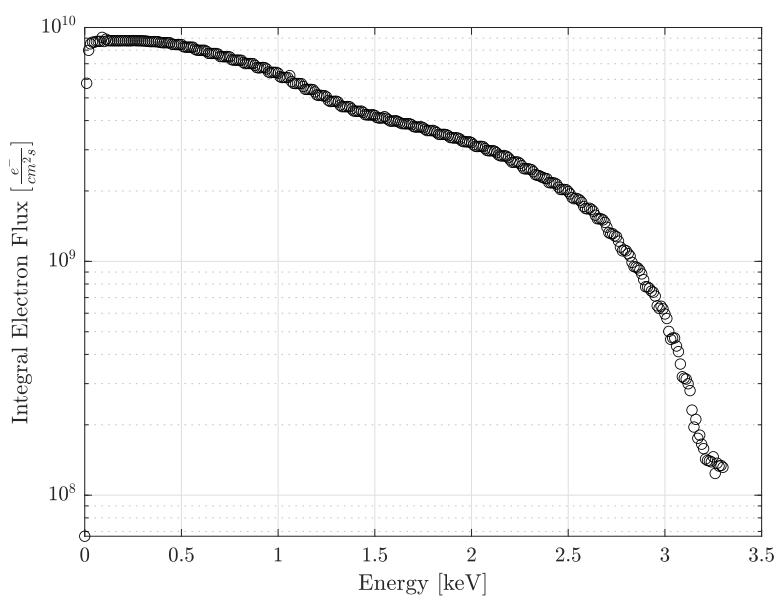


Figure 4.6: Integral electron flux of the broad-spectrum electron gun up to 3.3 keV, measured by the retarding potential analyzer.

shifted for plate potentials other than 0 V to accommodate for the changing electron populations that result from a charged plate. Figure 4.7 shows the experimental and theoretical change in total x-ray emission for plate potentials between -500 V and 400 V. The circles indicate the mean value, and the bars correspond to the  $2\sigma$  interval of the five test runs for each plate potential. Figure 4.8 includes a histogram for the error of the estimated plate potential, that is, the difference between the estimated potential according to the theoretical change in x-ray photons and the actual plate potential during the experiment. The errors are reasonably small, with a mean error of  $23 \pm 29\text{V}$   $1\sigma$ , and the experimental results follow the same trend as the theoretical curve. However, there is a non-zero bias in the errors shown in Figure 4.8, and the theoretical curve seen in Figure 4.7 appears to over predict the change in photon flux in due to both positive and negative potentials. This is due to the angular distribution of bremsstrahlung radiation, which favors emission in certain directions dependent on the energy of the incident electron. The models used in Section 2.2.2 to estimate bremsstrahlung radiation are based on an angle-integrated formulation, which does not account for these directional effects.

The experiments with a monoenergetic beam in Chapter 3 found no statistically significant dependence between detector-beam separation angle and landing energy computation accuracy. However, the angles evaluated there were limited to  $\pm 30^\circ$  from beam normal by the x-ray detector ribbon cable constraints. In this case the detector is positioned closer to  $60^\circ$  from beam normal, and beam normal is less defined due to the wide range of electron trajectories emerging from the broad spectrum electron gun. Both of these effects can lead to directional anisotropy in the resultant spectrum.

The limited accuracy of the utilized analytical expression of the bremsstrahlung model motivates alternative means of improving the passive electrostatic potential estimation method.

One way to mitigate the effects of the directional dependency of bremsstrahlung emission and the limitation of the analytical approximations is to look at only part of the x-ray spectrum, specifically the characteristic radiation. Unlike bremsstrahlung radiation, characteristic radiation is emitted isotropically, avoiding angular anisotropy concerns. The theoretical change in x-ray

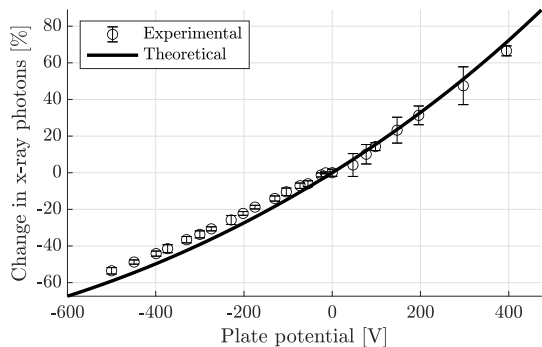


Figure 4.7: Change in total x-ray photon emission due to ambient plasma as a function of plate potential.

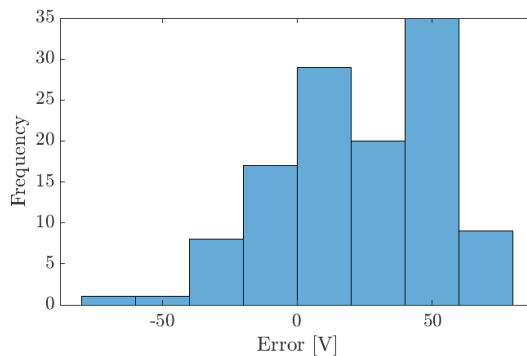


Figure 4.8: Error of the estimated plate potential for the set of points shown in the left plot.

photons is found by using Equation 2.2 to compute the expected number of emitted characteristic for a given incident electron flux. As discussed previously, characteristic radiation is emitted at a specific energy, but due to in-detector spreading effects, a Gaussian peak in the x-ray spectrum can be observed.

To filter out the bremsstrahlung radiation from the experimental spectrum, a Gaussian function is fitted to the characteristic peak. The energy level where the experimental spectrum starts to deviate significantly from the Gaussian function gives information about both the width of the characteristic peak and the intensity of the bremsstrahlung radiation at that energy. The resulting number of photons corresponds approximately to the photons emitted as characteristic x-rays. Equation 4.1 is used for the computation of the theoretical and experimental change in characteristic x-ray photon emission, and the results are shown in Figure 4.9.

The theoretical curve aligns closely with the experimental values, with the error bars encompassing the true value in every case shown in Figure 4.9. Comparing the results of the characteristic photon emission to the results of total photon emission (including the bremsstrahlung radiation) suggests that using the characteristic yield alone provides a better way to passively estimate the electrostatic potential of the plate. Figure 4.10 shows the errors of the estimated plate potential, which are in a similar range as the errors of the landing energy estimation that utilizes an active mono-energetic electron beam [162]. The strong agreement between the theory and the experi-

mental results—just  $7 \pm 20\text{V}$   $1\sigma$  mean error—indicate that this passive sensing method provides a promising approach of touchlessly estimating the electrostatic potential of a nearby object without using an electron beam.

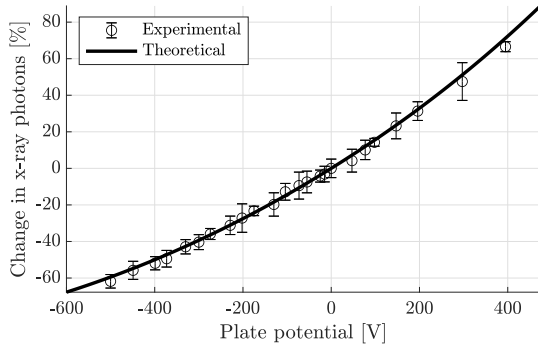


Figure 4.9: Change in characteristic x-ray photon emission due to ambient plasma as a function of plate potential.

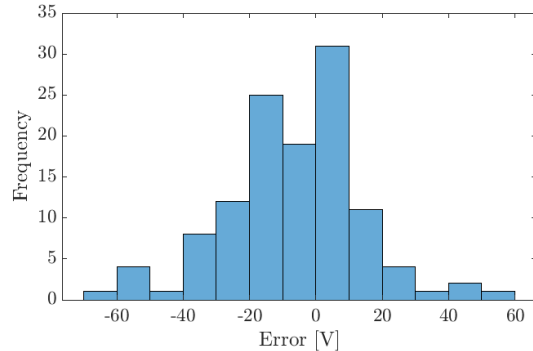


Figure 4.10: Error of the estimated plate potential for the set of points shown in the left plot.

#### 4.4 Solar x-ray contribution

The sun is a significant source of x-rays which may interfere with efforts to use x-ray spectra to measure estimate electron landing energies. A number of missions have flown x-ray spectrometers in Earth orbit to observe the sun, and these spectra could be used to determine the contribution of the solar x-ray spectrum to a spectrum that would be sensed in a potential measurement scenario. Two missions, the MinXSS-1 and MinXSS-2 cubesat solar observatories, flew variants of the x-ray detector used in the experimental part of this work [104]. MinXSS-1 operated in 2016, and two sample spectra from this mission, preprocessed to Level 1 and obtained from [2], are shown in Figure 4.11.

It is assumed that the sensor is oriented such that the sun line of sight is excluded from the sensor’s field of view, but the sun is illuminating the object of interest. X-rays incident on a surface typically do not undergo reflections, but can excite the release of characteristic x-rays from the surface material through secondary fluorescence [159]. Any incident x-ray with an energy above the characteristic energy of the atom it is interacting with can result in secondary fluorescence, a

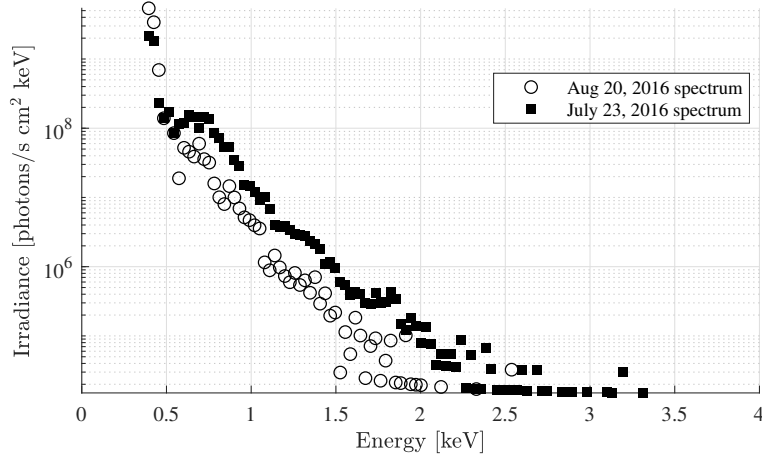


Figure 4.11: The solar x-ray spectrum observed by MinXSS-1. July 23 was the date of 2016’s most significant flare event, an M7.6, and illustrates enhanced x-ray flux relative to the quiet August 20th spectrum [2].

technique which is often used for material composition mapping of airless bodies like the Moon and asteroids [99]. An equation for fluorescence yield was developed by Reference [159], and represents the number of characteristic photon emissions per incident photon with an energy greater than the characteristic energy  $E_k$ :

$$\omega_K = \frac{10^{-6} Z^4}{1 + 10^{-6} Z^4} \quad (4.2)$$

For aluminum, this yields an efficiency of approximately 0.03, which matches well with the experimental data compiled by [78].

Therefore, for each photon with an energy over 1.49 keV incident on aluminum approximately 0.03 characteristic x-rays are generated. For a spacecraft made of aluminum with an area of 5 m<sup>2</sup>, integrating the MinXSS-1 data for the nominal August 20th spectrum and then multiplying by  $\omega_k$ , this yields  $2.5 \times 10^7$  photons emitted per second with an energy of 1.49 keV. The same analysis performed on the July 23, 2016 flare data yields an x-ray flux nearly 6 times larger, at  $1.4 \times 10^8$  photons per second.

Ultimately, the solar x-ray contribution to the sensed x-ray spectrum from the target will be negligible, only increasing the flux of characteristic x-rays. Incident photons with energies above the characteristic energy of the surface elements will be absorbed by the material but can contribute

to characteristic emission, while those with energies below  $E_k$  will primarily be absorbed without inducing secondary fluorescence. For the nominal solar spectrum, it is expected that only a few tens of additional photons will be observed per second by a  $75 \text{ mm}^2$  detector at a distance of 10 meters.

While the servicing spacecraft can be oriented to avoid having solar photons directly incident on the sensor aperture, the cosmic x-ray background is much harder to exclude. However, the flux levels are much lower than those from the sun, with estimates on the order of  $10 \text{ photons cm}^{-2} \text{ s}^{-1} \text{ sr}^{-1} \text{ keV}^{-1}$  in the keV range. For a  $75 \text{ mm}^2$  detector with a  $10^\circ$  field of view, this yields a negligible flux of around 1 photon per minute.

#### 4.5 Spectrum with environmental noise contributions

Ultimately, the bremsstrahlung-based method for determining the potential of a target is better suited to use in active charge control scenarios, such as the Electrostatic Tractor [135]. A nominal electron beam current for such a scenario may be on the order of  $10 \text{ }\mu\text{A}$ . Figure 4.12 illustrates the relative magnitudes of the bremsstrahlung radiation from the electron beam and the ambient plasma, assumed to be the IGE-2006 mean flux. For direct comparison, both spectra are treated as isotropic point sources 10 meters from a detector with a  $75 \text{ mm}^2$  sensor. In reality, the electron beam contribution is likely to behave in a point-source like manner, but the x-ray emission from it is not isotropic. The plasma-induced x-rays will be isotropic [103], but are less accurately modeled by the point source approximation. However, accurately modeling this distribution requires knowledge of the target geometry and relative attitude, which is highly scenario dependent. As shown, the solar x-ray spectrum adds only to the characteristic radiation, and has no contribution to the bremsstrahlung continuum. The hot plasma electron flux does contribute to the bremsstrahlung spectrum, but at a level that is approximately 4 orders of magnitude smaller than the beam-induced flux. The electron beam current in this scenario is  $10 \text{ }\mu\text{A}$ , while the cumulative plasma current (neglecting charging effects) is approximately  $0.7 \text{ nA}$ —roughly 3.5 orders of magnitude smaller, in line with the relative x-ray fluxes.

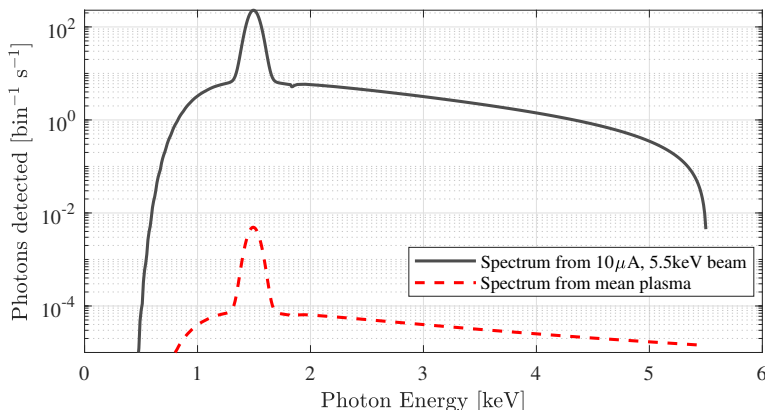


Figure 4.12: Simulation of sensed x-ray spectrum for a  $10 \mu\text{A}$  electron beam and ambient plasma electron fluxes, using the IGE-2006 mean flux. The target is assumed to be an isotropically emitting point source equivalent to a  $5 \text{ m}^2$  aluminum spacecraft.

The local plasma is therefore dominated by the electron beam-induced x-rays and forms an insignificant contribution to the sensed spectrum. The presence of ambient hot electron populations will not significantly impact the ability to determine the landing energy of the electrons. Likewise, the solar x-ray contribution to the characteristic radiation will not impact the determination of electron beam landing energy.

## 4.6 Radiation effects within detector

Just as environmental interactions will generate x-rays on a target surface, the space environment will also interact with the x-ray sensor itself. Energetic electrons and protons from the ambient plasma could be significant sources of noise within a silicon diode detector, and galactic cosmic rays can also contribute spurious signals. Though more energetic sources could generate x-ray signals by interacting with any part of the servicing spacecraft structure, the analysis here will focus on interactions with the detector itself.

### 4.6.1 Electron trajectories in detector

An open source Python package built on the GEANT4 electron-photon transport monte carlo codes, pyPenelope [48], was used to simulate an incident shower of electrons on a simplified

detector geometry. A 2D representation of the detector is developed, as a 25  $\mu\text{m}$  thick beryllium layer, followed by 0.1 mm (100  $\mu\text{m}$ ) of vacuum, and then a 500  $\mu\text{m}$  thick silicon layer atop a 500  $\mu\text{m}$  layer of copper, representing the thermoelectric cooler and support electronics. Figure 4.13 shows the electron tracks propagating through the simplified assembly. This figure qualitatively shows the general distribution of 250 keV electrons through the detector, with the beryllium window serving to scatter incident electrons, which then deposit the remainder of their energy in a wider area of the silicon diode. Some of the electrons are seen to backscatter from the silicon diode back into the beryllium window. Each interaction in both the silicon and the beryllium can result in the formation of bremsstrahlung x-rays, or characteristic x-rays as a result of inner-shell vacancy formation. Therefore, a fraction of the initial energy of each electron will be deposited in the silicon diode as photons or electron-hole pairs. The standard for determining this energy deposition would be to develop a mass model of the full spacecraft and sensor structure, and then perform a high fidelity Monte Carlo simulation approximating the incident particle and photon radiation spectra [41, 59]. However, this process is expensive both computationally and in the human time required to develop the model.

Instead, an approach is pursued here that allows for a first order approximation of the effects of particle radiation within the detector. These results are then compared to high fidelity analyses and flight data found in relevant instrument literature. The environmental electron (IGE-2006 model), proton (AP-9 model) and GCR (ISO-15390 model) fluxes are obtained from Spenvis [145]. Particle radiation is assumed to impinge from the beryllium layer, using the same simplified geometry as Figure 4.13. This assumption may not be accurate for highly energetic particles which could penetrate through the spacecraft structure, but provides a starting point for this analysis without knowing the full shielding characteristics of the entire spacecraft.

#### 4.6.2 Energy deposition analysis

The NIST ESTAR and PSTAR databases, which cover electron and proton radiation, respectively, were used to obtain range, photon radiation yield and stopping power data for beryllium,

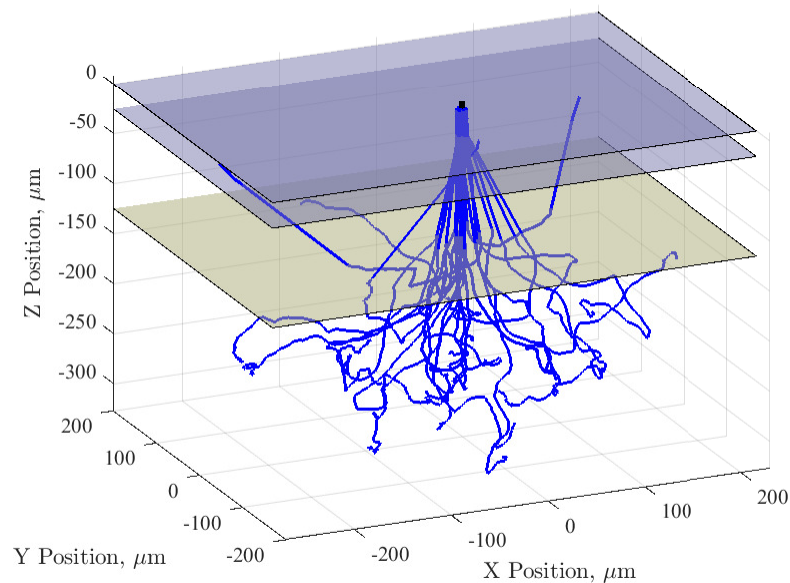


Figure 4.13: Twenty electrons (250 keV initial energy) incident on a simulated detector structure. The top two layers represent the top and bottom faces of the  $25\ \mu\text{m}$  beryllium window, while the bottom layer represents the top face of the silicon diode.  $100\ \mu\text{m}$  of vacuum separate the materials.

silicon and copper. Using the continuous slowing down approximation (CSDA), the average range of electrons and protons is computed to determine which energies and fluxes are expected to reach the detector diode, and which are expected to fully penetrate the diode. These curves are shown in Figure 4.14. Effectively all proton fluxes are blocked by the detector window, while approximately  $10^3$  electrons/cm<sup>2</sup>-s are expected to reach the diode. However, for this energy range the bremsstrahlung generation rate for electrons is approximately  $10^{-3}$ , suggesting around one in-detector bremsstrahlung event per second, though additional interactions may result in spurious in-detector signals on the order of 10 counts per second.

Heavy particles, such as protons, tend to have relatively direct trajectories through materials. However, electrons are highly scattered in interactions, so a statistically-derived projected range is used to estimate the distance they penetrate into material. A worst-case normal incidence assumption is applied to both electrons and protons interacting with the detector.

Like electrons, protons impacting a material result in a range of interactions, some of which

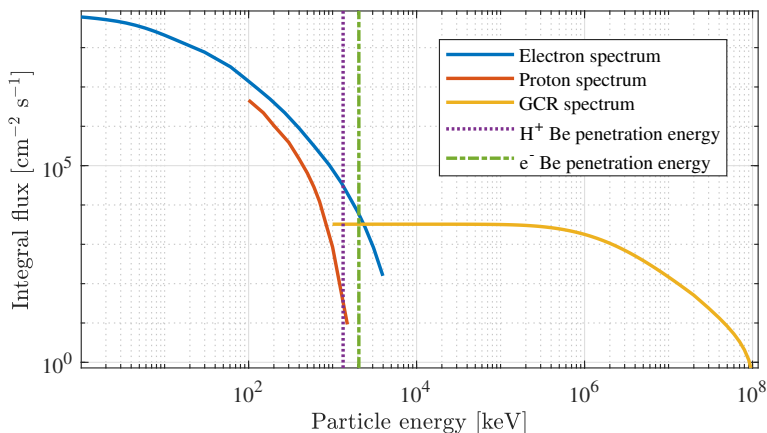


Figure 4.14: Electron, proton and GCR spectra and the relative energies required to penetrate the beryllium detector window.

yield x-ray photons. The most significant yield for proton-induced x-rays (PIXE) are from characteristic radiation, which are generated in significant quantities for protons with MeV-levels of energy [75]. Much like electron-based methods, a continuous x-ray background is generated by charged particle interactions, though this is a minor photon flux compared to the characteristic yield, and therefore is neglected here.

Beryllium has a  $K_{\alpha}$  characteristic energy of just 108 eV, which makes it quite susceptible to PIXE. However, the such low energy photons have relatively short attenuation lengths, and are likely to be absorbed in the beryllium window and in the silicon “dead layer” that forms on the surface of diodes. For the X-123 detector, this dead layer has a thickness of approximately 150 nm [57]. Photons with an energy of 108 eV, however, have an attenuation length (the point where photon flux has fallen to  $1/e$  of the initial value) of just 53 nm [65]. As the dead layer is 3 times the attenuation length, less than 5% of the photons that emerge from the beryllium window will reach the active area of the diode, providing significant shielding from this photon source. Additionally, beryllium has a very low rate of secondary fluorescence—equation (4.1) gives approximately 2 photons emitted per ten thousand incident—limiting the impact of this noise source on the detector.

In total, these results suggest that between 10 and 100 spurious counts per second can be

expected for an unshielded detector operating at GEO. These events will be quasi-static, forming a level of background noise that should be filtered and accounted for in practice. Additionally, these count rates are 1-2 orders of magnitude lower than the flux that would be observed for an operating electron beam, as seen in Figure 4.12. It is worth reiterating that these results are for an unshielded detector. Even 2.5 mm of aluminum shielding can reduce proton fluxes by over two orders of magnitude for  $<10$  MeV. Additionally, an open ended cylinder of shielding material (likely a layered structure with high  $Z$  material on the exterior and a low  $Z$  material on the inside) could be used to reduce particle fluxes on the detector by effectively decreasing the field of view. Assuming isotropic particle fluxes, adding a 5 cm long shielding tube could decrease the field of view and the associated particle fluxes by a factor of 50. Likewise, having the beryllium window located at the front of the shielding tube will significantly ( $\sim 1/200$ ) reduce the number of x-rays generated in the window that can reach the detector, due to their near-isotropic distribution. While a first-order assessment, these results indicate that in-detector noise is unlikely to be a significant problem for most operations in the GEO environment [121]. Analyses and flight results for a series of missions with related detector technology is used to validate this conclusion.

### 4.6.3 Comparison to analysis in other missions

Noise generated by the space environment has long been a significant consideration in instrument and mission design. As a point of comparison to the estimates of environmental noise obtained here, instrument background estimates and models from the literature were considered for a few high energy photon instruments.

The analysis presented in reference [92] examines the background spectra for both high earth and low earth orbits. SIGMA, a soft gamma ray telescope (35-1300 keV) that operated in a highly elliptic high earth orbit which included transiting the outer radiation belts. Significant contributions were noted from trapped proton radiation, which interacted with the spacecraft to produce radioisotopes that continued to decay in otherwise quiet portions of the orbit. Solar energetic protons (SEP) are found to have a significant contribution to the detector noise during

flare events, but insignificant during quiescent periods. The overall measured background level, including all sources, was measured to be  $1.4 \times 10^{-3}$  counts-cm<sup>-2</sup>-s<sup>-1</sup>-keV<sup>-1</sup> [92].

The European Space Agency’s XMM-Newton mission, also in a high earth elliptical orbit (ranging from 7000 km at perigee to 120000 km at apogee) experienced higher than expected instrument background noise levels, which Reference [59] compares to background simulations and results for the Suzaku and Swift x-ray observatories in LEO. The CCD sensor used by XMM-Newton was sensitive in the 0.2-10 keV energy range, comparable to the sensors under consideration for use here, with a 280  $\mu$ m silicon layer thickness. Data provided by Reference [59] indicates a background continuum flux of approximately  $3 \times 10^{-3}$  counts-cm<sup>-2</sup>-s<sup>-1</sup>-keV<sup>-1</sup> for the XMM-Newton mission and comparable levels for the sensors aboard Suzaku and Swift. These values are within an order of magnitude of the values measured by SIGMA. The ATHENA mission, a future x-ray telescope planned to operate at L2, is expected to observe the 0.1 to 15 keV energy range. Simulations of the anticipated spacecraft structure likewise indicate background noise rates on the order of  $10^{-3}$  counts-cm<sup>-2</sup>-s<sup>-1</sup>-keV<sup>-1</sup>m [63].

Further analysis by Reference [59] indicates that, for high earth orbits, secondary “knock-on” electrons generated by high energy protons within the spacecraft structure become a dominant component of instrument noise. However, these instruments are relatively centrally located within a larger spacecraft structure, and as such it is mostly shielded from protons with energies below 70MeV. For the scenario under consideration for potential estimation, a small sensor is likely to be placed on the exterior of the spacecraft, and therefore low-energy contributions are more likely to dominate. The anticipated environment-induced background in an additional instrument is worth considering, was analyzed for a geosynchronous orbit and specifically considers the trapped proton environment found there. The Roman Space Telescope is intended to observe infrared wavelengths, but the analysis is performed for generic silicon based detectors [88]. As in other cases, the authors find background photon and hadron environments to be a significant consideration requiring design effort, but not a major obstacle for highly sensitive instrument operation.

Ultimately the result of the analysis here and experience with other missions suggest that

environmentally induced noise in instrument sensors is a tractable problem, and is addressable through physical shielding and signal processing measures.

#### 4.7 Debris sensing SSA applications

The primary means of tracking objects in space currently are terrestrial optical or radar facilities. Both of these methods typically have limited resolution and sensitivity at GEO, and must be implemented terrestrially due to challenges in spacecraft integration [54]. The mechanisms discussed here which lead to x-ray emission from a body apply to any solid in space. Therefore any object, including difficult-to-track debris objects, will emit x-rays when exposed to solar x-rays or energetic electron populations. These x-ray emissions have applications for space situational awareness (SSA), providing a means of detecting co-orbiting debris objects passively. This is particularly useful in a GEO context, where many large objects orbit with low relative velocities but in close proximity. Ground-based observations of spacecraft in GEO are limited to tracking objects greater than  $\sim 1$  meter in size, and have limited positional resolutions, which limits their ability to warn of conjunction events [139]. Therefore, it is advantageous to passively sense other debris objects passing in a spacecraft's vicinity to improve the debris catalogue and inform avoidance maneuvers to mitigate collision risks.

Combining the results of the IGE-2006 mean electron spectrum and the mean solar induced fluorescence, approximately  $3 \times 10^{10}$  x-ray photons will be emitted per second from a  $5 \text{ m}^2$  aluminum debris object, such as a defunct spacecraft. In practice elements heavier than aluminum, such as indium-tin compounds used to coat solar panels, or nickel alloys used in rocket motor nozzles, will have reduced characteristic radiation yields (due to the increase in characteristic energy) but increased bremsstrahlung yields. However, the aluminum approximation illustrates the feasibility of detecting these emissions from a co-orbiting spacecraft.

A few assumptions about the sensor and detection thresholds are made. First, the sensor is assumed to require detection of 10 photons over a 20 second integration period to provide a reasonable reliability. As earlier, the photons are assumed to be emitted from the object are

isotropically, and a sensor like the Amptek SDD with a mean efficiency in the energy region of interest of 90% and a detector area of  $75 \text{ mm}^2$  is used. For this case, a separation of some 780 meters or less yields the signal required to identify the presence of a nearby object; this rises to nearly 1 km for the IGE-2006 upper electron flux case. The detector sensitivity could be increased by the use of x-ray optics, like those that were developed for the NICER x-ray observatory mission which have an effective collection area of  $44 \text{ cm}^2$  at 1.5 keV [115]. Adding these optics extends the detection range to nearly 6 km (over 7.2 km in the upper electron flux case). Other options, from larger or more efficient optics, or increased integration times, could improve the sensitivity of this method.

## 4.8 Conclusions

Although environmental contributions to the sensed x-ray spectra do not impact relative potential sensing method, they are able to provide an alternative, passive form of electrostatic potential estimation. The introduction of environmentally-induced x-ray fluxes also allows for the use of x-rays in space situational awareness applications, where spacecraft could determine the presence of nearby debris objects by their x-ray emissions.

Future work can examine more realistic distributions of materials and non-planar surfaces, where electric fields around these complex shapes will focus incident electrons into certain regions. Both of these factors complicate the analysis, but will yield high fidelity models of the x-ray spectra generated by the interaction of the object with the space environment. The focusing effects of electric fields could be used to estimate the charge distribution on the object directly if high resolution soft x-ray imaging techniques are used.

## Chapter 5

### Comparison and fusion of methods for remote potential sensing

In addition to the x-ray spectroscopic method for electrostatic potential sensing described thus far, another method has been developed in parallel by other researchers in the lab group, primarily Miles Bengtson. This method involves measuring the energy distribution of secondary electrons and photoelectrons emitted by the object of interest. Both types of electrons are emitted with initial energies of a few eV, so the energy with which the electrons arrive at the servicing craft is equal to the potential difference through which they have been accelerated. If the potential of the servicing craft is known, then the potential of the target object is determined [15, 16].

Each sensing method is analyzed individually in the literature and each method has unique strengths and limitations. This chapter considers the fusion of data from both methods to generate an estimate of the electrostatic potential with higher signal availability and accuracy than either method could provide independently. Rather than using only one of the methods, this chapter demonstrates that future missions could incorporate both sensors into an electrostatic characterization suite for more robust sensing capabilities, without adding significant complexity or requirements to the servicing spacecraft.

#### 5.1 Overview of electron spectroscopic potential determination method

As discussed in Chapter 1, energetic electrons impacting a surface can produce additional secondary electrons with energies of a few eV. The peak of the secondary electron initial energy distribution is equal to one-third the work function of the surface material, which is typically a

few eV. The number of secondary electrons produced for a single incident electron is known as the secondary electron emission (SEE) yield, a material-dependent property that is a function of the incident electron energy, angle, and material surface preparation [95]. The SEE yield can vary from a small fraction to values of 5 or greater, and typically increases as the incident beam becomes more off-normal to the surface [30]. This is because for shallow angles, the incident particles deposit more energy closer to the surface, generating secondary electrons with a greater chance of escaping the material.

The prospects and challenges of the electron method for remote potential sensing are discussed in Reference [15], but are briefly reviewed here. The electron method for remote sensing leverages the fact that secondary electrons are generated with very small initial energies regardless of the incident particle energy. These electrons are then accelerated by the electric field towards a positively-biased servicing craft, which collects them using an electron energy analyzer. Electron energy analyzers are ubiquitous on satellites and therefore have extensive flight heritage (e.g. [87, 32, 124, 161]). The energy of the electrons is equal to the potential difference between the two craft. Therefore, if the voltage of the servicing craft is known, the voltage of the object of interest is determined.

There are some complications, however, primarily related the geometric constraints imposed by the electric field structure between the servicer and the target. The electric field is a product of the target's geometry, as is discussed in Section 5.4. Therefore, the electrons generated on the target may not fly toward the sensing craft unless the sensing craft is in a favorable relative position, and with a favorable relative potential. Debris objects are commonly tumbling, so there will be times and relative attitudes for which the target voltage is unobservable using the electron method. Plasma-induced secondary electron and photoelectric currents also provide measurable signals without requiring an active electron beam.

A retarding potential analyzer (RPA) is used to collect electron spectra, and the RPA design is discussed in detail in Chapter 3. An example secondary electron spectrum collected by a retarding potential analyzer (RPA) is shown in Figure 5.1. To obtain this data, an electron beam is directed at an aluminum plate which is held at a fixed potential of -511 V, indicated by the dashed vertical

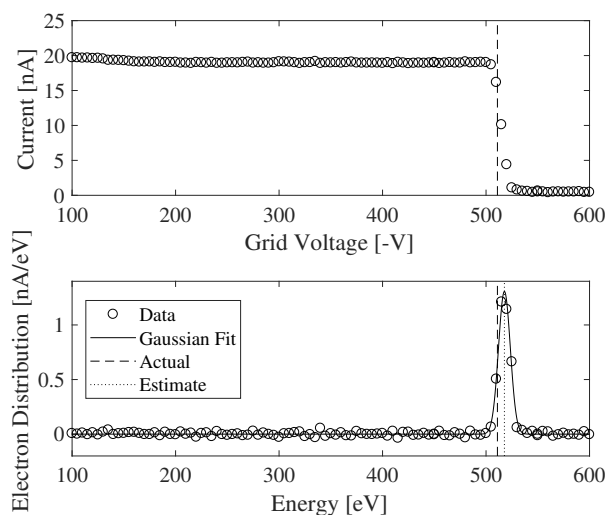


Figure 5.1: Example electron spectrum generated by a 10 keV, 10  $\mu\text{A}$  electron beam incident on an aluminum plate. The top panel shows the collected current as a function of discriminating grid voltage. The lower panel shows the electron distribution, Gaussian fit, and estimated voltage (dotted vertical line). The dashed vertical line gives the actual plate voltage.

line in both panels. The top panel of Figure 5.1 shows the current-voltage curve. Taking a derivative of this gives the actual electron energy distribution, as shown in the lower panel. A Gaussian curve is fit to the electron energy distribution data and the peak of the curve is taken as the estimate of the plate potential. For the example shown, the estimated voltage is -518 V whereas the actual plate voltage was -511 V. This gives an error of 1.37%. The 95% confidence bounds on the Gaussian fit are taken as the uncertainty associated with the measurement. The noise floor of the electron energy distribution is 0.0605 nA/eV whereas the peak of the Gaussian model is 1.308 nA/eV, giving a signal-to-noise ratio of 21.6. As the total signal received by the RPA decreases, the peak height of the energy distribution tends toward the noise floor and the uncertainty bounds increase toward infinity.

Several systematic error sources contribute to the uncertainty of the electron method. Misalignment between the electron trajectory and the central axis of the RPA reduces accuracy, as the RPA is ultimately a velocity filter, not an energy filter. Off-axis particles are filtered when the voltage on the grid is lower than their total energy shifting the electron energy distribution towards

lower energies. The shift in energy is given by [47]:

$$\frac{\Delta E}{E} = \sin^2 \theta, \quad (5.1)$$

where  $\theta$  is the off-axis angle of the particles. Even though the aperture of the RPA is aligned with the electron beam spot on the plate, the electric field from the plate and ambient magnetic field can steer the particles such that they enter the RPA at an angle. The ambient magnetic field in the vacuum chamber is on the order of  $40 \mu\text{T}$ , leading to electron gyroradii an order of magnitude larger than the distances of interest. The purpose of RPA grids is to form equipotential planes for particle filtering; however, these grids are imperfect because the voltage in the center of a grid square is less than the voltage applied to the actual grid wires [47]. This causes a broadening of the electron peak, which results in an increase of the peak width of  $\frac{\Delta E}{E} = 2.1\%$  for the RPA used in the experiments. Finally, contaminants and oxide layers on the target surface and cause small, localized potential variations on the order of a volt which affect the measured plate potential, while the secondary electrons are generated with an initial energy distribution spanning a few eV which also contributes to the peak location and width [130].

Though in Figure 5.1 the estimate is slightly larger (in magnitude) than the actual plate voltage, this is not always the case. The measurement is affected by the alignment of the RPA relative to the particle flight directions, the design of the RPA, and the surface conditions of the target. Recent experimental campaigns have shown that the electron method is accurate to within a few percent error for a wide range of test conditions and there is not a systematic bias to estimate higher or lower [16].

## 5.2 Comparison of touchless potential sensing methods

While both x-ray and electron spectra can be collected from a single target simultaneously, there are significant differences in performance between the methods in accuracy and signal availability.

The x-ray method tends to have higher uncertainties ( $< 100\text{V}$ , typical) in the measured

potential than the secondary electron method ( $< 10\text{V}$ , typical), for cases with good signal-to-noise ratios for both methods. This difference is largely due to the more stochastic processes underlying bremsstrahlung generation and emission, and the increased noise sources in the x-ray sensor compared to the RPA. However, the x-ray spectra are collected in seconds, while electron spectra require up to a minute using the power supplies available in the ECLIPS facility. While accuracies and sampling rates are important considerations, they are only relevant if a signal is actually observable. Both methods rely on unique physics which impact signal availability.

Unlike the experimental results for x-ray based potential sensing presented in Chapter 3, the secondary electrons have an angular distribution that affects the collected yield at a given position. However, this distribution is a small effect relative to the electric fields resulting from target geometries. In an operational scenario, the servicer translates relative to the target, and the target is likely to be rotating relative to the servicer. However, the instruments and the electron beam would be mounted at fixed points on the servicer. This results in a constant angle between the sensors and the electron beam, so the x-ray sensor will always be observing the same portion of the bremsstrahlung spectrum. The orientation relative to the target's surface will be varying with time, so the secondary electron flux observed changes significantly.

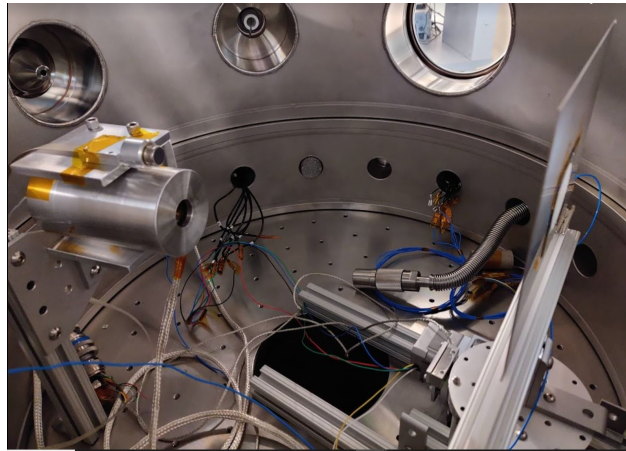


Figure 5.2: Experiment to collect electron and x-ray spectra simultaneously. The x-ray detector is mounted atop the RPA (left), just under the electron gun feedthru (top left). The target plate (right) is mounted to a rotary stage (bottom right) to control its angle.

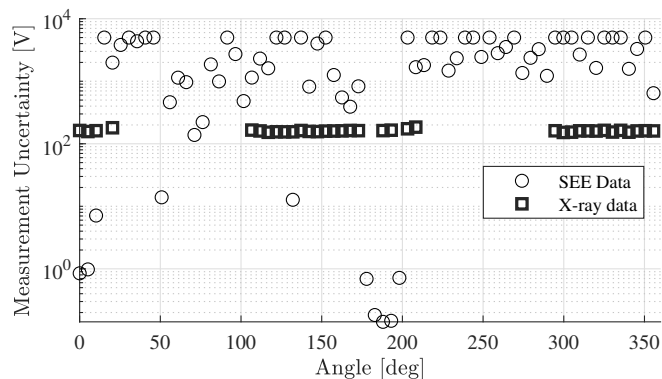


Figure 5.3: Uncertainty in plate potential determination as a function of target plate angle.

To demonstrate the effect of a non-stationary target on the signal observed by each detector, an experiment with a rotating plate is performed, analogous to a servicing mission with a rotating target. This experiment, seen in Figure 5.2, consists of an aluminum plate mounted to a rotational stage while the sensors are in a fixed position inside the chamber as discussed in the rotating plate experiments in Chapter 3. The potential of the plate is held at -511 V by a high voltage power supply, and the plate potential is held constant while the plate rotates.

Initially, the target is stationary while electron and x-ray spectra were collected. After collecting a spectrum at a given point, the plate was rotated by  $5^\circ$ , and new spectra collected. The plate angle is defined as the angle between the plate normal and the instrument positions. Therefore, angles of  $0^\circ$ ,  $180^\circ$ , and  $360^\circ$  indicate that the plate is facing the instruments. The electron gun parameters were held constant throughout the experiment at 10 keV emission energy and a beam current of  $10 \mu\text{A}$ .

Figure 5.3 illustrates the uncertainty in potential estimation for both methods as a function of plate angle relative to the detector. At some angles, particularly around  $0^\circ$  and  $180^\circ$ , the electron-based method returns highly confident results with uncertainties of less than a volt. As the plate rotates, significant variation of over 5 orders of magnitude is observed in the uncertainty in the target potential based on the electron data. In comparison, for this test case the x-ray data never has an uncertainty of less than 100V, but also has less than a 50% variation over all angles with

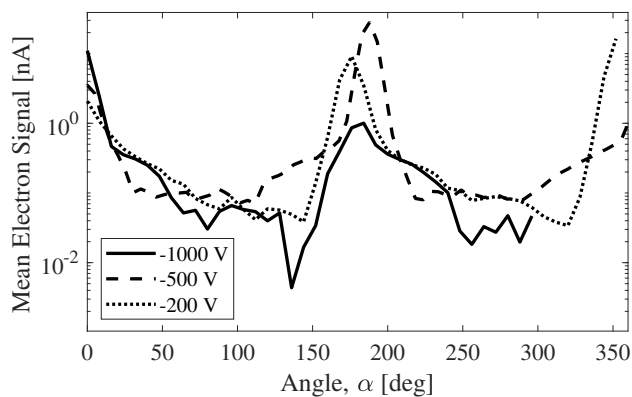


Figure 5.4: Mean SEE signal as a function of angle between the plate normal and the instrument location for various voltages.

signal availability.

Figure 5.4 shows the mean collected electron current as the target plate rotated through a full revolution for several plate voltages, with a constant set of electron beam parameters (10 keV, 10  $\mu\text{A}$ ). Note that a measurable peak in the electron data is only obtainable if the total signal is greater than 0.8 nA. During each test, the total signal exceeded this threshold 17% of the time. Therefore, the SEE method only produces quality measurements for a narrow range of angles when the detector is aligned near the plate normal. The distribution of electrons from more complex target shapes are explored through simulation in Section 5.4.

As discussed in Chapter 3, some plate orientations result in signals from the chamber walls as well as the target plate, as identified through characteristic radiation. For the case of a 2D plate with the limitations introduced by the chamber geometry, over 100° of the plate’s 180° rotation provide a high quality signal, with the signal from another 60° contaminated by chamber wall interactions. Ultimately, a useable signal is expected for over 75% of a target’s rotation.

It is possible to obtain a signal from at least one of the methods through most angles, even with the x-ray measurements being limited due to the electron beam impinging on the chamber walls. Without these contaminating cases, a usable x-ray spectrum would be observed in over 75% of cases, with fairly consistent uncertainties and errors as seen in Figure 5.3. Periods of unobservability were due to the angular separation between the electron beam and the detector,

where the electron beam would impact the face of the target plate opposite from the x-ray detector. Co-alignment of the electron beam and x-ray spectrometer aperture would eliminate these periods of unobservability, though electron beam deflection could limit the generated x-ray flux [131].

While the SEE data provides a highly accurate solution with low uncertainties when the geometry is optimally oriented, the confidence in the computed solution quickly decreases for off-normal geometries because no electron signal is actually measured, as seen in Figure 5.9. The uncertainty from the x-ray method is comparatively large in the best cases, but varies far less as the target rotates. The relationship between angle and uncertainty for the stationary plate case is illustrated in Figure 5.3.

### 5.3 Fusion of potential sensing methods

Each method has unique strengths and limitations, which makes fusing the data from both sensors appealing. Data fusion is often performed through the use of a Kalman filter, which requires some underlying dynamical model of the system. In this case the system is the spacecraft-environment interaction, and the state of interest is the evolution of the target body potential.

On-orbit charging involves a range of current sources, dominated by interactions with plasma electrons, ions, photoelectrons and the backscattered and secondary electrons associated with those currents. For a given space environment condition, spacecraft reach an equilibrium potential very quickly, typically seconds or less [102]. All of these environmental currents are highly dependent on material properties and the spacecraft surface potential, which makes developing an accurate dynamic model of the charging very challenging. While the spacecraft equilibrates to a new environment quickly, the charge state evolves on the order of minutes to hours as space weather conditions change. However, after reaching an equilibrium potential, spacecraft tend to vary in potential quite slowly, such that a steady state approximation could be applied in filter development in the absence of a higher fidelity model.

An alternative model-free method that better captures changing potential measurements is a filter that adapts the process noise parameter as a function of the measurement, confidence and

residual at each time step [6]. The filter chosen estimates the potential, and then computes the residual of the actual measurement at that timestep. This residual is then normalized by the uncertainty in the measurement, which prevents particularly noisy low-confidence results (such as SEE data with a very low SNR and resultant very high uncertainty) from triggering a dramatic change in the process noise. The normalized residual is then checked against a tunable threshold, which was set to 0.4 based on observations of the actual noise of the measurements and expected changes. If the threshold is exceeded, then the normalized residual is used to scale the process noise. Therefore, if a measurement with a high residual but low uncertainty is observed, the filter will significantly increase the process noise to account for the (presumed) change in target state. This method was found to be more effective at tracking transients, such as those that could be expected during an eclipse crossing, than alternative methods such as adding a fading memory term to a steady state filter.

---

**Algorithm 1:** Adaptive Kalman filter pseudocode implementation [6]

---

```

1  $Xp_i = AX_{i-1}$       Prediction of the estimate;
2  $r_i = \frac{z - Xp_i}{R}$     Compute normalized residual;
3 if  $r_i > 0.4$  then
4   |  $Q = Q(1 + r_i)$     If normalized residual exceeds threshold, scale process noise;
5 else
6   |  $Q = 1$ 
7 end
8  $Pp_i = AP_{i-1}A^T + Q$     Prediction of error covariance;
9  $K_i = Pp_i H^T (HPp_i H^T + R)^{-1}$     compute Kalman gain;
10  $X_i = Xp_i + K_i(z_i - HXp_i)$     compute state estimate;
11  $P_i = Pp_i - K_i H Pp_i$     compute error covariance;

```

---

For the steady-state assumption, the Kalman filter system state matrix  $A$  is set equal to identity. The states and the system state matrix are both scalars since only the target potential is to be estimated. The measurement vector,  $z$ , consists of the x-ray measurement and electron measurement for a given timestep stacked into a  $2 \times 1$  vector. The measurements are directly equal to the state of interest, so the measurement-to-state conversion matrix  $H$  is a  $2 \times 1$  vector of ones. The process noise matrix  $Q$  (in this case a scalar quantity) is tuned, and good filter performance

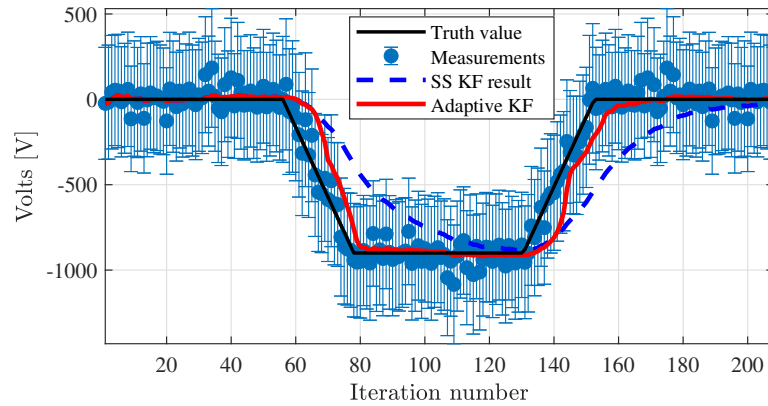


Figure 5.5: Application of adaptive filter to simulated data with eclipse-like transients.

with satisfactory convergence (to within 10V of a truth value after initialization at a 500V error in under 10 iterations) occurs when  $Q$  is set to identity.

To generate a dataset for filtering use, an experiment is conducted with an aluminum plate maintained at a fixed potential ( $-900\text{V}$ ). The electron gun then targets the plate with a fixed energy and current ( $10\text{ keV}$  and  $10\ \mu\text{A}$ ), while electron and x-ray spectra are collected. A total of 60 spectra of each type are collected. These spectra are used to generate a set of measurements that are superimposed on a desired trend to simulate an eclipse scenario, as seen in Figure 5.5. This provides a dataset to compare performance of the steady-state and adaptive Kalman filters. The adaptive filter performed much better over the dataset shown in Figure 5.5, with mean errors of less than 50V, less than  $1/3$  of the errors from a filter without adaptive process noise terms. For a static voltage case the performance is equivalent to that achieved by a steady-state filter.

Ultimately, this filter provides an example method for fusing data from both sensors, and accounts for the uncertainty in the potential estimated by each sensing method at each time step. Depending on the relative geometry between the target and the servicer only a degraded or insignificant signal may be available for each method. Therefore, this filter could effectively combine the measurements to attain an estimate with the overall signal availability of the x-ray method and the accuracy of the electron-based method when a signal is available.

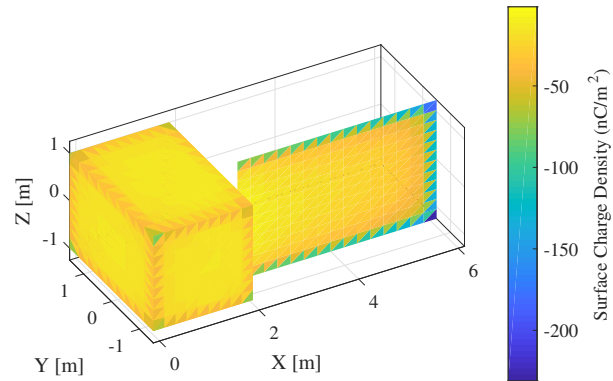


Figure 5.6: Target spacecraft body.

## 5.4 Simulation of spacecraft servicing scenario

Section 5.3 demonstrated how experimental data for both methods could be combined to achieve a more robust signal than either method individually. However, numerical simulation of a spacecraft rendezvous scenario provides an example of how these systems could be used in practice with more complicated target geometry than a flat plate, and anticipated signal availability at far greater ranges than can be experimentally achieved. A target with an uncontrolled  $0.2^\circ/\text{s}$  tumble rate is established, and the returned electron and x-ray photon fluxes are computed as the servicer approaches from 100 meters to 10 meters. The target body model, which consists of a rectangular bus with a single solar array, is shown in Figure 5.6, and development of this model was discussed in Chapter 2.

### 5.4.1 Electron signal analysis

A simulation is developed to model the fluxes of electrons around the target to determine the expected electron signal as the servicer craft approaches the target. To gain insight into the electron distribution, only electrons generated in-plane with the servicer (along the  $Z = 0$  m plane in Figure 5.6) are considered, though this methodology can be extended to a 3D simulation as necessary.

First, the target geometry is discretized into triangular elements (as seen in Figure 5.6), and the target capacitance matrix is computed using the Method of Moments [61, 35]. The target is assumed to be continuously conducting and therefore equipotential, allowing the charge on each triangular element to be determined via the capacitance matrix. Next, the Method of Moments is used to determine the electric field at a given point by numerically integrating over the charge of each triangular element. Given the electric field, the motion of an electron near the target is integrated using the Boris algorithm [27, 127].

Figure 5.7 shows electron trajectories after emission from the target surfaces. Crucially, the electric fields resulting from the target geometry focus or deflect the emitted electrons. Note the plot is not symmetric about the X axis because the solar panel on the right side of the box is located at  $Y = -0.5$  m rather than at  $Y = 0$  m. Particles are generated on the target centerline with a constant linear density of 60 particles/meter. As a result, the relative density of the particle trajectories (black lines) corresponds to signal magnitude. For example, the electric field near the corners of the box or end of the solar panel spread particles out, resulting in a lower signal. Particles near the interior corner where the solar panel meets the box are focused into a smaller spatial region with a large signal. A total of 1080 particles are simulated in the XY plane, with each generated evenly on the target surface with zero initial velocity. Though the presence of a magnetic field affects the particle trajectories through gyromotion, the gyroradius for 5 keV electrons interacting with the relatively low  $\sim 100$  nT magnetic fields at GEO [28] is over 2 km; even 500 eV electrons have gyroradii of 800 m, much larger than the  $< 100$ m distances of interest. Therefore, the magnetic field is assumed to be zero here to allow the effects of the target geometry to be investigated with greater clarity.

Figure 5.8 shows the location of the servicing craft in the target body frame (red dots), along with the electrons emitted from the target. The servicer craft begins the simulation at the point located at  $X = 100$  m. As the servicer approaches the target, the target rotates. As a result, the electron signal observed by the servicer varies. The number of simulated particles which enter a 0.5 m radius sphere centered at each measurement location is counted, which provides a relative

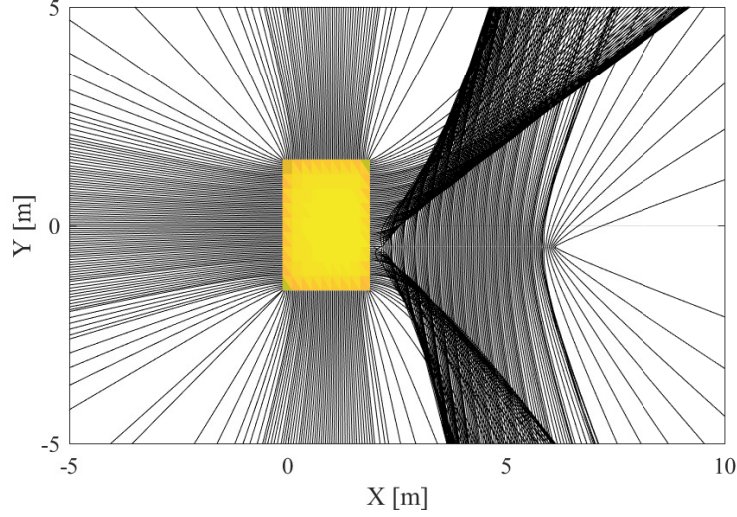


Figure 5.7: Close-up view of electrons emitted from target surface. The solar panel is located to the right of box.

estimate of the particle fluxes expected from the target. To convert this simulated signal from particles to a current in nA, it is assumed that the servicer craft directs a  $1 \mu\text{A}$  beam toward the target and that the beam has a landing energy of 20 keV. While the Secondary Electron Yield (SEY) is often highly material dependent [95], but is estimated by [44]:

$$\delta = \frac{4\delta_{\max}(E_0/E_{\delta_{\max}})}{(1 + (E_0/E_{\delta_{\max}}))^2}, \quad (5.2)$$

where  $\delta$  is the number of secondaries produced for every incident electron (the SEY),  $E_0$  is the landing energy in eV, and  $\delta_{\max}$  and  $E_{\delta_{\max}}$  are the maximum SEY and energy at which the maximum SEY occurs for a given material. The target object is assumed to be aluminum, so values of 0.97 and 300 eV are used for  $\delta_{\max}$  and  $E_{\delta_{\max}}$ , respectively [91]. Given these parameters, the SEY at a landing energy of 20 keV is 0.0565.

It is assumed that the  $1 \mu\text{A}$  primary electron beam is expanded to hit the entire target, so the total current emitted from the side of the target hit by the beam is 56.5 nA. To determine which elements are visible from the servicer craft at a given location, the vector normal to the surface of each triangular element is computed. Next, the dot product between the surface normal vectors and the position vector from the target to the servicer is found. Elements with a positive

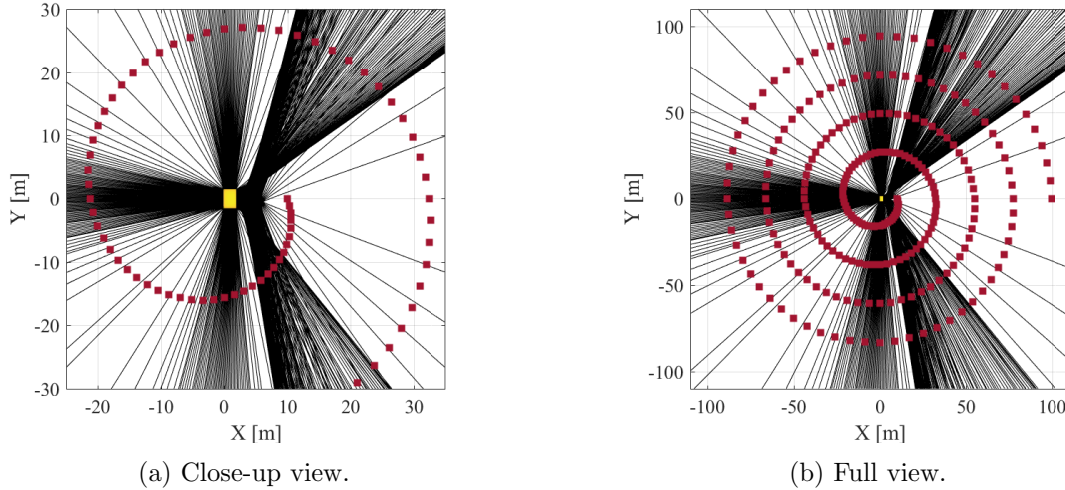


Figure 5.8: Views of electrons (black lines) emitted from target surface and servicer craft measurement points (red dots) in the target body frame.

dot product are thus visible by the servicer. Though there is a small amount of self-shadowing, it is sufficient for the purposes here to neglect such higher-order effects. Therefore, the number of particles captured at a given measurement point are divided by the particles emitted from the triangular elements visible from the servicer at that point. This fraction is then multiplied by the total 56.5 nA current emitted from the target, scaling the discrete particle simulation to an expected current observed by the servicer at each point.

Figure 5.9 shows the expected signal measured by the servicing craft as a function of distance from the target. Several interesting features are visible in the data. First, the signal magnitude increases as the servicer gets closer to the target, which is to be expected because the electron current expands out into space as it travels away from the target. However, the focusing effect of the target geometry highly significant. Electrons do not leave the target isotropically despite uniform emission from the surface, but instead are emitted in specific channels. A few dominant directions are observed in Figure 5.7, as the electrons have been focused by the target's electric field. A repetitive pattern is seen in the data, with clear similarities between the peaks at 28 51, 73, and 96 m; 21, 44, 66, and 88 m; and 13, 37, 60, and 82 m. The repeating pattern is a result of

the servicing craft sampling the electron flux from the target as the target rotates multiple times during the approach. There are three dominant peaks in each pattern: the electrons focused by the interior corner where the box and panel are joined, the electrons emitted from the flat side of the box on the opposite of the panel, and then the interior corner on the other side. The target rotates through four full rotations during the simulation, so the pattern of three peaks is observed four times, for a total of 12 main peaks.

The expected signal is useful for determining when the potential of the target is observable. By assuming the sensitivity of the servicer's electron detector, the simulation results demonstrate how often the electron signal is large enough for a potential measurement. For example, assume a 0.5 nA electron current is required to accurately resolve the potential of the target by measuring the energy of the electron population in the presence of an ambient plasma environment. In this case, a signal greater than 0.5 nA is available for 30% of the sample positions.

Simulations are conducted for target voltages of -500, -1000, and -5000 V. Interestingly, the electron trajectories, and thus the expected signal at the servicer, are independent of the target voltage over the range considered. The relative charge distribution on the target spacecraft is constant regardless of its potential. The total amount of charge on the target scales with voltage, but the relative location of the charge on the target is entirely determined by the geometry of the target. Therefore, the electric field magnitude changes with larger (magnitude) target voltages, but the electric field direction does not change. Because electrons are highly mobile due to their small mass, the electron trajectories are insensitive to surface potential magnitudes, even though the energy of the electron population changes. This is advantageous for the electron-based touchless sensing concept because the signal availability is determined from the target geometry before the potential of the target is known.

Complex, multi-faceted targets, such as the simulated servicing target, have more complicated electric fields than the flat plates used in experiments, which drives significant variations in electron signal availability. The results for one target spacecraft geometry do not readily generalize to others, so such analysis should be carried out for any anticipated target. The following section considers

the x-ray signal from the target body.

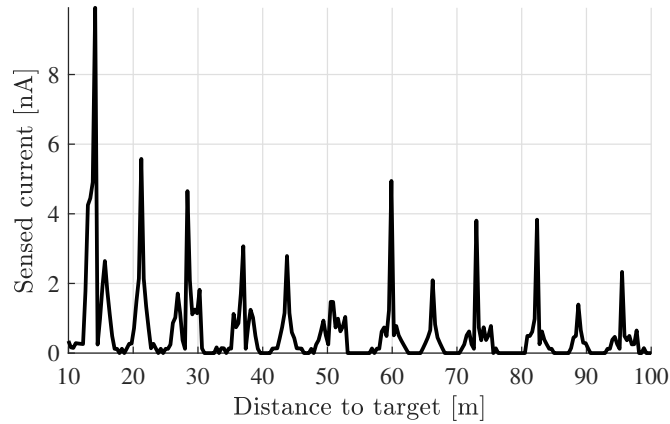


Figure 5.9: Sensed secondary electron yield from target, assuming  $1 \mu\text{A}$  beam at 20 keV.

#### 5.4.2 X-Ray signal analysis

The methodology applied to simulate bremsstrahlung emission from the environment is derived from the approach in Chapter 4. Both an active and passive sensing method are evaluated, using the same beam parameters prescribed for the electron sensing case. Plasma electron fluxes are provided by the mean electron flux IGE-2006 model for geostationary orbit [145]. Higher level effects, such as solar x-ray secondary fluorescence from the target were considered to be negligible [164].

The passive method relies on the change in total number of photons emitted by hot electrons in the ambient plasma, and therefore has no sampling requirement to construct a spectrum. Such a method may be effectively executed with tens or hundreds of photons, which may be collected over several seconds. However, using the assumption of even photon flux from the entire surface of the target body, this method would be sensitive to the apparent area of the target facing the servicer. This apparent projected area is a function of the distance between the spacecraft, and also the orientation of the target. Therefore, when comparing the apparent brightness of the target for passive potential estimation, it is important to simultaneously account for target pose and position.

Figure 5.11 illustrates the evolution of the target’s apparent brightness due to hot electrons in the ambient plasma. As the target rotates, the projected area seen by the servicer varies by a factor of 3, resulting in periodic variation in the sensed flux.

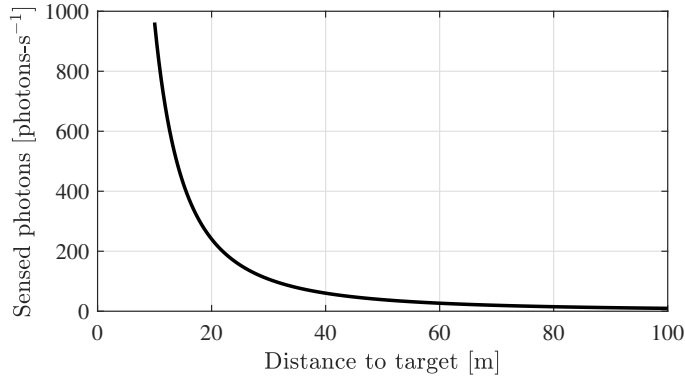


Figure 5.10: Photons observed by servicer, with 1  $\mu\text{A}$ , 30kV electron beam impacting target.

Experiments demonstrate that detection of  $\sim 1000$  photons are sufficient for an accurate bremsstrahlung spectrum and landing energy to be computed. From Figure 5.10, this equates to collection periods of tens of seconds at 50 meters, but just 1 second at 10 meters. Knowledge of electrostatic potential becomes significantly more important as distance to the target decreases, as electrostatic forces increase with  $1/r^2$  and the risk of ESD increases near contact. At a distance of 100 meters approximately 10 photons per second are anticipated, while the photon counting rate increases by two orders of magnitude at 10 meters. Therefore, the update rate for electrostatic potential estimates can increase from the order of minutes to seconds as the servicer approaches the target.

Several means are available to improve sensed photon yields, which can improve the accuracy of the x-ray spectroscopic potential measurement technique. X-ray optics increase the effective detector area by an order of magnitude or more [115]. Additionally, the bremsstrahlung yield increases significantly as the landing energy of the electrons increases. Moving from a 20 keV landing energy to 30 keV, for instance, doubles the photon yield. Likewise, increasing beam current would linearly increase photon yields. However, manipulating beam parameters will affect the

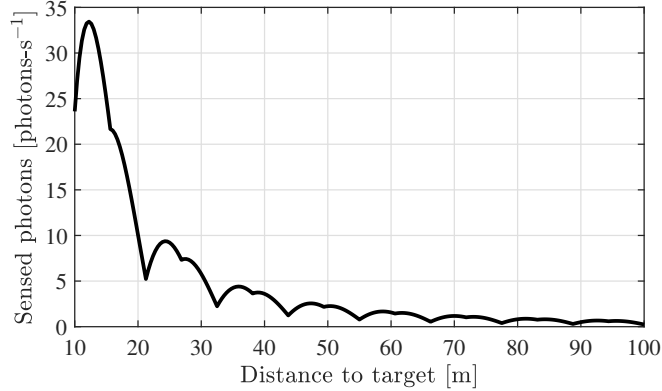


Figure 5.11: Photon flux sensed at servicer as a result of target-plasma interactions.

equilibrium potential of the target body, so such changes must be carefully considered to avoid undesired impacts.

The simulation demonstrates signal availability trends for both methods, with conclusions analogous to the experimental flat-plate case. Electron signals are highly dependent on relative geometries, but can provide a highly accurate signal when available. The x-ray signal is unaffected by the target orientation when an electron beam is used to generate x-rays, and shows only moderate dependence on attitude when observing environmentally-induced x-ray fluxes. For all cases, signal magnitude increases significantly at short ranges, though the focusing effects of the target geometry can provide strong electron signals at long ranges, if relative positions are correctly aligned.

## 5.5 Conclusion

Electron and x-ray spectral methods for remote sensing of spacecraft electrostatic potential have been evaluated through experiments and simulations. A key result is that, if a sufficient signal is available, the electron-based method outperforms the x-ray sensing method, providing accuracies on the order of volts. However, signal availability for this method is limited due to the focusing or diverging of electron trajectories due to electric fields around the target object. This trend is observed experimentally and through simulation of a target spacecraft geometry. In contrast, the x-ray method provides uncertainties around 100V, but signal availability is fairly agnostic to the

geometry of the target surface. Further, the x-ray method does not place any requirements on the relative potentials of the two objects, whereas the electron method only works if the electrons are accelerated toward the servicing satellite. Fusing the datasets using an appropriate filter mitigates some of the limitations of each method, thereby producing an estimate of the plate potential with smaller errors and uncertainties that is robust to target orientation. Either electron beams or hot electrons in the ambient plasma provide sufficient emission for both methods.

Continuously conducting spacecraft at a single potential are assumed in this work. However, spacecraft often experience differential charging, in which different parts of the spacecraft charge to different potentials. This effect significantly complicates the measurement process for both methods, and should be considered in future work.

## Chapter 6

# Impact of Electrostatic Perturbations on Proximity Operations in High Earth Orbits

### 6.1 Problem formulation

This chapter analyzes the impact of charged spacecraft on the dynamics of close proximity operations between an active spacecraft and an inert or disabled target object flying tens of meters apart, as seen in Figure 6.1. This chapter is organized as follows: first, the general frequency of spacecraft charging in high Earth orbits is discussed for context. Next, the multi-sphere method (MSM) is applied in developing a 6-DOF, 2-craft simulation of a controlled servicer and two types of inert target vehicle. Results from simulations with different spacecraft geometries for both rendezvous trajectories and relative station keeping are analyzed, and the results compared to perturbations resulting from Solar Radiation Pressure (SRP). Finally, a rendezvous scenario is used as an alternative demonstration of electrostatic charging impacts on relative motion.

The spacecraft used for a proximity operations baseline are the MSM models of a two-panel servicer and an asymmetric one-panel uncooperative target craft discussed in Chapter 2.

The perturbations of interest occur over small separation distances on the order of tens of meters. Thus the final stage of a rendezvous and docking process is considered where the servicer slowly approaches a target vehicle and has brief target-relative hold periods to evaluate mission parameters before docking. Additionally, these effects are predominant in regions of high spacecraft charging, such as GEO. The combination of very close formation flight (tens of meters), large orbital radii with small eccentricities ( $a$  over 42000 km,  $e = 0.0001$ ) and relatively short time

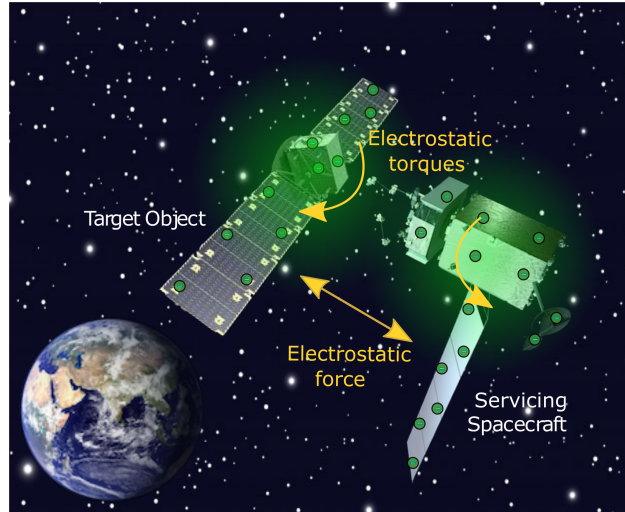


Figure 6.1: Electrostatic force and torque interactions between spacecraft in close proximity.

periods makes the dynamics well suited to linearization. As a result the Hill-Clohessey-Whiltshire (HCW) equations of relative motion are used [134]. The components  $a_x, a_y, a_z$  represent the Hill-frame components of acceleration contributed by perturbing forces, whether electrostatic or control thrust;  $n$  is the orbital mean motion.

$$\begin{aligned}
 \ddot{x} &= 3n^2x + 2n\dot{y} + a_x \\
 \ddot{y} &= -2n\dot{x} + a_y \\
 \ddot{z} &= -n^2z + a_z
 \end{aligned} \tag{6.1}$$

Two spacecraft are established as deputies relative to a virtual Keplerian chief orbiting in a GEO graveyard. The deputies exert mutual forces and torques due to electrostatic interactions such that they exhibit perturbed motion relative to the Keplerian chief frame  $\mathcal{H}$ . The first deputy, which represents the uncontrolled target for rendezvous, is initially located at the origin of the HCW frame, while the second spacecraft (the controlled servicer) is set at an initial position determined by the scenario under consideration.

Translational dynamics constitute only one part of the problem, however. The two spacecraft exert mutual torques on each other which will perturb their attitudes. This has a strong impact on the servicer motion as it must approach in a prescribed manner relative to the target object

body frame. Thus, if the object is tumbling the servicer needs to match this motion to maintain a body-fixed approach. The external torque vector ( $\mathbf{L}$ ) acting on each craft is related to the angular rotational vector  $\boldsymbol{\omega}$  of each body by

$$[I]\dot{\boldsymbol{\omega}} = -\tilde{\boldsymbol{\omega}}[I]\boldsymbol{\omega} + \mathbf{L} \quad (6.2)$$

where the tilde represents the skew symmetric matrix operator equivalent to a vector cross product, and  $[I]$  represents the inertia tensor [134]. Quaternions are used to represent attitudes. The orientation of the servicer is prescribed to match the attitude of the target at each time step to simulate active relative attitude control of the servicer relative to the target object. At each time step the translational states and rates are integrated using the CW equations, while Euler's equation of rotational motion is used to integrate rotational rates and the quaternion differential equation of motion is used to integrate attitude states.

There are three relevant reference frames for this scenario:  $\mathcal{H}$ - an unperturbed co-orbiting origin point for the Hill frame which is treated as an inertial frame,  $\mathcal{T}$ -a body-fixed frame on the target spacecraft,  $\mathcal{S}$ - a body-fixed frame at the docking point on the servicer. The servicer attitude reference frame  $\mathcal{T}$  fixed to the docking point on the target, as would be expected for a servicing scenario. As the target spacecraft rotates due to perturbing torques, the reference location is also rotated in the HCW frame. The initial positions of the spacecraft MSM models in a sample rendezvous trajectory is shown in Figure 6.2.

## 6.2 Charged Proximity Operations Study

All cases here are evaluated with equal potentials on each spacecraft. As both spacecraft are exposed to near-identical environmental conditions (assuming one is not shadowing the other), it is reasonable to assume that each has a similar potential, though there may be differences due to variations in design or material properties. As discussed earlier, the spacecraft are considered to be fully conducting, though specific target vehicles vary.

The results are organized as follows: first, the electrostatic forces and torques are evaluated

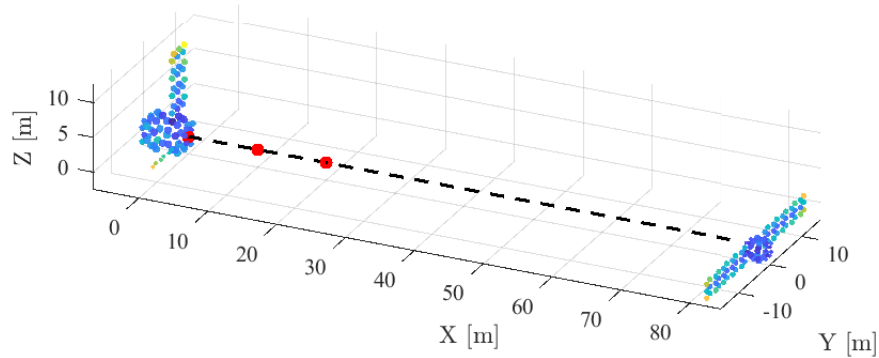


Figure 6.2: Initial position of the servicer (right) and uncooperative target (left). Red dots indicate hold points along a nominal rendezvous trajectory.

for both types of spacecraft as a function of position relative to the target, and as a function of potential. As a point of comparison, a basic SRP model considering the spacecraft model facets, but not considering self shadowing etc., is used to compare the significance of these perturbations. The impact of electrostatic perturbations in maintaining a static hold relative to a target is then evaluated, and fuel consumption compared between an SRP-only case and an SRP and electrostatically perturbed case. The servicer attitude control requirements during these operations are evaluated, and then a full rendezvous scenario with electrostatic perturbations is demonstrated.

### 6.2.1 Electrostatic force and torque magnitudes

The MSM formulation described in Chapter 2 is used to compute electrostatic forces and torques acting between the spacecraft. As seen in Equation (2.11), the electrostatic torque acting on a body is a function of the relative positions of each body, their orientations, the geometry of each body and the electrostatic potentials. To evaluate the magnitude of electrostatic forces and torques on the target as a function of servicer location, an equi-distant shell is developed. Rather than use a spherical shell where each point is an equal distance from the center of mass, each point is distributed such that it is an equal distance from the nearest surface on the target spacecraft, as seen in Figure 6.3. The servicer is oriented such that the docking face is oriented towards the

target center of mass, enabling comparisons to be drawn between the force and torque on the target at different sample positions. The multi-sphere method is used to compute the forces and torques acting on each body. The forces and torques acting on the GOES-R target as a function of servicer azimuth and elevation with a fixed distance from the target are seen in Figure 6.4a and 6.4b.

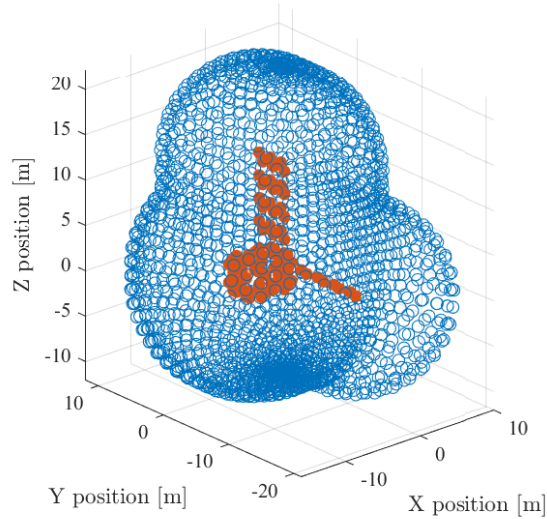
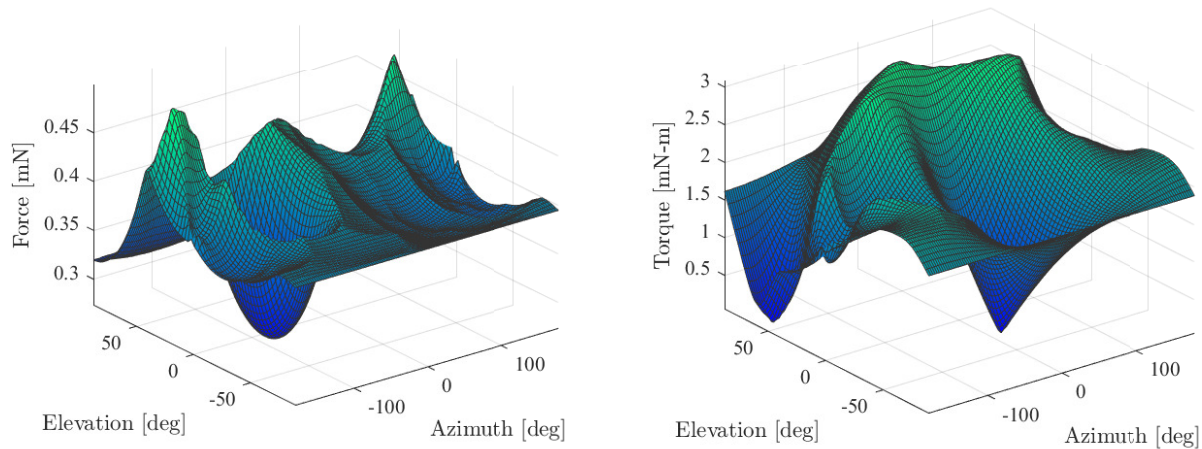


Figure 6.3: Sample points of constant distance (10 meters) to the spacecraft used to evaluate electrostatic torque on a target as a function of azimuth and elevation.

The maps of torque as a function of azimuth and elevation shown in Figures 6.5a and 6.5b provide some suggestions as to how a trajectory could be designed to minimize the perturbing torque acting on the target. For instance, approach along an azimuth of  $15^\circ$  and an elevation of  $-27^\circ$  decreases the torque imparted to the GOES-R spacecraft by a factor of 20 compared to a straight line approach at  $0^\circ$  azimuth and  $0^\circ$  elevation. A constraint cone is often used during approaches to ensure satisfactory navigation sensor performance and mission safety, and used to limit acceptable approach vectors. Emphasizing the importance of trajectory selection, electrostatic torques can vary by a factor of 50 while maintaining a  $25^\circ$  half angle approach cone constraint for this spacecraft configuration. In most cases of operational constraints imposed on a specific mission, it is possible to develop a feasible trajectory to minimize electrostatic torques.

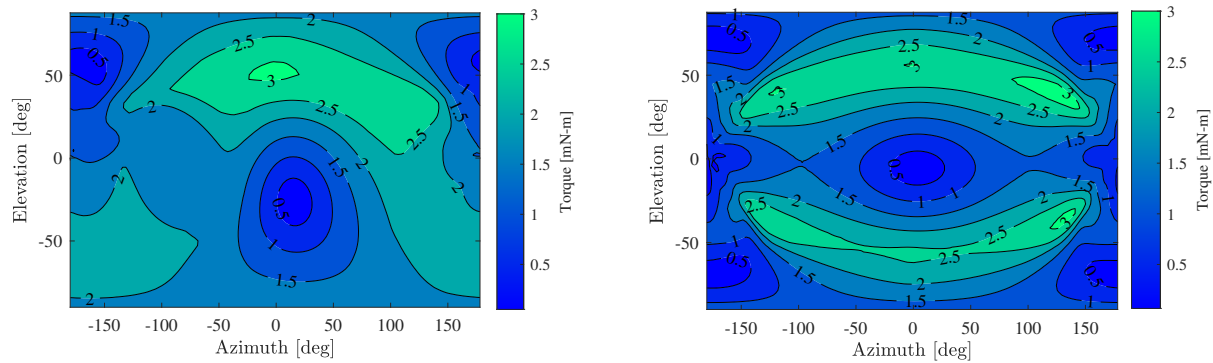
Minimizing the perturbing torque acting on the target is critical to reducing the target's



(a) Force on GOES-R target for different servicer azimuth and elevations.

(b) Torque magnitude acting on GOES-R target as a function of servicer position.

Figure 6.4: Force and torque for different servicer locations, with the servicer at 10 meters from the target. All evaluated at 10 kV, with a servicer based on the symmetric two-panel MSM model, and a target based on the GOES-R model.



(a) Electrostatic torque on GOES-R target

(b) Electrostatic torque on two panel target.

Figure 6.5: Torque magnitude acting on target as a function of servicer azimuth and elevation, with all positions located 10 meters from the target. All points evaluated at 10 kV.

acquired rotational rate at grappling, and therefore in reducing control effort required by the servicer and improving safety for the overall mission. In addition to path selection, electrostatic interactions can be minimized by adjusting the attitude of the servicing spacecraft with respect to the target. For the two-panel servicer and GOES-R target scenario, having the spacecraft panels pointing in the same direction results in torques over 30% larger than in a scenario where the panels are oriented along perpendicular axes. Likewise, altering the orientation of the solar arrays relative to the spacecraft frame will alter the electrostatic torques acting between the spacecraft.

Repeating the equidistant shells procedure for different positional offsets results in Figure 6.6, which illustrates the relationship between distance to the target, spacecraft potential, and resultant perturbing torque for both a two-panel and GOES-R target.

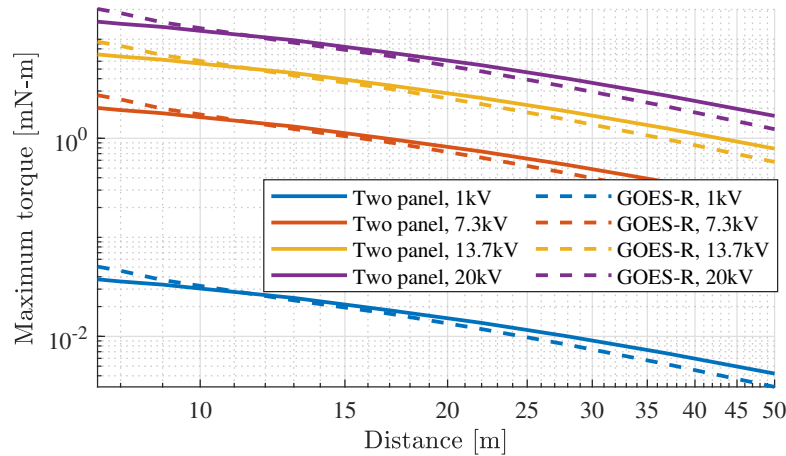


Figure 6.6: Maximum electrostatic torque between servicer and target as a function of distance.

### 6.2.2 Other Perturbations

Given the relatively high electrostatic potentials of interest in this problem, it is worth considering the dynamic effects of charged spacecraft interactions with the environment. Two interactions are considered: the effect of the charged spacecraft's interactions with Earth's magnetic field (Lorentz force) and ionospheric drag, due to the interaction of a charged spacecraft with ambient charged particles. The total charge on a spacecraft charged to a near-record -20 kV is approximately

$1 \times 10^{-5}$  C. The Lorentz force is computed as

$$\mathbf{F} = q(\mathbf{E} + \mathbf{v} \times \mathbf{B}) \quad (6.3)$$

which, given a nominal GEO magnetic field intensity of 106 nT [28], orbital velocity  $v = 3$  km/s and electric field intensity on the order of 1 mV/m [10], the Lorentz force is estimated to be on the order of  $10^{-8}$  N - approximately  $\frac{1}{3}$  the gravitational force exerted by the moon, and approximately 5-6 orders of magnitude smaller than inter-craft electrostatic forces.

Likewise, plasma densities at GEO are often very low compared to LEO orbits, with typical plasma densities on the order of  $10^5$  ions per cubic meter compared to a typical  $5 \times 10^{10}$  per cubic meter at 500 km, some 5 orders of magnitude larger [10, 62]. These low plasma densities, combined with lower orbital velocities than in LEO, result in negligible ionospheric drag forces.

### 6.2.3 Comparison to Solar Radiation Pressure

While the contributions of Lorentz forces and ionospheric drag are negligible for these orbits, the dominant perturbation at high earth orbits is typically SRP [147], which can affect a spacecraft's inertial acceleration and also impart significant torques. As a point of comparison for the significance of the electrostatic forces and torques, a first order estimate of the solar radiation pressure-induced torque is investigated. The spacecraft is divided into elements representing each panel in the MoM model in Figure 2.9, and a similar procedure is carried out for the two-panel spacecraft model; the front and back of the solar arrays is treated as separate faces to allow different reflection coefficients to be applied to each.

The SRP force per area element is computed as [93]

$$\mathbf{F}_i = -P_{\text{SRP}} \left( (1 - \beta_{s,i}) \hat{\mathbf{s}} + 2 \left( \beta_{s,i} \cos(\theta_i) + \frac{1}{3} \beta_{D,i} \right) \hat{\mathbf{n}}_i \right) \cos(\theta_i) A_i \quad (6.4)$$

where  $\beta_s$  represents the specular reflection coefficient, and  $\beta_D$  is the diffuse reflection coefficient for the given element. The sun direction unit vector is given by  $\hat{\mathbf{s}}$ , while  $\hat{\mathbf{n}}_i$  is the face normal unit vector;  $\theta_i$  describes the angle between  $\hat{\mathbf{s}}$  and  $\hat{\mathbf{n}}_i$ .  $A_i$  is the area of the given element.

The specular and diffuse reflection coefficients are taken from Reference [93], with the spacecraft structure assumed to be covered in multi-layer insulation (MLI,  $\beta_s = 0.29$ ,  $\beta_d = 0.29$ ), the back of the solar array to be black paint ( $\beta_s = 0.015$ ,  $\beta_d = 0.015$ ) and the front of the solar array to be given by  $\beta_s = 0.073$ ,  $\beta_d = 0.007$ . Self-shadowing and multiple reflection effects are neglected, and the resultant SRP force and torque are evaluated over a full range of azimuth and elevation angles for the incident sun vector. Torques are computed by treating the SRP force on a given area element as a point force applied to the center of area, with the position vector of the element centroid relative to the center of mass for the spacecraft used to find the resultant torques.

The mean SRP torque on the GOES-R model is found to be about 0.57 mN-m, with a worst-case torque of 1.1 mN-m; the two-panel model had a mean torque of 0.11 mN-m, and a worst-case SRP torque of 0.14 mN-m. For the two-panel model, a worst-case torque at 5 meters of separation and just 1000 V is sufficient to exceed the maximum SRP torque by a factor of three; at 10 meters, 1900 V results in electrostatic torques exceeding the maximum SRP torque for this body (Figure 6.6). Additionally, while SRP forces and torques decrease as the face rotates away from the sun, the electrostatic torques continue to be exerted as long as the servicer is maintaining a relative position, continuing the rotational acceleration of the target. Therefore, the electrostatic perturbations acting on the target are the dominant disturbance at GEO during periods of significant spacecraft charging.

#### 6.2.4 Perturbed Station Keeping

To gain further insight into the impact of electrostatic perturbations on proximity operations, a case where the servicer actively maintains a fixed position relative to the target is considered. In this case, the servicer maintains a position 10 meters from the target in the Hill-frame  $\hat{x}$  direction. Figure 6.7b shows the trajectory followed by the servicer over this period to maintain a fixed position at 10 meters from the target in the target frame. The target is initialized with no rotational motion, but is considered to be inert, and therefore affected by electrostatic perturbations. Each hold is evaluated over an arbitrary 5 hour period.

### 6.2.4.1 Controller Description

A Lyapunov-derived reference tracking controller is implemented to follow a desired trajectory, such as a position fixed in the target body frame  $\mathcal{T}$ , computing the required control authority as [134]

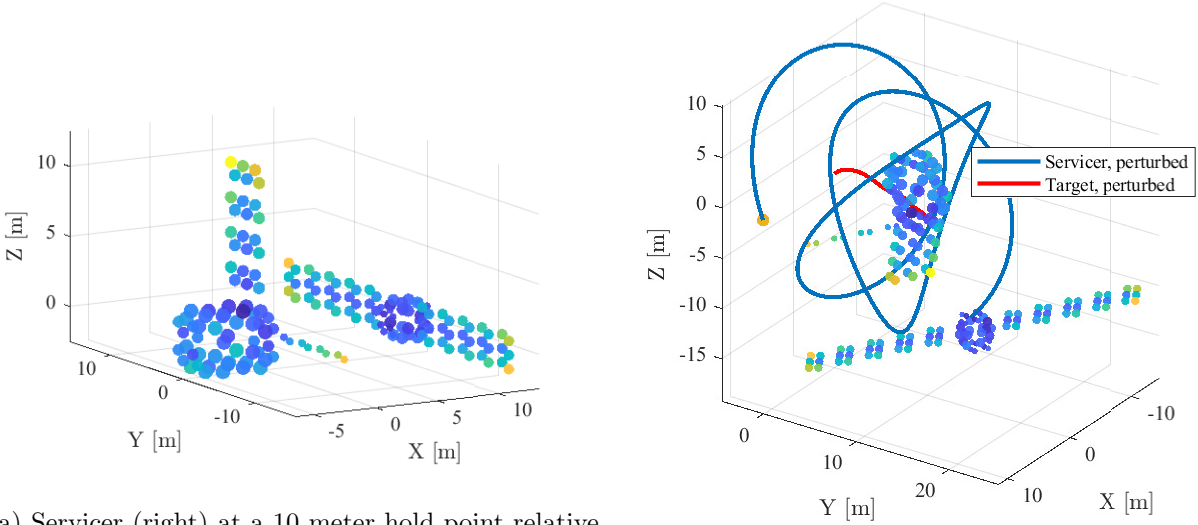
$$\mathbf{u} = -(\mathbf{f}(\mathbf{r}_d) - \mathbf{f}(\mathbf{r}_d^*)) - [K_1] \Delta \mathbf{r} - [K_2] \Delta \dot{\mathbf{r}} \quad (6.5)$$

where  $\Delta \mathbf{r} = \mathbf{r}_d - \mathbf{r}_d^*$  represents the difference between the spacecraft actual position  $\mathbf{r}_d$  and desired position  $\mathbf{r}_d^*$  in the target's reference frame, and  $\Delta \dot{\mathbf{r}}$  represents the velocity difference in the same frame. The term  $(\mathbf{f}(\mathbf{r}_d) - \mathbf{f}(\mathbf{r}_d^*))$  represents the relative inertial acceleration between the vehicle and the target orbit, evaluated numerically at each time step. To mimic a servicer case where the spacecraft potentials are unknown, this relative acceleration term includes only relative accelerations due to gravity, not the electrostatic perturbations. The gain matrices  $[K_1]$  and  $[K_2]$  are set to achieve desired performance, with  $[K_1] = 0.03 \cdot [I_{3 \times 3}] \text{s}^{-2}$  and  $[K_2] = 3 \cdot [I_{3 \times 3}] \text{s}^{-1}$  to achieve a closed loop response time on the order of minutes while avoiding thruster saturation, representative of such a rendezvous scenario.

The goal of this work is to evaluate the contribution of specifically electrostatic perturbations, so navigational or controller noise are not included in simulations and perfect knowledge of relative states assumed. However, the control authority is limited to account for thruster saturation effects. For the MEV-1 mission, final approach and rendezvous control was provided by a mix of 1-Newton and 22-Newton hydrazine thrusters developed by Aerojet Rocketdyne; given a spacecraft mass of approximately 2300 kg, the 22N thrusters set an upper acceleration limit of  $\sim 0.01 \text{ m/s}^2$  which is used in this study [5]. The servicer's attitude is prescribed to match the attitude of the target, ensuring docking faces remained aligned.

### 6.2.4.2 Station keeping results

While it is expected that the case of an asymmetrical target like the GOES-R spacecraft would experience significant electrostatic torques, it is possible for symmetric targets to experience



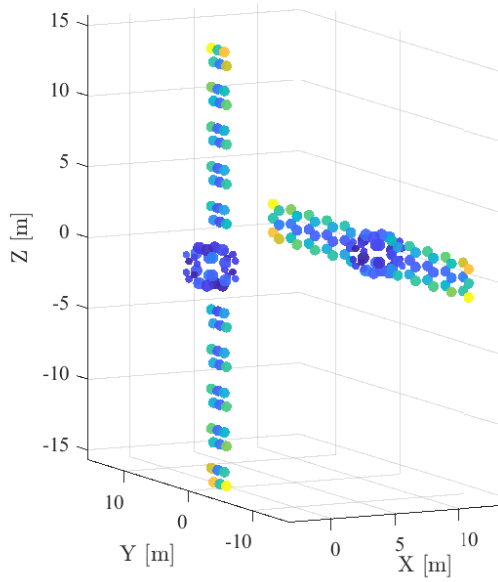
(a) Servicer (right) at a 10 meter hold point relative to the target (left), both craft at 0 kV.

(b) Servicer maintaining a 10 meter hold relative to the target for 5 hours, both craft at 10 kV. Only electrostatic perturbations acted on the target.

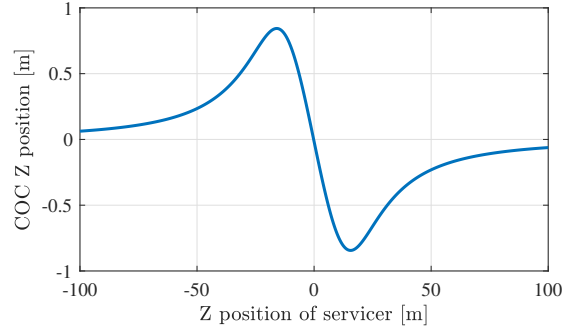
Figure 6.7: Results of servicer holding a fixed position relative to a target for a 5 hour hold, shown in the Hill frame. Electrostatic torques result in a significant tumble being imparted to the target, despite it having no initial rotation.

these perturbations as well. More generally, any case where the electrostatic force vector is not co-linear with the vector from the servicer center of charge (CoC) to the target center of mass (CoM) will result in a net torque on the target. Due to mutual elastance effects, as one charged body approaches another the center of charge location of each body will change. Figure 6.8b shows how the Z-position of the center of charge of a symmetrical spacecraft is impacted by the relative position of a nearby object. For this case, where both craft were held at 10 kV potentials, the center of charge position is shifted by up to  $\pm 85$  cm by induced capacitance effects of the nearby servicer.

A sweep of parameters is run to quantify the increase in control effort caused by the electrostatic perturbations for the hold case with an asymmetric GOES-R target. The target spacecraft was assumed to be inert, and the servicer required to maintain a fixed position relative to the target. The  $\Delta V$  required to hold a fixed position relative to the target when perturbed by only SRP



(a) Initial position of servicer (right) and two-panel target (left). Target is centered at the origin, servicer is offset by 10 m in the X direction.



(b) Change in Center of Charge (CoC) position of the target as a function of servicer location.

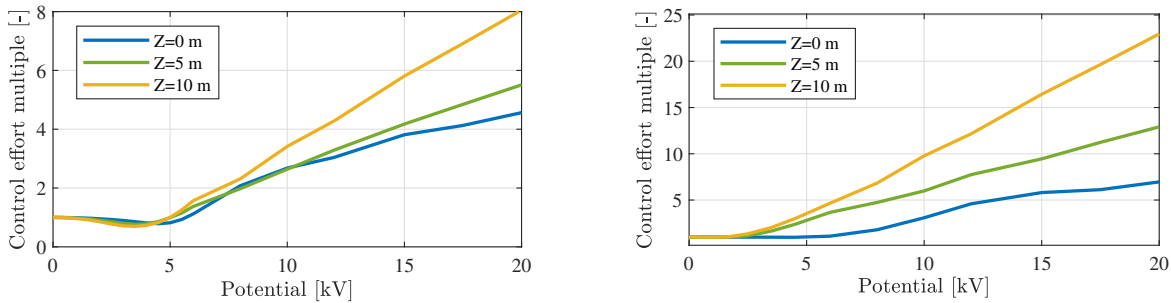
Figure 6.8: Variation in target parameters with changing servicer position.

is compared to the  $\Delta V$  requirement when both SRP and electrostatic perturbations are present. These simulations use the same  $x$ -offset for the hold point in the target frame (10 meters), but varied the  $\hat{z}$  position, from the target spacecraft docking location up to the top of the target's solar array. This allows evaluation of relative position on control effort, as moving the servicer center of charge further from the center of mass of the target will result in larger effective torques. This trend is seen in the resulting control effort increase with increasing  $\hat{z}$  position seen in Figure 6.9.

Even when the servicer is aligned with the two-panel target's docking port at  $z = 0$  meters, the torques generated by -10 kV potentials result in a control effort increase of over  $3\times$  the SRP-only perturbed case at 10 meters separation, while a hold level with the top of the solar array yields an increase of over  $10\times$  the unperturbed case. Additionally, the acceleration required by the servicer to maintain a position 10 meters away from the target at 10 kV reached approximately  $1 \text{ mm/s}^2$ , which could saturate the 1N thrusters used as part of the fine maneuvering system on

MEV-1 or a future servicing mission [5]. These numbers demonstrate that proximity operations can be significantly perturbed by electrostatic interactions.

Interestingly, there are combinations of potential and position which decrease the fuel consumption relative to the SRP-only perturbation case. This is a result of the electrostatic torques countering the SRP-induced torques, yielding reductions in final rotational rate of over 50% compared to the SRP-only case, and corresponding fuel savings of over 30% (Figure 6.9a).



(a) Control effort multiple with asymmetric GOES-R target. (b) Control effort multiple with symmetric two-panel target.

Figure 6.9: Increase in control effort (as a multiple of the  $\Delta V$  for the 0V, SRP-only case) required to hold a fixed 10 meter offset from the target for different servicer  $\hat{z}$  positions.

### 6.2.5 Servicer attitude control requirements

As the target tumbles, the servicer must both translate and rotate in order to maintain a fixed relative orientation. The attitude of the servicer is prescribed to match that of the target in this scenario, but the torque required to achieve this rotation is computed at each timestep by rearranging equation (6.2).

The inertia matrix is taken to be the same as the one estimated for the GOES-R spacecraft, as an estimate for a generic large GEO spacecraft. Figure 6.10 shows the torque required for the servicer to maintain its orientation relative to the target during the hold at different  $Z$  positions and potentials. Increasing the  $Z$  offset away from the target spacecraft centerline results in higher torque requirements for the servicer, as does increasing the potential of the spacecraft from 5 kV

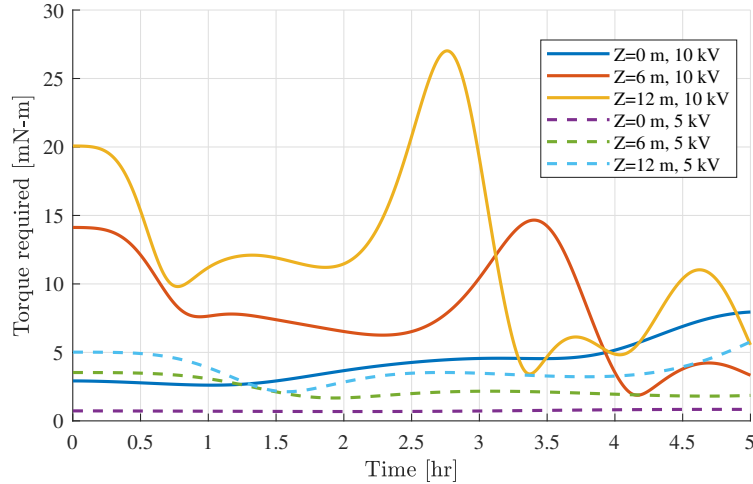


Figure 6.10: Torque required by servicer to maintain a relative orientation to the GOES-R target while holding a 10 meter offset position and 10 kV on each spacecraft.

to 10 kV. In both cases, these changes increase the torque acting on the target, so it is logical for the servicer to then require higher torque levels to maintain relative attitude. The highest required torque, for the  $Z = 12\text{m}$  and 10 kV potential case, is over 27 mN-m. Large reaction wheels, such as the Honeywell HR-12, are capable of generating torques of 100-200 mN-m, suggesting that these torques are significant but achievable [98]. The accumulated momentum in the reaction wheels as a result of these attitude maneuvers could present another limiting factor in control during charged proximity operations.

### 6.3 Rendezvous example

While it is clear that there are force and torque perturbations as a result of electrostatic interactions, it is less clear how much they might realistically matter in a rendezvous scenario where a relatively limited time is spent in close proximity to the target. To simulate this scenario, a nominal rendezvous trajectory is developed, based on public videos of the MEV-1 final trajectory. The servicer begins 80 meters from the target, and follows a straight trajectory to the interface point. Several holds are built in along the way, with 10 minutes each at 20 meters, 10 meters and 3 meters from the target. The terminal point is 1 meter from the docking location, at which point

physical grasping mechanisms take over during a final 30 minute hold.

A pre-computed reference trajectory (shown in Figure 6.2) is used here, and the controller tracks the reference as it evolves with time. The inherently coupled dynamics of the two spacecraft can increase the risk of collision as induced torques on the target spacecraft can result in collisions between antennas or arrays on the target and the servicer. In these cases it may only take a few degrees of target rotation to cause contact with the servicer.

The controller gains prioritize tracking accuracy as might be expected for the terminal rendezvous phase in an operational mission where positioning may be valued above fuel consumption concerns. These gains ( $[K_1] = 0.03 \cdot [I_{3 \times 3}]s^{-2}$  and  $[K_2] = 3 \cdot [I_{3 \times 3}]s^{-1}$ ) are selected to avoid saturating the controllers, but still enabling high precision rendezvous with a nominal fuel cost of 0.11 m/s when only gravitationally-induced relative motion perturbs the relative trajectory.

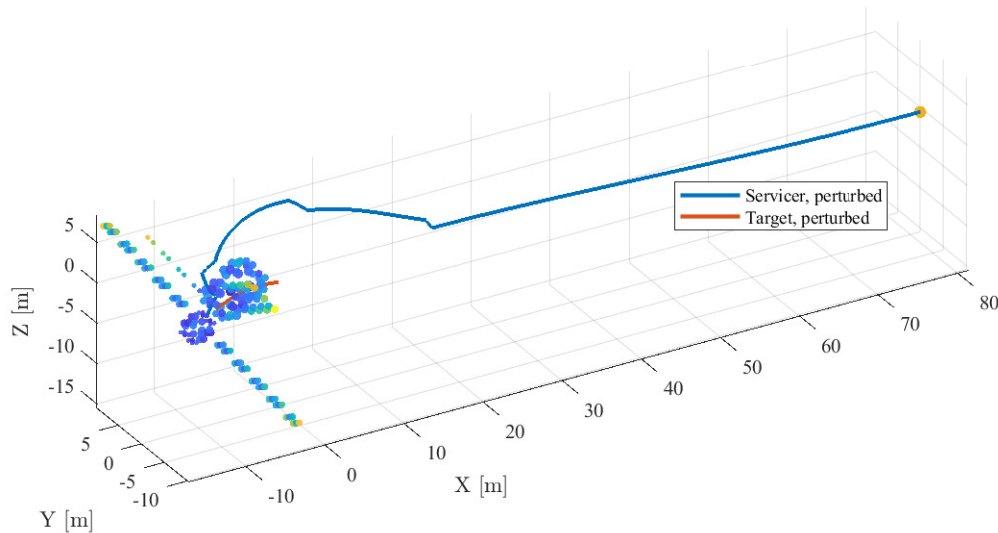


Figure 6.11: Perturbed rendezvous trajectory with -10 kV potential on each spacecraft.

Because the controller is forced to track a reference position which is accelerating in an inertial frame when the target begins to rotate, a steady state equilibrium is not possible and therefore performance with respect to steady state errors cannot be evaluated. However, for this rendezvous scenario, adding a -1 kV potential to each spacecraft results in a 80-fold increase in fuel

consumption (compared to a case with only gravitational accelerations), comparable to a worst-case SRP addition. The addition of -1 kV potentials to a case already perturbed by SRP can, as observed with the static hold cases, either increase or decrease control effort required for rendezvous by up to 10%.

Increasing the potential to just -5 kV results in over 30% increase in fuel consumption to maintain millimeter level errors in final position (relative to a worst-case SRP perturbation), and the target acquires rotational rates of  $0.03^\circ/\text{s}$  prior to rendezvous. Spacecraft potentials of -10 kV, seen in Figure 6.11, are still within the capability of the control system to maintain accurate positioning, with a worst case error of just over 3 cm, but at considerable fuel cost: over 9 m/s, or 125% increase over the max-SRP reference case and over  $90\times$  more than an unperturbed case. The target experiences more than a complete tumble during this rendezvous and final rotational rates of  $0.05^\circ/\text{s}$ . Finally, a near-record electrostatic charging level of -20 kV on each spacecraft results in a nearly 300-fold increase in control effort, worst-case positioning errors of 20 cm and final target rotational rates of  $0.2^\circ/\text{s}$ .

## 6.4 Conclusions

Ultimately, these results demonstrate that charging conditions which have been observed at GEO present significant perturbations to proximity operations, and should be modeled in rendezvous and proximity operations development. Perturbing torques between modeled spacecraft at 10 kV are shown to be an order of magnitude larger than SRP, and can dramatically increase the control effort required to perform proximity operations. These perturbing effects exist even when the potential between the spacecraft has been equalized, such as through the use of a plasma contactor (though the injection of plasma may introduce additional shielding effects between the spacecraft and should be further considered).

For some cases, such as a servicer which must inspect or repair a solar array, or a significantly asymmetric target object, it will be impossible to avoid imparting disturbing torques to the target. However, changing the attitude of the servicer on approach, or altering solar array orientations,

may help in minimizing these torques. Developing control and guidance strategies to feedforward on estimates of electrostatic potentials on each spacecraft to improve proximity operations perturbed by charging will be a goal of future work.

The examples presented here are not bounding cases, but instead serve to illustrate a possible scenario during a rendezvous which is not designed to account for electrostatic interactions. Worst case scenarios depend on the specific spacecraft geometries, approach trajectory and electrostatic potentials on each spacecraft. While electrostatic torques tend to increase fuel consumption and complicate rendezvous, in some cases the electrostatic torques can be helpful by balancing SRP torques, reducing overall fuel consumption and terminal rotational rate. This suggests appropriate selection of a rendezvous or proximity operation trajectory, and accurate knowledge of the potentials on both spacecraft are crucial to mitigating the impact of these perturbations, or could even use these perturbations to impart desired torques on the target.

## Chapter 7

### Constrained guidance for spacecraft proximity operations under electrostatic perturbations

#### 7.1 Motivation

Chapter 6 establishes that electrostatic force and torque perturbations are significant in a rendezvous scenario, leading to an obvious question: can the impacts of these perturbations be mitigated through trajectory design and remote potential sensing?

This chapter unifies these two areas—proximity operations and remote potential sensing by evaluating two guidance methods which seek to minimize the impact of electrostatic perturbations. The first method is a deterministic, sampling-based approach that computes desired relative position and attitude at each time step in a manner that is suitable for on-board implementation. The second method seeks a globally minimal rotational rate of the target at rendezvous through a pseudospectral collocation-based approach. This method is more computationally intensive and better suited for ground-based mission planning.

#### 7.2 Problem scenario

The scenario of interest in this chapter is shown in Figure 7.1. Like the scenario in Chapter 6, it involves a servicer approaching an inert target spacecraft where both spacecraft have accumulated significant electrostatic potentials as a result of interactions with the space environment. While significant (>kV level) charging events at geostationary orbit are relatively rare, occurring perhaps a few days per year on average, they can occur more frequently during periods of heightened solar

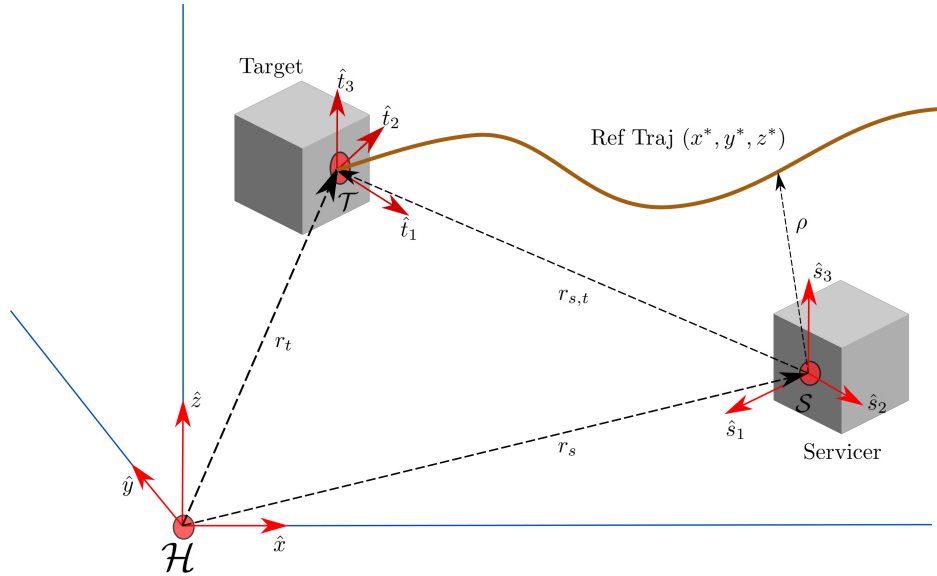


Figure 7.1: Reference frames for the proximity operations scenario.  $\mathcal{H}$  is the Hill frame, taken to be inertial for this scenario,  $\mathcal{S}$  is a frame fixed to the servicer and  $\mathcal{T}$  is fixed to the target's docking port.

activity [100]. Additionally, some components of spacecraft and debris objects may not be continuously conducting with the spacecraft frame, and may be composed of dielectric or other materials which experience charging differently than conducting metal structures. These components may be subject to significantly higher levels of charging than a fully conducting spacecraft structure, as ATS-6 observed dielectrics carrying 100x the electrostatic potential of the conducting spacecraft frame [118].

### 7.3 Dynamic sensitivity to estimated potential and range

The analysis here covers a two-craft rendezvous scenario in a geostationary graveyard orbit. It includes electrostatic perturbations, and solar radiation pressure (SRP) is also modeled as the other dominant perturbation in the GEO regime.

A few fundamental assumptions underpin the use of MSM here. First, the sphere radii and positions are derived from a finite element model of each spacecraft, taken as a ground truth. This truth model requires accurate models of the surface geometry of both spacecraft; through a

combination of a priori knowledge of the target and systems like LiDAR, this is readily achievable [123].

Next, the relative position and attitude of the spacecraft must be known to accurately compute the relative positions of each pair of spheres. Relative pose estimation remains an area of active research, but it is possible to obtain pose estimates of an uncooperative target with less than a degree of error using modern 3D flash LiDARs, stereo cameras or other techniques [119].

The electrostatic force  $F_{S,T}^e$  between charged bodies is computed through the MSM (Chapter 2), and torque is then computed as the cross product between the electrostatic force vector and the radius from the point of force application to the body center of mass. Torque computation therefore requires an accurate evaluation of the target body's center of mass. Furthermore, to predict the resultant rotational dynamics requires an accurate estimate of the target's inertia matrix. For a cooperative servicing target these values should be well documented, even in an end of life scenario. However, for a debris object these parameters may require estimation on-orbit by observing the rotational properties of the target. If the shape and potential of the target are known it is possible to use electrostatic interactions and proximity flight to deliberately introduce perturbing torques to the target, and the target's resulting rotational behavior then used to estimate its inertia parameters. The ability to apply a known external torque to a body may enable improvements in performance over previously proposed methods to estimate the inertia properties of tumbling bodies like those described by Reference [76].

Finally, the electrostatic potential of both the servicer and target must be known. The methods described in the previous chapters can achieve consistent target voltage estimates within 100 V or less. However, no work has yet been conducted to evaluate the potential estimation accuracy required for sufficiently accurate dynamic evaluations. In related work, Reference [68] explores the impact of erroneous total system charge product (the product of multiplying the charges on each spacecraft) on the closed-loop control stability characteristics of an actively charged Electrostatic Tractor debris tugging scenario. The authors find that the closed loop control can bifurcate and become unstable if charge is mis-estimated by just 40%, making it critical that an

accurate measure of electrostatic potentials be available.

While the electrostatic potential may be sensed remotely by the methods in Chapter 5, electrostatic charges are responsible for producing force and torque interactions between the bodies. The charge is related to the potential on a body by the body's capacitance, which is chiefly determined by the body's surface geometry.

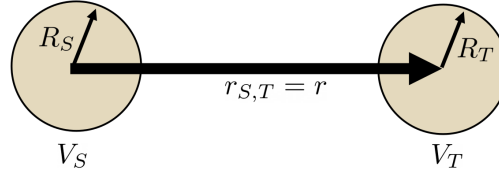


Figure 7.2: Illustration of two-sphere system evaluated.

A reduced-order analysis is developed to evaluate the sensitivity of the computed force and torque to the estimated electrostatic potential, and intercraft distance. To gain analytic insight into the sensitivity, each body is modeled as a single sphere, as seen in Figure 7.2, the simplest configuration which still enables the capture of mutual capacitance effects. An  $S$  subscript denotes a property of the servicer and a  $T$  the target. The force acting between the spheres is then found as

$$F = \frac{k_c q_S q_T}{r^2}. \quad (7.1)$$

where  $k_c$  is Coulomb's constant,  $q_s$  is the charge on the servicer,  $q_T$  is the target charge and  $r$  is the distance between the spheres.

Therefore, electrostatic charges on each sphere are calculated as a function of their potentials, computed as in Equation 2.9 and repeated here for convenience:

$$\begin{bmatrix} q_S \\ q_T \end{bmatrix} = \frac{r}{k_c (r^2 - R_S R_T)} \begin{bmatrix} r R_S & -R_S R_T \\ -R_S R_T & r R_T \end{bmatrix} \begin{bmatrix} V_S \\ V_T \end{bmatrix}. \quad (7.2)$$

The upper right and lower left elements of the capacitance matrix represent mutual capaci-

tance effects, caused by the interactions of the two bodies. These are expanded as

$$q_S = \frac{r}{k_c (r^2 - R_S R_T)} (r R_S V_S - R_S R_T V_T) \quad (7.3)$$

$$q_T = \frac{r}{k_c (r^2 - R_S R_T)} (r R_T V_T - R_S R_T V_S) \quad (7.4)$$

Combining this expansion with Equation 7.1 yields a force expression as

$$F = \left( \frac{r}{k_c (r^2 - R_S R_T)} \right)^2 ((r^2 + R_S R_T) V_S V_T - r R_S V_T^2 - r R_T V_S^2). \quad (7.5)$$

where the leading term is constant with respect to voltage.

However, in practice, the measured quantities are the potential of the servicer  $V_S$  and the relative potential of the target relative to the servicer  $\Delta V_{T,S}$ . Therefore

$$V_T = V_S + \Delta V_{T,S} \quad (7.6)$$

The force between the bodies then becomes

$$F = \left( \frac{r}{k_c (r^2 - R_S R_T)} \right)^2 ((r^2 + R_S R_T) V_S (V_S + \Delta V_{T,S}) - r R_S (V_S + \Delta V_{T,S})^2 - r R_T (V_S + \Delta V_{T,S})^2). \quad (7.7)$$

Typically, the effects of electrostatic interactions only become significant for cases where potentials exceed a few kV. While the sensitivity analysis provides a relative sensitivity, the methods used to remotely measure electrostatic potentials between spacecraft tend to be better characterized by an absolute uncertainty rather than a percentage. However, the typical  $1\sigma$  uncertainty in the measurements are in the range of 10-100 V, so expected errors for multi-kV targets are in the region of  $< 1 - 10\%$ . For a case with a 10% error in the relative potential estimate between the spacecraft, the resultant force estimation error is only about 8%, as seen in Figure 7.3, on the same order as the errors associated with the MSM formulation.

Common methods for measuring a spacecraft's own potential relative to the ambient plasma are limited in accuracy by the energy resolution of the instruments used, but can typically resolve spacecraft potentials to within  $< 5\%$  [132]. Because the remote potential sensing methods here

provide only relative potentials, the net error in a target's absolute potential will be a combination of errors in both the relative potential and a spacecraft's self-potential measurement.

The sensitivity of force to error in either the voltage of the servicer ( $V_S$ ) or the potential of the target relative to the servicer ( $\Delta V_{T,S}$ ) can be evaluated by taking the ratio of the partial derivatives of the electrostatic force with respect to  $V_S$  and  $\Delta V_{T,S}$ . The resultant ratio, seen in Equation 7.8, is a function of not just  $V_S, \Delta V_{T,S}$  but also of the problem geometry. The ratio of  $\partial F / \partial V_S / \partial F / \partial \Delta V_{T,S}$  is independent of the base voltage of each sphere; the ratio remains the same regardless of  $V_S, V_T$  as long as  $V_S = V_T$ .

$$\frac{\partial F / \partial V_S}{\partial F / \partial \Delta V_{T,S}} = \frac{(2V_S + \Delta V_{T,S})(r^2 + R_S R_T) - 2R_S V_S r - 2R_T r (V_S + \Delta V_{T,S})}{V_S (r^2 + R_S R_T) - 2R_T r (V_S + \Delta V_{T,S})} \quad (7.8)$$

Ultimately, the system, is far more sensitive to  $V_S$  than  $\Delta V_{T,S}$ . The exact value of the sensitivity ratio is a function of both voltages and the positions of each sphere, but is typically somewhere between 3 and 10 for most reasonable combinations of potentials and positions. Potentials on both spacecraft should be similar, as they are exposed to near-identical space environment conditions, but differences in construction and material properties may result in significant kV-level differences [118]. For a nominal case where each spacecraft is charged to 10 kV at 10 meter separation, Figure 7.3 illustrates the relationship between mis-estimated potentials on each sphere and the resultant force. As expected, the force error is significantly more affected by errors in  $V_S$  than  $V_T$ , with the relation nearly linear in this range. Nonlinearities in this relation become more pronounced as errors exceed 20%, but it is reasonable that this figure should account for most potential measurement uncertainties using existing techniques.

## 7.4 Control

### 7.4.1 System frames

Three coordinate frames are used, as shown in Figure 7.1. The Hill relative orbit frame,  $\mathcal{H}$  is assumed to be equivalent to an inertial frame for this scenario, and originates at a virtual Keplerian

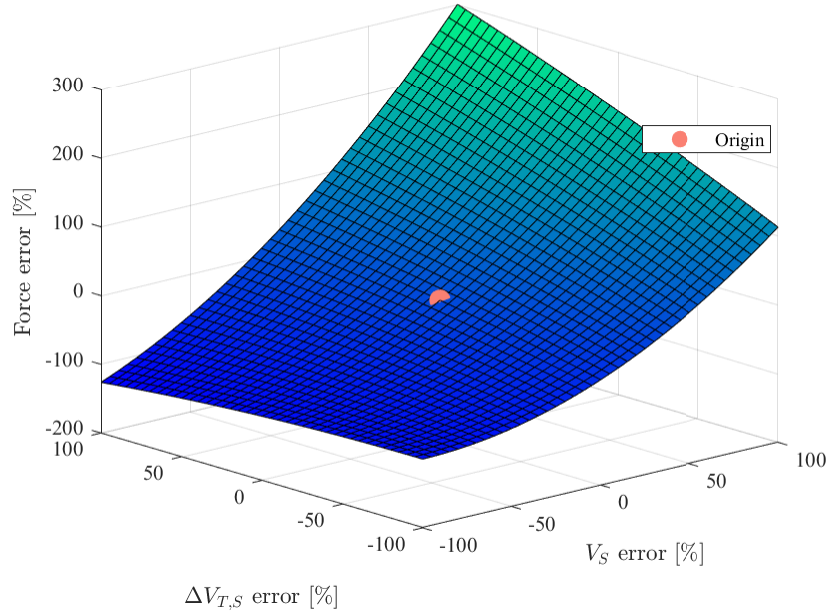


Figure 7.3: Sensitivity of electrostatic force to errors in  $\Delta V_{T,s}$  and  $V_S$ .

chief. The target frame,  $\mathcal{T}$  is co-located and co-aligned with the Hill frame at the beginning of the simulation. The target frame is fixed to the docking port on the target body. The servicer frame,  $\mathcal{S}$ , is fixed to the servicer docking port.

The reference trajectory is given by  ${}^{\mathcal{T}}\mathbf{r}^* = [x^*, y^*, z^*]^T$ , and right star superscripts are used to denote reference quantities. The reference is computed in the target frame, which aligns with a Hill-frame approach if no perturbations are present. However, if the target is rotating, the servicer will need maneuver in the Hill frame to track the reference trajectory in  $\mathcal{T}$ .

#### 7.4.2 Translational control

The goal of the control system is to track the reference trajectory by driving the position and velocity errors to zero. Error terms are given by

$$\boldsymbol{\rho} = \mathbf{r}_{S/T} - \mathbf{r}_{S/T}^* \quad (7.9)$$

$$\dot{\boldsymbol{\rho}} = \dot{\mathbf{r}}_{S/T} - \dot{\mathbf{r}}_{S/T}^* \quad (7.10)$$

as seen in Figure 7.1.

The system dynamics are inherently nonlinear due to the coupling of position, attitude and resultant force and torque. Therefore, a nonlinear Lyapunov-derived Cartesian feedback controller is implemented to track the desired reference trajectory computed by the guidance system, as [134]

The positive definite Lyapunov candidate function is chosen to be

$$V(\boldsymbol{\rho}, \dot{\boldsymbol{\rho}}) = 1/2[K_1]\boldsymbol{\rho}^T \boldsymbol{\rho} + 1/2\dot{\boldsymbol{\rho}}^T \dot{\boldsymbol{\rho}} \quad (7.11)$$

The derivative of  $V(\boldsymbol{\rho}, \dot{\boldsymbol{\rho}})$  is then

$$\dot{V}(\boldsymbol{\rho}, \dot{\boldsymbol{\rho}}) = \dot{\boldsymbol{\rho}}^T (\mathbf{u}_s + (\ddot{\mathbf{r}}_{S,T} - \ddot{\mathbf{r}}_{S,T}^*) + [K_1]\boldsymbol{\rho}) \quad (7.12)$$

which takes the negative semidefinite form

$$\dot{V}(\boldsymbol{\rho}, \dot{\boldsymbol{\rho}}) = -\dot{\boldsymbol{\rho}}^T [K_2]\dot{\boldsymbol{\rho}} \quad (7.13)$$

for the control input

$$\mathbf{u}_s = -\ddot{\boldsymbol{\eta}} - [K_1]\boldsymbol{\rho} - [K_2]\dot{\boldsymbol{\rho}}. \quad (7.14)$$

and positive definite matrices for the control gains  $[K_1], [K_2]$ . Here the term  $\ddot{\boldsymbol{\eta}}$  represents  $(\ddot{\mathbf{r}}_{S,T} - \ddot{\mathbf{r}}_{S,T}^*)$ , the relative Hill-frame acceleration between the reference in  $\mathcal{T}$  and  $\mathcal{H}$  as a result of differential gravitational accelerations and the rotation of the target body with respect to  $\mathcal{H}$ . It is assumed that the target body's rotational rates and pose are known, likely through a combination of image-based and LiDAR-based methods. By feeding forward on these known relative accelerations, the servicer achieves better tracking and convergence at lower control effort cost.

As the target body rotates, the reference position will accelerate relative to the Hill frame. The Hill frame is assumed equivalent to an inertial reference frame. This acceleration is computed as

$$\ddot{\mathbf{r}}_{T/S} = \mathbf{r}_{T/S}'' + \dot{\boldsymbol{\omega}}_{T/H} \times \mathbf{r} + 2\boldsymbol{\omega}_{T/H} \times \mathbf{r}'_{T/S} + \boldsymbol{\omega}_{T/H} \times (\boldsymbol{\omega}_{T/H} \times \mathbf{r}_{T/S}) \quad (7.15)$$

where the prime right superscript denotes a target-frame derivative, and dots a Hill-frame derivative.

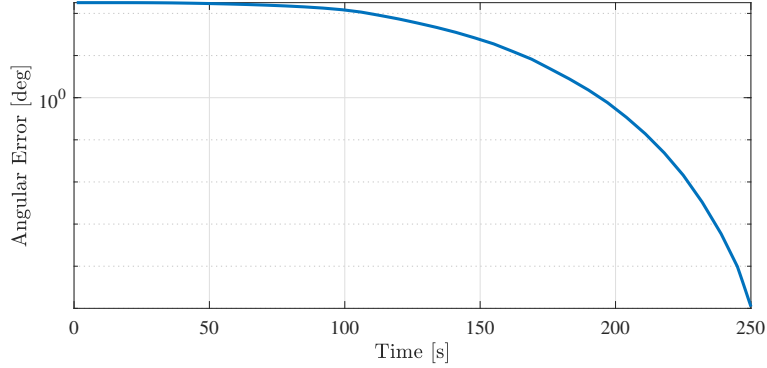


Figure 7.4: Servicer attitude error during a 180° slew maneuver.

### 7.4.3 Attitude control

The attitude of the servicer must follow a time-varying reference to maintain a line of sight vector between the servicer’s relative navigation sensors and the docking point on the target. The goal of the attitude controller is therefore to track the target’s rotation such that the navigation system is always aligned to the docking port.

The attitude controller acts independently of the translation controller, and like the translation controller, has a maximum control effector limit but no minimum. This correlates well to an attitude control system reliant on momentum exchange devices like reaction wheels or control moment gyroscopes, while a reaction control system or other thruster-based method is used to apply translational control. The torque control limit is set to 100 mN-m, feasible for large reaction wheels like the Honeywell HR-12 series [98].

The attitude controller feeds back on the spacecraft attitude quaternion, and is given by Reference [134] as

$$\mathbf{T}_s = -K\boldsymbol{\epsilon}_{S/T} - P\delta\boldsymbol{\omega}_{S/T} + [I](\dot{\boldsymbol{\omega}}_{s^*} - [\tilde{\boldsymbol{\omega}}]\boldsymbol{\omega}_{s^*}) + [\tilde{\boldsymbol{\omega}}_{s^*}][I]\boldsymbol{\omega} - \mathbf{L}_{\text{ext}}. \quad (7.16)$$

where

$$\mathbf{L}_{B,\text{ext}} = \mathbf{L}_{B,\text{SRP}} + \mathbf{L}_{B,\text{electro}} \quad (7.17)$$

and  $\epsilon_{S/T}$  is the 3 element vector component of the quaternion attitude error  $\beta_{S/T}$ .

$$\epsilon = \beta_{S/T}(1 : 3) = [\beta_1, \beta_2, \beta_3]^T \quad (7.18)$$

$\mathbf{L}_{\text{ext}}$  is the external torque acting on the servicer as a result of SRP and electrostatic interactions.  $\mathbf{T}_s$  is the control torque commanded by the servicer, and gains are  $K = 0.01[I]_{3 \times 3}$ ,  $P = 0.001[I]_{3 \times 3}$ . Convergence of this controller is shown in Figure 7.4. The inertia matrix used for numerical simulations is that from equation (2.13), repeated here for convenience:

$$[I] = \begin{bmatrix} 15597 & -335.17 & 7070 \\ -335.17 & 23277 & -188.63 \\ 7070 & -188.63 & 23407 \end{bmatrix} \text{ kg-m}^2. \quad (7.19)$$

The servicer spacecraft's translation and rotational control are assumed to be independent, such that it can always command a Hill-frame force up to the maximum threshold (equivalent to 0.01 m/s<sup>2</sup> acceleration).

## 7.5 Guidance

Prior studies into the topic of spacecraft proximity operations guidance under perturbations often focus on optimal control strategies to develop trajectories which minimize risk and fuel consumption [96].

These methods are typically computationally intensive, particularly when applied to systems with significant constraints and complex dynamics, and may require reference trajectories to be computed a priori on the ground, while a controller or neighboring optimal solution follows the trajectory on board the spacecraft [96].

This is often problematic in the case of electrostatic perturbations, which may vary significantly over a several hour rendezvous process as spacecraft move through changing local plasma environments or lighting conditions. This can cause dramatic changes in the relative motion dynamics between the two bodies, necessitating costly re-optimization [102].

As discussed in Chapter 2, it is very difficult to accurately predict the potential on a spacecraft, as this prediction is highly sensitive to space weather conditions. Therefore, global optimization of a multi-hour rendezvous requires some assumption of the environment. Alternatively, given the uncertain future system dynamics, the servicer could compute the optimal approach vector at that timestep, and re-evaluate the desired approach as new measurements of target and servicer potential are available. The solution introduced here follows this second strategy, relying on a sampling-based approach. A reduced-order MSM model is used to compute position and attitudes which most closely meet a desired torque, trading a small degree of accuracy for decreases in computational burden. The approach trajectory illustrated here defines the servicer position and attitude relative to the target at each time step, providing 6 DOF inputs to the controller.

### 7.5.1 Deterministic translational guidance

Several constraints are imposed on the approach trajectory. The nominal unperturbed trajectory is shown in Figure 7.7, and is shown in the target frame  $\mathcal{T}$ . For a non-rotating target case, this corresponds to the Hill frame approach. The position and velocity for this approach are shown in Figure 7.8. The trajectory is initialized at an 80 meter range, a point where remote electrostatic potential measurements are expected to be available. The servicer is required to perform 3 hold maneuvers at 10 meters, 5 meters and 1 meter from the docking point. The first two are set for ten minutes, to allow ground controllers to verify navigation solutions or similar, while the final hold is commanded for 30 minutes to allow for robotic arms to perform grappling maneuvers. Hyperbolic tangent functions are used to smooth the approach trajectory to avoid acceleration singularities as seen in Figure 7.8.

Repulsive electrostatic forces between the target and the servicer result in the target translating relative to the servicer and the servicer having to accelerate to pursue it, these accelerations are very small, on the order of  $10^{-7}$  m/s<sup>2</sup>. By comparison, torques result in rotational rates on the order of 0.1°/s, which results in translational acceleration of the reference frame relative to the Hill frame, which a servicer at 10 meters distance must then chase with accelerations on the

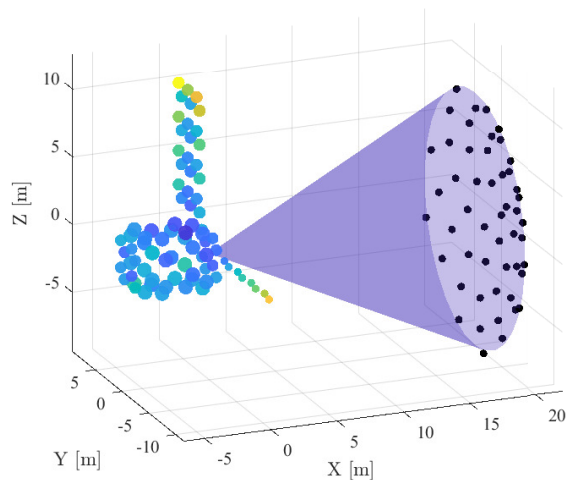


Figure 7.5: Constraint cone fixed to target docking port, and selected test positions at a fixed distance to the target port.

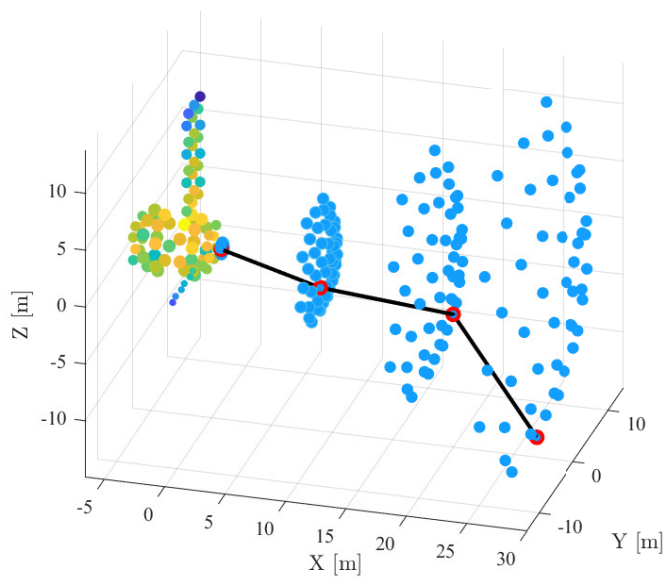


Figure 7.6: Conceptual illustration of four updates of iterative guidance strategy. Best solution at each time step shown in red, black line represents the servicer trajectory between each pair of points.

order of  $10^{-4}$  m/s<sup>2</sup> or greater. Electrostatic torques are therefore a much more significant perturbation than electrostatic forces, and minimizing the impact of these torques on an inert target could dramatically reduce the overall control effort required for proximity operation.

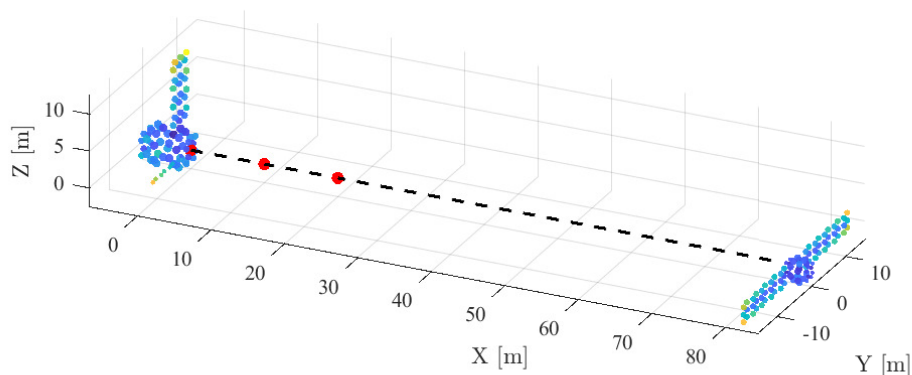


Figure 7.7: The nominal approach trajectory from the two-panel servicer to the one panel target at the origin. Hold points are shown in red.

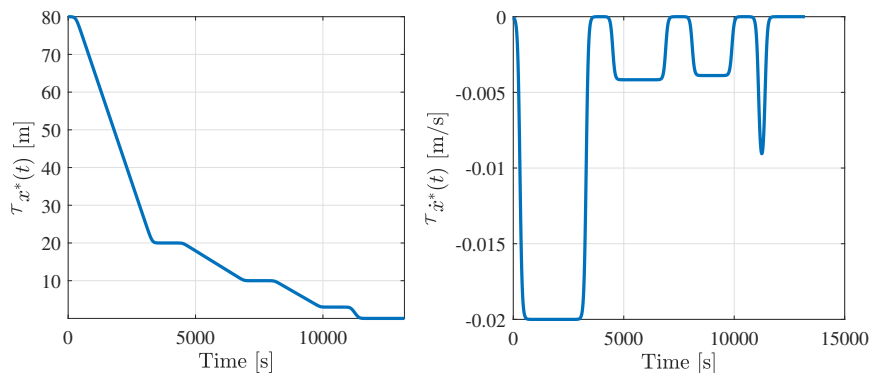


Figure 7.8: Position and velocity of the target-frame desired rendezvous trajectory.

The final phase of autonomous rendezvous is highly dependent on an accurate navigation solution, typically obtained by a combination of LiDAR and visual or IR cameras. These impose line of sight constraints on the approach trajectory; not only does the servicer need to stay within a constraint cone of the docking point to allow satisfactory navigation sensor visibility, but the

attitude of the servicer must also be constrained such that the RPO sensors have a direct line of sight to the docking location. For this work an approach cone with a  $25^\circ$  half angle is chosen, on a similar level to the approach angle observed in publicly available videos of the MEV-1 rendezvous operation. Despite being a relatively tight approach cone, there is significant variation in the magnitude and direction of electrostatic torques acting on the target in this area. Figure 7.9 illustrates an example of the torques imparted to a GOES-R target with a servicer at 10 meters distance, 10 kV on each spacecraft; methodology for this figure is described in Chapter 6. Within the  $25^\circ$  approach cone there is a difference of over an order of magnitude between the lowest torque point ( $< 0.2$  mN-m) and the highest ( $> 2.3$  mN-m).

Due the relatively small region admissible under the constraints, a sampling-based strategy can efficiently evaluate the search space. The guidance strategy implemented here evaluates the electrostatic interactions between low-fidelity MSM models (20 sphere) of both spacecraft at 50 points over the  $25^\circ$  approach cone, with a fixed distance to the docking location as seen in Figure 7.5. At each guidance update a new approach vector is computed based on the evaluation of the torque vector on the target, as seen in Figure 7.6. The torque vector quantity acting on the target closest to a desired quantity is selected at each step. The servicer then follows a linear reference trajectory until the next guidance update.

The position of each sample point is selected based on a spherical spiral to achieve near evenly spaced points. The number of points to sample is chosen by evaluating the variation in electrostatic torques over the constraint cone, and then selecting a sample density that captures relatively small scale variations in torque. In this case, the sensitivity of torque with respect to angle seen in Figure 7.9 led to a 50 point sample, which ensures the minimum torque is within 0.1 mN-m of the minimum sampled point for these spacecraft models. By constraining the distance to the target to be constant, this reduces to a constrained two dimensional (in azimuth and elevation angle) search space, where the  $L_2$  norm of the angles must be less than  $25^\circ$ .

The electrostatic forces and torques acting between the bodies are a function of the relative position of every sphere on each body, so both the target's attitude and position state need to

be prescribed by the guidance algorithm at each timestep. The RPO sensors must maintain a line of sight to the docking point, so the servicer must orient itself accordingly. However, this only constrains two degrees of rotational freedom for the servicer, which is free to rotate about the line of sight. As seen in Figure 7.10, there are significant differences in torque as a servicer rotates through the one unconstrained degree of freedom. For this case, the maximum torque magnitude is over 20% higher than the minimum, which could have significant implications over a multi-hour proximity operation. Therefore, 50 attitudes are evaluated at each position, to find the combination of position and attitude which come closest to satisfying a desired torque as possible while maintaining a reasonable computational burden.

Evaluating the intercraft forces and torques over 50 attitudes at 50 positions requires less than 0.1 second using Matlab on a modern laptop computer; significant performance gains could be realized by moving to a language commonly used for flight software development like C. Using a higher fidelity model with four times more spheres per vehicle results in computation times increasing by a factor of  $6\times$ , with little change in the best position/attitude combination found.

The electrostatic potentials and inter-craft forces will evolve over time periods on the order of minutes to tens of minutes, depending on separation distances and closure rates, so relatively slow updates of the guidance algorithm are acceptable for the system dynamics. The desired approach vector and attitude combination can be computed infrequently, making this solution well suited to implementation on board a servicing spacecraft. However, the MSM formulation tested here is sufficiently fast that it could be implemented on-board a spacecraft with updates on the order of seconds or faster if desired.

### 7.5.2 Deterministic attitude guidance

The servicer attitude is prescribed to orient the sensors towards the docking point, computing the required quaternion between the sensor line of sight vector  $\hat{\mathbf{s}}$  and the relative  $\mathcal{T}$ -frame position of the servicer  $\mathbf{r}_{S/T}$  as

$$\hat{\mathbf{e}} = \frac{\mathbf{r}_{S/T}}{|\mathbf{r}_{S/T}|} \times \hat{\mathbf{s}} \quad (7.20)$$

$$\phi = \cos^{-1} \left( \frac{\mathbf{r}_{S/T} \cdot \hat{\mathbf{s}}}{|\mathbf{r}_{S/T}| |\hat{\mathbf{s}}|} \right) \quad (7.21)$$

$$\boldsymbol{\beta}_{S/T} = [\cos(\phi/2) \quad \hat{\mathbf{e}} \sin(\phi/2)]^T \quad (7.22)$$

This approach constrains two rotational degrees of freedom for the servicer, but does not constrain the about-boresight rotation.

While only representing one degree of freedom, there are significant differences in the torque vector exerted on the target at different servicer attitudes. For the example position shown in Figure 7.10, rotating the servicer about the line of sight axis results in changes in the total torque magnitude of over 30%. In addition, the direction of the torque vector can change by over 70° by varying servicer orientations at a specific position.

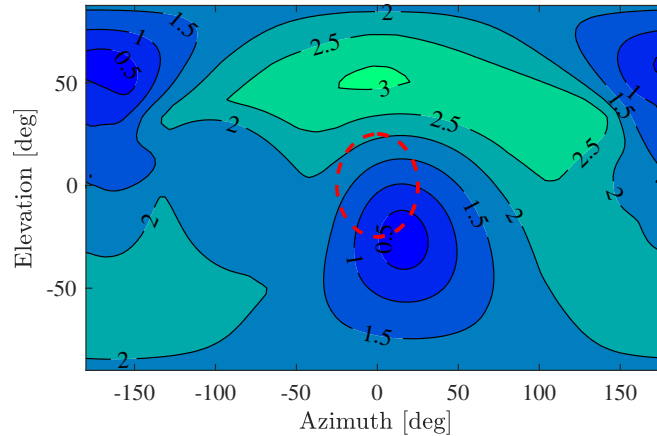


Figure 7.9: Torque acting on a GOES-R target due to electrostatic interactions at a 10 meter distance as a function of azimuth and elevation. Circled region corresponds to a 25° approach cone.

For cases where there is < 1% difference in electrostatic torque between different orientations, the servicer attitude is chosen to maximize the distance between the closest points on the two spacecraft in an effort to minimize the probability of a collision between the craft.

Additionally, there are cases where exerting a specific electrostatic torque vector on the target are desirable. These scenarios involve rendezvous with a tumbling target, when electrostatic forces

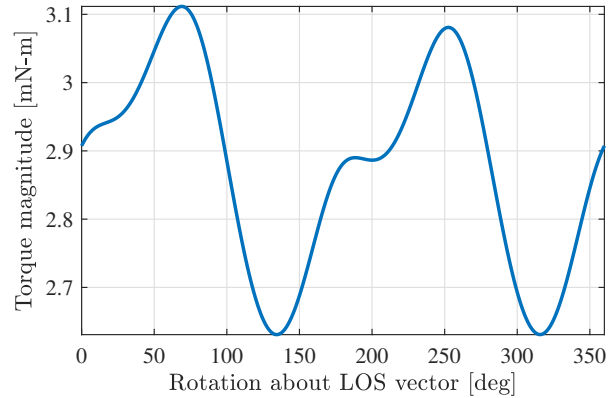


Figure 7.10: Electrostatic torque imparted to the target as a function of servicer attitude, where the servicer is only rotated about the line of sight (LOS) vector.

reduce the rotational rate of the target prior to grappling, or cases where a cooperative client transitions into a free-drift mode prior to docking and perturbing effects like SRP are negated by electrostatic interactions.

### 7.5.3 Simulation results

A rendezvous scenario is simulated with a notional GEO spacecraft and servicer, as described in Chapter 6. Mass and inertia properties for the target and servicer are taken to be known exactly in the controller and dynamics propagation.

SRP is added as an unmodeled disturbance for the target body, using the non-shadowing model discussed previously. For the GOES-R target, the single asymmetric solar array leads to average SRP induced torques of approximately 0.5 mN-m across all orientations. For comparison, electrostatic torques at 10 meters exceed this level when just 1900 V are applied to each spacecraft.

Figure 7.11 illustrates a straight line rendezvous perturbed by electrostatic interactions, using a guidance policy that does not account for those electrostatic perturbations. The dashed line illustrates the trajectory unperturbed by electrostatics. Qualitatively, the approach shown in Figure 7.12 experiences far less perturbation from the nominal, straight line trajectory shown in Figure 7.11. These simulations are performed with 80 sphere models for the target and 92 spheres for the

servicer, and 10 kV potentials on each. This is a severe charging event only relatively infrequently at GEO, but is reasonable to anticipate in a spacecraft lifetime [116]. This scenario therefore offers a plausible instance of significant electrostatic perturbations due to space weather interactions.

Selecting an approach angle to minimize the electrostatic torque acting on the target during rendezvous results in a greater than 60% decrease in control effort required for rendezvous, and decreases in target rotational rate of over 50%, from  $0.025^\circ/s$  to less than  $0.01^\circ/s$ .

These improvements result in improved docking accuracy, reduced navigation uncertainty and more predictable lighting conditions. These improvements occur despite not accounting for significant SRP torques in the model. Steady lighting conditions are particularly important in improving optical navigation accuracy during the final meters of rendezvous, when small errors could result in undesired contact between the spacecraft.

For this analysis both spacecraft are assumed to be at fixed potentials, with electrostatic potentials constant over the entire spacecraft surface. This is in adherence with modern guidelines for spacecraft design, which recommend that all surfaces be continuously conducting and commonly grounded to the spacecraft frame to mitigate arcing hazards. However, this is not an accurate assumption in all cases; older spacecraft were frequently nonconducting, which can result in different components on the structure having potential differences of hundreds or even thousands of volts due to varying material properties and solar photon exposure [132, 118]. Inclusion of differential charging effects and the assessment of their impact in proximity operations is an area for future work, and could be augmented by the approach presented in Reference [71] for incorporating non-conductive structures into an MSM framework.

Given the attitude, position and approach angle constraints imposed on the servicer, only a limited subset of potential locations are admissible. While the sampling-based method used here may only find a sub optimal local minimum of the electrostatic torque, it is generally within  $< 10\%$  of an absolute minimum torque. This limits the improvements in performance possible through the use of more computationally intensive optimal control strategies. While it is expected that the servicer should be able to determine its own attitude with high precision, uncertainty in target

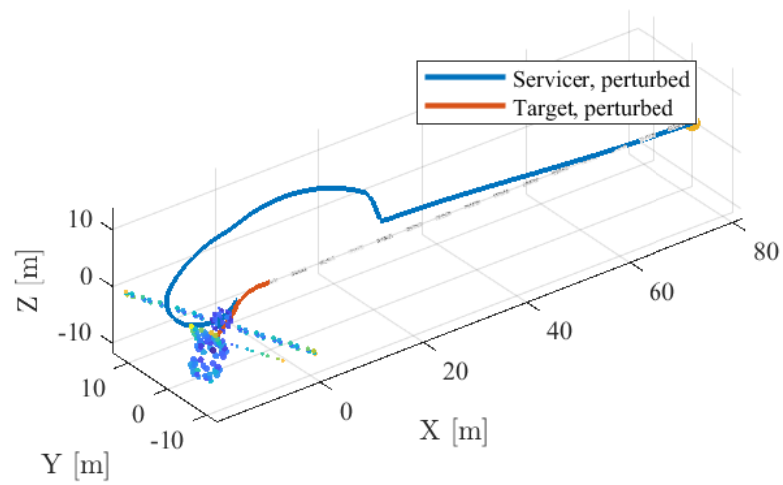


Figure 7.11: Rendezvous trajectory perturbed by 10 kV electrostatic potential on each spacecraft, with no guidance accounting for electrostatic interactions.

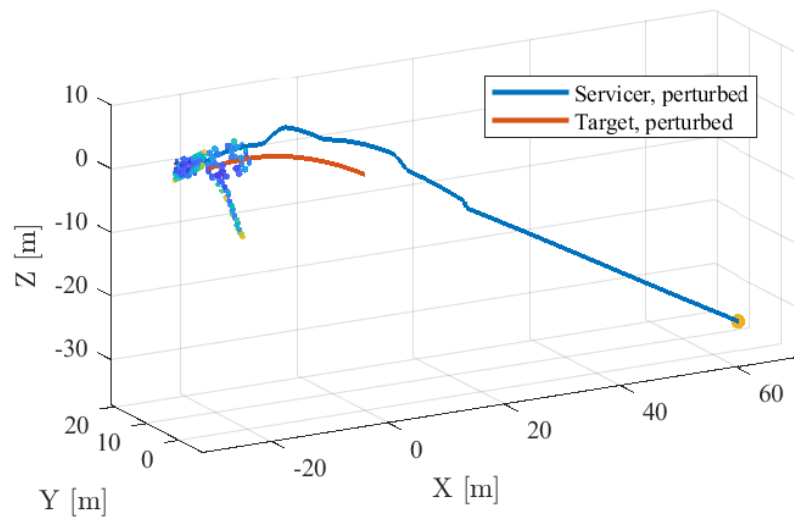


Figure 7.12: Rendezvous trajectory perturbed by 10kV electrostatic potential on each spacecraft, with guidance accounting for electrostatic interactions.

relative pose estimation can drive significant mis-calculation of the electrostatic torques between the craft. Taking the gradient of the data shown in Figure 7.9 allows the sensitivity of torque to the attitude of the target to be determined. The gradient of torque with respect to attitude is shown in Figure 7.13. Some regions in Figure 7.13 exhibit sensitivities over 0.03 mN-m/degree, so just a few degrees of error in target attitude estimates can result in significant errors in computed electrostatic torque.

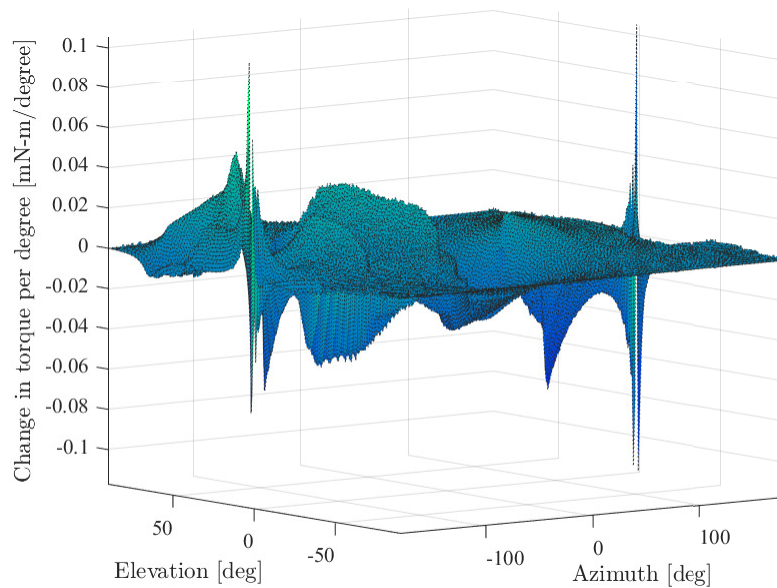


Figure 7.13: Sensitivity of  $L_{T,\text{electro}}$  to target attitude estimation errors

## 7.6 Optimized guidance approach

The sampling-based guidance approach offers significant improvements in final rotational rate, further improvements are obtained by globally optimizing a trajectory to minimize the rate. The sampling-based approach minimizes the net torque parameter at each successive interval, but a superposition of local minima at discrete timesteps is not equivalent to a global optimization across the full reference trajectory.

While a wide range of techniques are available for trajectory optimization, a method based on

pseudospectral collocation is utilized here. Rather than parameterize the control effort, as is often done in optimal control collocation problems, the target-frame trajectory of the servicer is used. A polynomial function is selected to prescribe the reference trajectory, as it guarantees satisfaction of initial and final position/velocity constraints.

### 7.6.1 Trajectory parameterization

This trajectory is parameterized in the  $\mathcal{T}\hat{y}$  and  $\mathcal{T}\hat{z}$  directions seen in Figure 7.7. The  $\mathcal{T}\hat{x}$  direction follows the nominal reference trajectory in Figure 7.7, which preserves the hold points. Additionally, the initial positions and velocities are fixed for all directions, beginning at [80 0 0]m with no initial velocity. The simulation period is fixed at 3.5 hours, as in the nominal case. At this final time the trajectory is constrained to reach a position of [1 0 0]m, with no relative velocity.

Additionally, a soft constraint is imposed through a linearly increasing penalty term to ensure the servicer remains within the approach constraint cone. Smoothly approaching the final state additionally imposes the terminal approach constraint

$$\left. \frac{dy^*}{dx^*} \right|_{x^*=0} = \left. \frac{dz^*}{dx^*} \right|_{x^*=0} = 0. \quad (7.23)$$

Differentiating the trajectory prescribing polynomial once provides the velocity at each point in time, while the second derivative provides accelerations. To ensure that the maximum acceleration magnitude is within the control authority bounds set, the second derivative of the position is constrained to fall within the actuation limits.

The hard constraints the optimized trajectory must meet therefore consist of initial position  $Y(X(t_o))$ , final position  $Y(X(t_f))$ , initial velocity  $\dot{Y}(X(t_o))$ , and final velocity  $\dot{Y}(X(t_f))$ . Because the trajectory is parameterized in the  $\mathcal{T}y$  and  $\mathcal{T}z$  directions as a function of the  $\mathcal{T}x$  reference position  $x^*$ , the value of  $x^*$  is normalized to improve numerical conditioning for the polynomial trajectory as

$$\chi = \frac{x^*}{x^*(t_o)}. \quad (7.24)$$

This set of initial/final states and rates provides 4 constraints, so a 3<sup>rd</sup> order polynomial

with 4 total terms could fit these constraints perfectly. However, this would provide no variables to tune in the optimization, and consequently could exceed acceleration limits or other imposed constraints. A solution is therefore to use a 5<sup>th</sup> order polynomial, as

$$y^*(\chi) = \alpha_1\chi^5 + \alpha_2\chi^4 + \alpha_3\chi^3 + \alpha_4\chi^2 + \alpha_5\chi + \alpha_6 \quad (7.25)$$

$$z^*(\chi) = \beta_1\chi^5 + \beta_2\chi^4 + \beta_3\chi^3 + \beta_4\chi^2 + \beta_5\chi + \beta_6 \quad (7.26)$$

where  $\chi$  is the non-dimensional independent variable and  $\alpha_i$  represents the coefficients on each term. This formulation for  $y^*(\chi)$  and  $z^*(\chi)$  provides 6 total coefficients to determine in  $\boldsymbol{\alpha}$  and  $\boldsymbol{\beta}$ , so a state vector is compiled as

$$\boldsymbol{\kappa}_{y^*} = \begin{bmatrix} y_0 & y_f & \dot{y}_0 & \dot{y}_f & \ddot{y}_0 & \ddot{y}_f \end{bmatrix}^T \quad (7.27)$$

The acceleration terms  $\ddot{y}_0, \ddot{y}_f$  are treated as tuning parameters, and the set of coefficients  $\boldsymbol{\alpha}$  is computed to meet these constraints as

$$\boldsymbol{\alpha} = [M]^{-1}\boldsymbol{\kappa}_{y^*} \quad (7.28)$$

where

$$[M] = \begin{bmatrix} 0 & 0 & 0 & 0 & 0 & 1 \\ 1 & 1 & 1 & 1 & 1 & 1 \\ 0 & 0 & 0 & 0 & 1 & 0 \\ 5 & 4 & 3 & 2 & 1 & 0 \\ 0 & 0 & 0 & 2 & 0 & 0 \\ 20 & 12 & 6 & 2 & 0 & 0 \end{bmatrix} \quad (7.29)$$

Analogously, the  $\boldsymbol{\beta}$  coefficients are computed as

$$\boldsymbol{\beta} = [M]^{-1}\boldsymbol{\kappa}_{z^*}. \quad (7.30)$$

The  $[M]$  matrix is equivalent for any 5<sup>th</sup> order polynomial, and is also used for the  $z^*$  and  $\theta_1^*$  reference trajectory components.

Therefore, this approach allows the creation of trajectories that meet 4 constraints precisely, and 2 bounded parameters that are tuned through the optimization.

Trajectories can be optimized to any number of variables and cost functions, but the primary objective in this case is to minimize the final rotational rate of the target object. A state vector is generated by the optimizer, using the 4 prescribed and 2 tuned parameters, and the resultant polynomial coefficient vector  $\alpha$  computed. This process is done independently for the  ${}^T\hat{y}, {}^T\hat{z}$  and  $\hat{\theta}_1$  directions. The prescribed trajectory is then used as a reference trajectory input into the reference tracking controller, and the final rotational rate of the target assessed. The optimization is performed to minimize the cost function

$$\mathcal{J} = \omega_f^T \omega_f \quad (7.31)$$

where  $\omega_f^T$  is the angular velocity of the target body at the end of the simulation.

This approach, preserving initial conditions and driving final states/rates to zero, is generalized to a polynomial of arbitrary degree  $n$  to describe  $y^*(\chi)$  and  $z^*(\chi)$  as

$$y^*(\chi) = \alpha_2\chi^2 + \alpha_3\chi^3 + \sum_{j=1}^n \alpha_{(j+3)}\chi^{(j+3)} \quad (7.32)$$

$$z^*(\chi) = \beta_2\chi^2 + \beta_3\chi^3 + \sum_{j=1}^n \beta_{(j+3)}\chi^{(j+3)} \quad (7.33)$$

where the 2<sup>nd</sup> and 3<sup>rd</sup> coefficients are related to the initial states for  $y^*$  as

$$\begin{bmatrix} \chi_i^2 & \chi_i^3 \\ 2\chi_i & 3\chi_i^2 \end{bmatrix} \begin{bmatrix} \alpha_2 \\ \alpha_3 \end{bmatrix} = \begin{bmatrix} y_0^* - \sum_{j=1}^n \left\{ \alpha_{(j+3)} \chi_i^{(j+3)} \right\} \\ \frac{V_{y,i}}{V_{x,i}} x_0^* - \sum_{j=1}^n \left\{ (j+3) \alpha_{(j+3)} \chi_i^{(j+2)} \right\} \end{bmatrix} \quad (7.34)$$

As discussed previously, the servicer attitude is constrained to maintain a line of sight to the target docking port. However this is an under-constrained problem, leaving the servicer attitude free to rotate about the line of sight vector. An additional polynomial is used to prescribe the rotation about this vector as a function of the  $X$  position, developed analogously to the trajectories in  $\hat{y}, \hat{z}$  as

$$\theta_1(\chi) = \gamma_1\chi^5 + \gamma_2\chi^4 + \gamma_3\chi^3 + \gamma_4\chi^2 + \gamma_5\chi + \gamma_6 \quad (7.35)$$

A quintic polynomial is found to perform well in prescribing both translation and rotational positions, with little improvement offered by higher order polynomials for this rendezvous scenario. Higher orders allow better fitting and more optimal solutions in cases with initially rotating target bodies, however.

Final rotational rate is strongly dependent on the inertia properties of the target vehicle, so a proxy measure of minimizing the torque imparted on the target over the rendezvous trajectory is preferable if center of mass location is more accurately known. Torque acting on the uncooperative target for this scenario is only a function of spacecraft relative pose and target center of mass location, sun angle and electrostatic potentials, decreasing the target parameters that need to be determined.

The inertia and mass properties are likely to be the most poorly defined aspect of the target, as spacecraft at end of life typically have some (uncertain) quantity of residual fuel remaining. Additionally, in a servicing or debris remediation mission where the spacecraft may have broken up to some extent, a priori knowledge of the inertia properties is highly uncertain [76].

Optimization of this trajectory is performed using Matlab's `fminsearch` unconstrained optimization function. This method resulted in a final target rotational rate of just  $0.006^\circ$  when subject to 10 kV potential levels and SRP, as seen in Figure 7.15.

These results present a significant improvement in final rotational rate over the sampling-based algorithm, but at dramatically increased computational cost. While the sampling-based approach could compute a desired approach vector and attitude in  $\sim 0.1$  seconds, the `fminsearch` optimizer required  $\sim 10^4$  times longer and thousands of iterations to converge, with each requiring integration for a full trajectory. Such high computation times occurred despite having just 6 total tuning parameters. Increasing the search space with higher fidelity polynomials comes with an accompanying increase in computational time. Therefore, although the sampling approach provides a sub-optimal solution to the trajectory, it has benefits in computational burden, enabling on-orbit recomputation as potential estimates evolve.

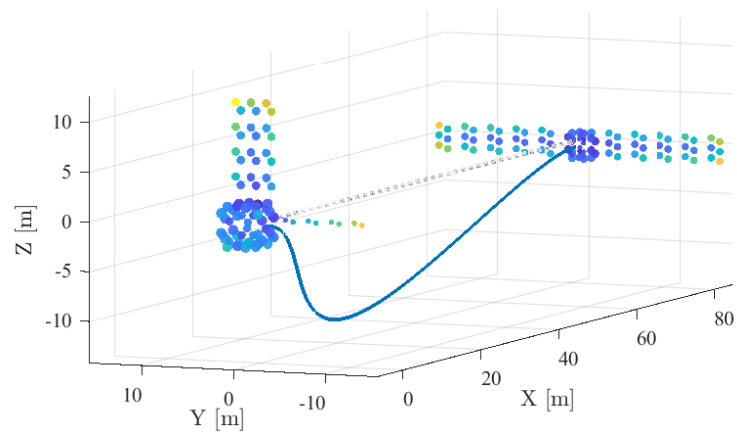


Figure 7.14: Pre-computed optimal trajectory, initial states.

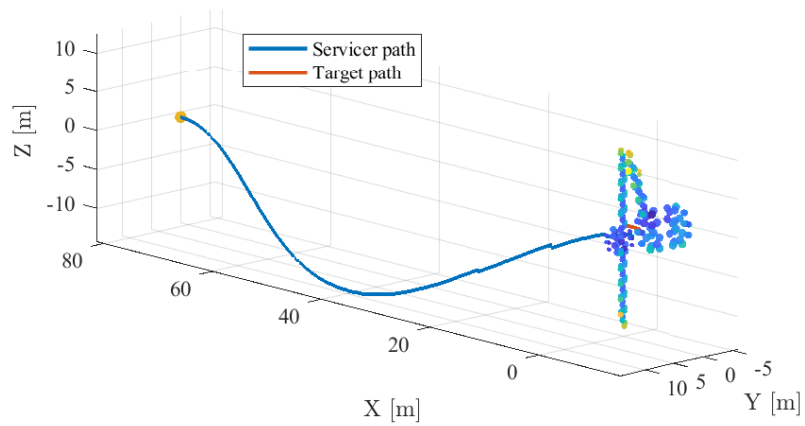


Figure 7.15: Pre-computed optimal trajectory, final result.

### 7.6.2 Monte Carlo Simulation

The polynomial-based guidance approach shows an order of magnitude improvement over the deterministic sampling-based approach, but has disadvantages in computation time that likely limit it to ground-side path planning. Therefore, it is important that this approach be robust to varying scenario parameters. A Monte Carlo simulation is conducted to evaluate performance under mis-modeled parameters. The same optimized trajectory was evaluated for 500 simulations. Inertia properties were evaluated with 5%  $1\sigma$  normally distributed variation in each element. Additionally, linearly time-varying spacecraft potentials were imposed for the target to represent the space environment evolution, ranging from the nominal  $10 \pm 0.1$  kV,  $1\sigma$  at the beginning of the simulation to  $10 \pm 1$  kV  $1\sigma$  at the end.

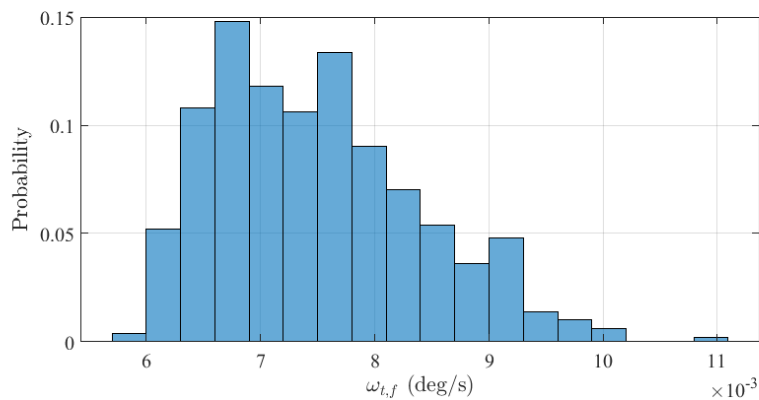


Figure 7.16: Target final rotational rate through 500 runs of a monte carlo simulation.

The results of this analysis show that the designed trajectory is robust to uncertainties in potential and inertia properties. Therefore it is reasonable to pre-compute a trajectory from the initial 80m hold point based on observations of relative potential, and follow that trajectory. The worst results in this assessment were  $0.011^\circ/\text{s}$ , which is approximately twice the optimized rate. However, this result is still approximately equal to the solution computed through the deterministic sampling-based approach.

## 7.7 Conclusions

While electrostatic perturbations significantly impact proximity operations dynamics, it is possible to use new methods to remotely sense the potential on an object in tandem with rapid techniques for evaluating the resultant inter-craft forces and torques to mitigate these concerns. The impact of electrostatic interactions are reduced substantially, if without imposing unreasonable burdens on operational constraints or computational resources. For targets that are poorly characterized or otherwise difficult to obtain accurate pose estimates for, it may be advantageous to optimize for both torque and pose estimation sensitivity. This could allow a relatively low, but not minimal, torque to be found, but with less impact from potential errors in target pose estimates.

## Chapter 8

### Conclusions and future work

#### 8.1 Overview and contributions of this work

Proximity operations in high earth orbits for servicing and debris remediation are an integral part of securing a sustainable future in space. Unlike in low earth orbits, the high earth orbit environment is particularly susceptible to severe spacecraft charging events. These multi-kV spacecraft potentials pose risks, but also opportunities through novel concepts for touchless actuation of debris. Regardless of whether the goal is to mitigate these potentials for safe rendezvous, monitoring potentials for improved dynamic models and path planning during proximity operations, or actively inducing and controlling them for relative motion control, future operations in this region require the ability to measure electrostatic potentials remotely.

The overarching goals of this work are to:

- Develop a method for remote sensing of electrostatic potential of a space object through simulation and experimental validation
- Evaluate the impact of electrostatic potentials on proximity operations in high earth orbits
- Develop guidance strategies to mitigate the effect of electrostatic perturbations during proximity operations.

Development of a method for remotely measuring the potential of an object is accomplished through the bremsstrahlung-based method in Chapter 2. The bremsstrahlung x-ray spectrum

contains information about the energy of incident electrons, which is used to determine the potential of the target if the source energy of the electrons is known.

Experimental evaluation required the development of a sophisticated vacuum chamber facility, which demonstrated that accuracies on the order of tens of volts are readily achievable through this sensing method. The potential effects of the space environment on the sensing method are shown to be tractable. In addition to a minor noise source for the x-ray detector, the space environment enables passive estimation of electrostatic potentials on nearby objects, with no requirement for an electron beam to generate x-ray emission.

The x-ray based sensing methods are combined with an alternative approach to remote potential estimation reliant on electron spectroscopy, improving the accuracy and robustness of each method individually. Simulations show that both methods could be used at ranges in excess of 100m.

Finally, electrostatic potentials known to occur due to natural spacecraft interactions with the environment are shown to have significant impacts on the dynamics of proximity operations. Guidance solutions are presented which leverage the ability to sense potentials remotely to mitigate the dynamic effects of spacecraft charging, improving safety of proximity operations trajectories.

## 8.2 Directions for future work

While this work has successfully demonstrated an x-ray spectroscopic method for touchless potential sensing, there are a number of areas for future research to relax assumptions made in this work or expand in new directions.

An interesting avenue exists to validate the passive potential sensing method with flight data. A number of missions, including SMART-1 and Rosetta, have operated both x-ray spectrometers and electron energy analyzers around airless bodies like the moon or comets. These missions have examples of x-ray spectra generated by ambient plasma electrons in the space environment, and refinements to passive potential sensing methods outlined here could enable the surface potential of these bodies to be estimated. Likewise, the NICER x-ray telescope on the ISS may provide

indications of visiting vehicles in the x-ray spectrum.

A key assumption in much of this work, both experimental and theoretical, has been of a continuously conducting spacecraft structure. While this is in accordance with design guidelines, many spacecraft have components which charge to different potentials. Therefore, it would be highly valuable to deconvolve the x-ray spectra generated by electrons with multiple landing energies. This would provide information about the charge distribution across the object, enabling better models of electrostatic forces and torques to be developed. Additionally, the ET concept could leverage such information to ensure the servicer's electron beam was interacting with the portions of the structure which provide the greatest force and torque returns, improving its efficiency.

Another assumption which could be evaluated is the approximation of negligible plasma interactions within the Debye sheath. Future work should consider what conditions may invalidate this assumption, and evaluate the effect of plasma contactors or other systems on inter-spacecraft electrostatic forces and torques. This could lead to orbital demonstration of touchless sensing and electrostatic actuation techniques in LEO plasma wakes as an analogue for high earth orbit environments.

## Bibliography

- [1] Jumbo Space Environment Simulation and Spacecraft Charging Chamber Characterization. Technical report, Air Force Research Laboratory, Space Vehicles Directorate, Albuquerque, New Mexico, 4 2015.
- [2] Level 1 science data from minxss-1 cubesat. Laboratory for Atmospheric and Space Physics, 2017.
- [3] X-123 si-pin x-ray detector specifications. Technical report, Amptek, Inc., 2018.
- [4] Goes-r series data book. Technical report, NASA GOESR Series Program Office, 2019.
- [5] Aerojet rocketdyne propulsion helps enable new satellite servicing market. Technical report, Aerojet Rocketdyne, 2020.
- [6] Shahrokh Akhlaghi, Ning Zhou, and Zenyu Huang. Adaptive adjustment of noise covariance in kalman filter for dynamic state estimation. CoRR, 2017.
- [7] R. Ambrose, D.L. Kahler, H.E. Lehtihet, and C.A. Quarles. Angular dependence of thick-target bremsstrahlung. Nuclear Instruments and Methods in Physics Research Section B: Beam Interactions with Materials and Atoms, 56-57:327–329, 1991.
- [8] Paul V. Anderson and Hanspeter Schaub. Local orbital debris flux study in the geostationary ring. Advances in Space Research, 51(12):2195–2206, 2013.
- [9] Phillip C. Anderson. Characteristics of spacecraft charging in low earth orbit. J. Geophys. Res., 117(A7):A07308, 07 2012.
- [10] Wolfgang Baumjohann and Rudolf A Treumann. Basic Space Plasma Physics. Imperial College Press, 1996.
- [11] M Belhaj, O Jbara, M.N Filippov, E.I Rau, and M.V Andrianov. Analysis of two methods of measurement of surface potential of insulators in sem: electron spectroscopy and x-ray spectroscopy methods. Applied Surface Science, 177(1):58 – 65, 2001.
- [12] M Bengtson, K Wilson, J Hughes, and H Schaub. Survey of the electrostatic tractor research for reorbiting passive geo space objects. Astrodynamics, 2(4):291–305, 2018.
- [13] M. Bengtson, K. Wilson, and H. Schaub. Broad-spectrum electron gun for laboratory simulation of orbital environments. In Proceedings of the 2021 AIAA SciTech Forum and Exposition, 2021.

- [14] Miles Bengtson. Electron Method for Touchless Electrostatic Potential Sensing of Neighboring Spacecraft. PhD thesis, University of Colorado Boulder, 2020.
- [15] Miles Bengtson, Joseph Hughes, and Hanspeter Schaub. Prospects and challenges for touchless sensing of spacecraft electrostatic potential using electrons. IEEE Transactions on Plasma Science, 2019.
- [16] Miles Bengtson, Kieran Wilson, and Hanspeter Schaub. Simulations and experimental results of electron method for remote spacecraft charge sensing. In Applied Space Environments Conference, 2019.
- [17] Miles T Bengtson and Hanspeter Schaub. Remote sensing of spacecraft potential at geosynchronous orbit using secondary and photo electrons. In AIAA Scitech 2019 Forum, page 0311, 2019.
- [18] Trevor Bennett and Hanspeter Schaub. Touchless electrostatic three-dimensional detumbling of large axi-symmetric debris. Journal of Astronautical Sciences, 62(3):233–253, 2015.
- [19] Trevor Bennett and Hanspeter Schaub. Capitalizing on relative motion in electrostatic detumbling of axi-symmetric geo objects. In 6th International Conference on Astrodynamics Tools and Techniques (ICATT), Darmstadt, Germany, March 14–17 2016.
- [20] Trevor Bennett, Daan Stevenson, Erik Hogan, Lauren McManus, and Hanspeter Schaub. Prospects and challenges of touchless debris despinning using electrostatics. Advances in Space Research, 56(3):557–568, 2015.
- [21] Trevor J. Bennett. On-Orbit 3-Dimensional Electrostatic Detumble for Generic Spacecraft Geometries. PhD thesis, University of Colorado Boulder, 2017.
- [22] Conor J. Benson and Daniel J. Scheeres. Averaged solar torque rotational dynamics for defunct satellites. Journal of Guidance, Control, and Dynamics, 0(0):1–18, 2021.
- [23] MJ Berger, JS Coursey, MA Zucker, J Chang, SM Seltzer, and PM Bergstrom. Stopping-power & range tables for electrons, protons, and helium ions: Nist standard reference database 124. NIST Physical Measurement Laboratory, 2017.
- [24] John Berryman and Hanspeter Schaub. Static equilibrium configurations in GEO coulomb spacecraft formations. In Advances in Astronautical Sciences, volume 120, pages 51–68. American Astronautical Society, 2005. Paper No. AAS 05–104.
- [25] John Berryman and Hanspeter Schaub. Analytical charge analysis for 2- and 3-craft coulomb formations. AIAA Journal of Guidance, Control, and Dynamics, 30(6):1701–1710, Nov.–Dec. 2007.
- [26] James Biggs and Albert Caubet. An inverse dynamics approach to the guidance of spacecraft in close proximity of tumbling debris. In 66th Annual International Astronomical Congress, 10 2015.
- [27] Jay P Boris. Relativistic plasma simulation-optimization of a hybrid code. In Proc. Fourth Conf. Num. Sim. Plasmas, pages 3–67, 1970.

- [28] Joseph E. Borovsky and Michael H. Denton. Magnetic field at geosynchronous orbit during high-speed stream-driven storms: Connections to the solar wind, the plasma sheet, and the outer electron radiation belt. Journal of Geophysical Research: Space Physics, 115(A8), 2010.
- [29] H. Brandhorst and J. Rodiek. Improving space utilization by increasing solar array reliability. In AIAA Space 2007, 2007.
- [30] Hajo Bruining. Physics and applications of secondary electron emission. 1954.
- [31] M. R. Carruth, D. Ferguson, R. Suggs, and M. McCollum. Iss and space environment interactions without operating plasma contactor. Technical report, NASA, 2001.
- [32] Anthony W Case, Justin C Kasper, Michael L Stevens, Kelly E Korreck, Kristoff Paulson, Peter Daigneau, Dave Caldwell, Mark Freeman, Thayne Henry, Brianna Klingensmith, et al. The solar probe cup on the parker solar probe. The Astrophysical Journal Supplement Series, 246(2):43, 2020.
- [33] Gustavo Castellano, János Osán, and Jorge Trincavelli. Analytical model for the bremsstrahlung spectrum in the 0.25–20 keV photon energy range. Spectrochimica Acta Part B: Atomic Spectroscopy, 59(3):313 – 319, 2004.
- [34] J. Cazaux. Surface potential and se detection in the sem. In Martina Luysberg, Karsten Tillmann, and Thomas Weirich, editors, EMC 2008 14th European Microscopy Congress 1–5 September 2008, Aachen, Germany, pages 519–520, Berlin, Heidelberg, 2008. Springer Berlin Heidelberg.
- [35] Soumyabrata Chakrabarty and Rajeev Jyoti. Absolute charging analysis of space-craft bodies using method of moments (mom). In 2015 IEEE Applied Electromagnetics Conference (AEMC), pages 1–2. IEEE, 2015.
- [36] Mengü Cho, Shirou Kawakita, Masao Nakamura, Masato Takahashi, Tetsuo Sato, and Yukishige Nozaki. Number of arcs estimated on solar array of a geostationary satellite. Journal of Spacecraft and Rockets, 42(4):740–748, 2005.
- [37] Philip Chow, Joseph Hughes, Trevor Bennett, and Hanspeter Schaub. Automated sphere geometry optimization for the volume multi-sphere method. In AAS/AIAA Spaceflight Mechanics Meeting, Feb. 14–18 2016.
- [38] Stephen Clark. Two commercial satellites link up in space for first time. SpaceFlight Now, 2020.
- [39] John H. Cover, Wolfgang Knauer, and Hans A. Maurer. Lightweight reflecting structures utilizing electrostatic inflation. US Patent 3,546,706, October 1966.
- [40] V.A. Davis and M. J. Mandell. Plasma Interactions with Spacecraft. Volume 2, NASCAP-2K Scientific Documentation for Version 4.1. Science Applications International Corp, 4.1 edition, 2011.
- [41] A. J. Dean, A. J. Bird, N. Diallo, C. Ferguson, J. J. Lockley, S. E. Shaw, M. J. Westmore, and D. R. Willis. The modelling of background noise in astronomical gamma ray telescopes. Space Science Reviews, 105(1-2):285–376, 2003.

- [42] JR Dennison, C.D. Thomson, J.T. Kite, V.V. Zavyalov, and Jodie Corbridge. Materials characterization at utah state university: Facilities and knowledge-base of electronic properties of materials applicable to spacecraft charging. In 8th Spacecraft Charging Technology Conference, Huntsville, Alabama, October 2003.
- [43] M. H. Denton, G. D. Reeves, B. A. Larsen, R. H. W. Friedel, M. F. Thomsen, P. A. Fernandes, R. M. Skoug, H. O. Funsten, and L. K. Sarno-Smith. On the origin of low-energy electrons in the inner magnetosphere: Fluxes and pitch-angle distributions. Journal of Geophysical Research: Space Physics, 122(2):1789–1802, 2017.
- [44] BT Draine and EE Salpeter. On the physics of dust grains in hot gas. The Astrophysical Journal, 231:77–94, 1979.
- [45] W. Duane and F.L. Hunt. On x-ray wave-lengths. Phys. Rev., 6:166–172, Aug 1915.
- [46] Heiko Engwerda. Remote sensing for spatial electrostatic characterization using the multi-sphere method. Master’s thesis, Delft University of Technology, Delft, The Netherlands, March 2017.
- [47] CL Enloe. High-resolution retarding potential analyzer. Review of scientific instruments, 65(2):507–508, 1994.
- [48] J. Sempau F. Salvat, J. M. Fernández-Varea. Penelope 2006: A code system for monte carlo simulation of electron and photon transport. Nuclear Energy Agency Organisation For Economic Co-Operation And Development, 2006.
- [49] D. C. Ferguson, R. C. Hoffmann, D. P. Engelhart, and E. A. Plis. Voltage threshold and power degradation rate for gps solar array arcing. IEEE Transactions on Plasma Science, 45(8):1972–1975, Aug 2017.
- [50] D. C. Ferguson, J. Murray-Krezan, D. A. Barton, J. R. Dennison, and S. A. Gregory. Feasibility of detecting spacecraft charging and arcing by remote sensing. Journal of Spacecraft and Rockets, 51(6), 2014.
- [51] Dale C. Ferguson, William F. Denig, and Juan V. Rodriguez. Plasma conditions during the galaxy 15 anomaly and the possibility of esd from subsurface charging. In AIAA Aerospace Sciences Meeting including the New Horizons Forum and Aerospace Exposition, Orlando, FL, January 4–7 2011. Paper AIAA 2011-1061.
- [52] Dale C. Ferguson and G. Barry Hillard. New nasa see leo spacecraft charging design guidelines-how to survive in leo rather than geo. Technical report, NASA Glenn Research Center, Cleveland, Ohio, Dec. 2003. NASA/TM—2003-212737.
- [53] Dale C. Ferguson, Jeremy Murray-Krezan, and David A. Barton. On the feasibility of detecting spacecraft charging and arcing by remote sensing. In 5th AIAA Atmospheric and Space Environments Conference, June 24–27 2014.
- [54] T. Flohrer, H. Krag, H. Klinkrad, and T. Schildknecht. Feasibility of performing space surveillance tasks with a proposed space-based optical architecture. Advances in Space Research, 47(6):1029 – 1042, 2011.

- [55] D. Gonzales, B. Cavness, and S. Williams. Angular distribution of thick-target bremsstrahlung produced by electrons with initial energies ranging from 10 to 20 keV incident on Ag. Phys. Rev. A, 84:052726, Nov 2011.
- [56] Michael Goodman, Aurelio Paez, Emily Willis, and Anthony DeStefano. An analytic model for estimating the first contact resistance needed to avoid damaging esd during spacecraft docking in geo. In Applied Space Environments Conference, 2019.
- [57] M Guerra, M Manso, S Longelin, S Pessanha, and M L Carvalho. Performance of three different Si X-ray detectors for portable XRF spectrometers in cultural heritage applications. Journal of Instrumentation, 7(10):C10004–C10004, oct 2012.
- [58] J.S. Halekas, G.T. Delory, D.A. Brain, R.P. Lin, M.O. Fillingim, C.O. Lee, R. A. Mewaldt, T.J. Stubbs, W.M. Farrell, and M.K. Hudson. Extreme lunar surface charging during solar energetic particle events. Geophysical Research Letters, 34(2), 2007.
- [59] David J. Hall and Andrew Holland. Space radiation environment effects on X-ray CCD background. Nuclear Instruments and Methods in Physics Research Section A: Accelerators, Spectrometers, Detectors and Associated Equipment, 612(2):320–327, jan 2010.
- [60] Hamamatsu. S2D2 VUV Light Source Unit L10706 Series, 3 2014.
- [61] Roger F Harrington. Field computation by moment methods. Wiley-IEEE Press, 1993.
- [62] D. P. Hartley, M. H. Denton, and J. V. Rodriguez. Electron number density, temperature, and energy density at geo and links to the solar wind: A simple predictive capability. Journal of Geophysical Research: Space Physics, 119(6):4556–4571, 2014.
- [63] Steffen Hauf, Markus Kuster, Dieter H. H. Hoffmann, Philipp-Michael Lang, Stephan Neff, Maria Grazia Pia, and Lothar Strüder. Background simulations for the wide field imager aboard the ATHENA X-ray Observatory. In Tadayuki Takahashi, Stephen S. Murray, and Jan-Willem A. den Herder, editors, Space Telescopes and Instrumentation 2012: Ultraviolet to Gamma Ray, volume 8443, page 84435J, sep 2012.
- [64] Jennifer T. Heath, Chun-Sheng Jiang, and Mowafak M. Al-Jassim. Measurement of semiconductor surface potential using the scanning electron microscope. Journal of Applied Physics, 111(4):046103, 2012.
- [65] B.L. Henke, E.M. Gullikson, and J.C. Davis. X-ray interactions: Photoabsorption, scattering, transmission, and reflection at  $e = 50\text{--}30,000$  eV,  $z = 1\text{--}92$ . Atomic Data and Nuclear Data Tables, 54(2):181–342, 1993.
- [66] Erik Hogan and Hanspeter Schaub. Collinear invariant shapes for three-craft coulomb formations. Acta Astronautica, 12:78–89, March–April 2012.
- [67] Erik Hogan and Hanspeter Schaub. Linear stability and shape analysis of spinning three-craft coulomb formations. Celestial Mechanics and Dynamical Astronomy, 112(2):131–148, 2012.
- [68] Erik Hogan and Hanspeter Schaub. Relative motion control for two-spacecraft electrostatic orbit corrections. AIAA Journal of Guidance, Control, and Dynamics, 36(1):240–249, Jan. – Feb. 2013.

- [69] Erik A. Hogan and Hanspeter Schaub. Three-axis attitude control using redundant reaction wheels with continuous momentum dumping. In AAS/AIAA Spaceflight Mechanics Meeting, Kauai, Hawaii, Feb. 10–14 2013. Paper AAS 13-292.
- [70] J. M. Horack, G. J. Fishman, C. A. Meegan, R. B. Wilson, and W. S. Paciesas. Batse observations of bremsstrahlung from electron precipitation events. AIP Conference Proceedings, 265(1):373–377, 1991.
- [71] Joseph Hughes and Hanspeter Schaub. Guidance, navigation and control advances in electrostatic attitude control on passive geo objects. In 9th International Workshop on Satellite Constellations and Formation Flying, Boulder, CO, June 19–21 2017. Paper No. IWSCFF 17-16.
- [72] Joseph A. Hughes and Hanspeter Schaub. Heterogeneous surface multisphere models using method of moments foundations. Journal of Spacecraft and Rockets, 56(4):1259–1266, 2019.
- [73] W. L. Imhof. Review of energetic ( $\geq 20$  keV) bremsstrahlung x-ray measurements from satellites. Space Science Reviews, 29(2):201–217, Jun 1981.
- [74] Gabriel Ingram, Joseph Hughes, Trevor Bennett, Christine Reily, and Hanspeter Schaub. Autonomous volume multi-sphere-model development using electric field matching. In AAS Spaceflight Mechanics Meeting, Feb 5–9 2017.
- [75] Keizo Ishii. Pixe and its applications to elemental analysis. Quantum Beam Science, 3(2), 2019.
- [76] Danil Ivanov, Michael Ovchinnikov, and Marianna Sakovich. Relative pose and inertia determination of unknown satellite using monocular vision. International Journal of Aerospace Engineering, 09 2018.
- [77] Marko Jankovic, Kartik Kumar, Natalia Ortiz, Juan Manuel Romero Martin, Frank Kirchner, Francesco Topputo, Scott Walker, and Massimiliano Vasile. Robotic system for active debris removal: Requirements, state-of-the-art and concept architecture of the rendezvous and capture (rvc) control system. 09 2015.
- [78] A. Kahoul, A. Abassi, B. Deghfel, and M. Nekkab. K-shell fluorescence yields for elements with  $Z \geq 99$ . Radiation Physics and Chemistry, 80(3):369 – 377, 2011.
- [79] Y. Kamata, T. Takeshima, T. Okada, and K. Terada. Detection of x-ray fluorescence line feature from the lunar surface. Advances in Space Research, 23(11):1829 – 1832, 1999. The Moon and Mars.
- [80] Yu S. Karavaev, R. M Kopyatkevich, M. N. Mishina, G. S. Mishin, P. G. Papishev, and P. N. Shaburov. The dynamic properties of rotation and optical characteristics of space debris at geostationary orbit. Advances in the Astronautical Sciences, 119, 2004.
- [81] I. Katz, V. A. Davis, and D. B. Snyder. Mechanism for spacecraft charging initiated destruction of solar arrays in geo.
- [82] Ira Katz, V. A. Davis, and David B. Snyder. Mechanism for spacecraft charging initiated destruction of solar arrays in geo. In 36<sup>th</sup> Aerospace Sciences Meeting and Exhibit, Reno, NV, Jan. 12–15 1998.

- [83] Lyon B. King, Gordon G. Parker, Satwik Deshmukh, and Jer-Hong Chong. Spacecraft formation-flying using inter-vehicle coulomb forces. Technical report, NASA/NIAC, January 2002.
- [84] Lyon B. King, Gordon G. Parker, Satwik Deshmukh, and Jer-Hong Chong. Study of inter-spacecraft coulomb forces and implications for formation flying. AIAA Journal of Propulsion and Power, 19(3):497–505, May–June 2003.
- [85] Lynn Kissel, C.A. Quarles, and R.H. Pratt. Shape functions for atomic-field bremsstrahlung from electrons of kinetic energy 1–500 keV on selected neutral atoms  $1 \leq z \leq 92$ . Atomic Data and Nuclear Data Tables, 28(3):381–460, 1983.
- [86] Shoji Kitamura, Yukio Hayakawa, Kumi Nitta, Satomi Kawamoto, and Yasushi Ohkawa. A reorbiter for large geo debris objects using ion beam irradiation. In 63rd International Astronautical Congress, Naples, Italy, 2012. Paper No. IAC-12-A6.7.10.
- [87] William C Knudsen, Karl Spenner, Jack Bakke, and Vit Novak. Pioneer venus orbiter planar retarding potential analyzer plasma experiment. IEEE Transactions on Geoscience and Remote Sensing, (1):54–59, 1980.
- [88] Jeffrey W. Kruk, Michael A. Xapsos, Nerses Armani, Craig Stauffer, and Christopher M. Hirata. Radiation-induced backgrounds in astronomical instruments: Considerations for geosynchronous orbit and implications for the design of the WFIRST Wide-field instrument. Publications of the Astronomical Society of the Pacific, 128(961):035005, feb 2016.
- [89] Róbert Kákonyi, Miklós Erdélyi, and Gábor Szabó. Monte carlo analysis of energy dependent anisotropy of bremsstrahlung x-ray spectra. Medical Physics, 36:3897–3905, 2009.
- [90] S. T. Lai and M. F. Tautz. Aspects of spacecraft charging in sunlight. IEEE Transactions on Plasma Science, 34(5):2053–2061, 2006.
- [91] Shu T Lai. Fundamentals of Spacecraft Charging: Spacecraft Interactions with Space Plasmas. Princeton University Press, 2011.
- [92] F Lei, J.P. Leray, P. Mandrou, J Paul, J.P. Roques, and F. Lebrun. The background in a high earth orbit as measured by the soft  $\gamma$ -ray telescope SIGMA. Nuclear Instruments and Methods in Physics Research Section A: Accelerators, Spectrometers, Detectors and Associated Equipment, 321(3):598–608, oct 1992.
- [93] Meike List, Stefanie Bremer, Benny, and Hanns Selig. Modelling of solar radiation pressure effects: Parameter analysis for the microscope mission. International Journal of Aerospace Engineering, 2015.
- [94] Yuqiang Liu, Yang Zhao, Chunlin Tan, Huawei Liu, and Yongjian Liu. Economic value analysis of on-orbit servicing for geosynchronous communication satellites. Acta Astronautica, 180:176–188, 2021.
- [95] Phil Lundgreen and J. R. Dennison. Strategies for determining electron yield material parameters for spacecraft charge modeling. Space Weather, 18(4), 2020.
- [96] Yazhong Luo, Jin Zhang, and Guojin Tang. Survey of orbital dynamics and control of space rendezvous. Chinese Journal of Aeronautics, 27(1):1 – 11, 2014.

- [97] P. Charles M. Lamoureux. General deconvolution of thin-target and thick-target bremsstrahlung spectra to determine electron energy distributions. Radiation Physics and Chemistry, 75(10), October 2006.
- [98] Terence Marshall and Mitchell Fletcher. Meeting high-quality rwa commercial demand through innovative design. In Space Mechanisms and Tribology, Proceedings of the 8th European Symposium, 1999.
- [99] R. A. Masterson, M. Chodas, L. Bayley, B. Allen, J. Hong, P. Biswas, C. McMenamin, K. Stout, E. Bokhour, H. Bralower, D. Carte, S. Chen, M. Jones, S. Kissel, M. Smith F. Schmidt, G. Sondecker, L. F. Lim, D. S. Lauretta, J. E. Grindlay, and R. P. Binzel. Regolith x-ray imaging spectrometer (rexis) aboard the osiris-rex asteroid sample return mission. Space Science Reviews, 214(48), February 2018.
- [100] J.-C. Matéo-Vélez, A. Sicard, D. Payan, N. Ganushkina, N. P. Meredith, and I. Sillanpää. Spacecraft surface charging induced by severe environments at geosynchronous orbit. Space Weather, 16(1):89–106, 2018.
- [101] Jordan Maxwell, Kieran Wilson, Joseph Hughes, and Hanspeter Schaub. Multisphere method for flexible conducting space objects: Modeling and experiments. AIAA Journal of Spacecraft and Rockets, 57(2):225–234, 2020.
- [102] J. E. Mazur, J. F. Fennell, J. L. Roeder, P. T. O’Brien, T. B. Guild, and J. J. Likar. The timescale of surface-charging events. IEEE Transactions on Plasma Science, 40(2):237–245, 2012.
- [103] G H McCall. Calculation of x-ray bremsstrahlung and characteristic line emission produced by a maxwellian electron distribution. Journal of Physics D: Applied Physics, 15(5):823–831, may 1982.
- [104] Christopher S. Moore, Amir Caspi, Thomas N. Woods, Phillip C. Chamberlin, Brian R. Dennis, Andrew R. Jones, James P. Mason, Richard A. Schwartz, and Anne K. Tolbert. The instruments and capabilities of the miniature x-ray solar spectrometer (minxss) cubesats. Solar Physics, 293(2), Jan 2018.
- [105] F. S. Mozer. Dc and low-frequency double probe electric field measurements in space. Journal of Geophysical Research: Space Physics, 121(11):10,942–10,953, 2016.
- [106] E. G. Mullen, M. S. Gussenhoven, D. A Hardy, T. A. Aggson, and B. G. Ledley. Scatha survey of high-voltage spacecraft charging in sunlight. Journal of Geophysical Research, 91(A2):1474–1490, 1986.
- [107] EG Mullen, MS Gussenhoven, DA Hardy, TA Aggson, BG Ledley, and E Whipple. Scatha survey of high-level spacecraft charging in sunlight. Journal of Geophysical Research: Space Physics, 91(A2):1474–1490, 1986.
- [108] T. Muranaka, S. Hosoda, J. Kim, S. Hatta, K. Ikeda, T. Hamanaga, M. Cho, H. Usui, H. O. Ueda, K. Koga, and T. Goka. Development of multi-utility spacecraft charging analysis tool (muscat). IEEE Transactions on Plasma Science, 36(5):2336–2349, 2008.

- [109] Naomi Murdoch, Dario Izzo, Claudio Bombardelli, Ian Carnelli, Alain Hilgers, and David Rodgers. Electrostatic tractor for near earth object deflection. In 59th International Astronautical Congress, Glasgow Scotland, 2008. Paper IAC-08-A3.I.5.
- [110] Arun Natarajan and Hanspeter Schaub. Orbit-nadir aligned coulomb tether reconfiguration analysis. Journal of the Astronautical Sciences, 56(4):573–592, Oct. – Dec. 2008.
- [111] Arun Natarajan and Hanspeter Schaub. Hybrid control of orbit normal and along-track two-craft coulomb tethers. Aerospace Science and Technology, 13(4–5):183–191, June–July 2009.
- [112] Arun Natarajan, Hanspeter Schaub, and Gordon G. Parker. Reconfiguration of a nadir-pointing 2-craft coulomb tether. Journal of British Interplanetary Society, 60(6):209–218, June 2007.
- [113] M. Nose, T. Iyemori, M. Sugiura, and T. Kamei. Kp index. World Data Center for Geomagnetism, Kyoto, 2020.
- [114] L.S. Novikov, A.A. Makletsov, and V.V. Sinolits. Comparison of coulomb-2, nascap-2k, muscat and spis codes for geosynchronous spacecraft charging. Advances in Space Research, 57(2):671–680, 2016.
- [115] Takashi Okajima, Yang Soong, Erin R. Balsamo, Teruaki Enoto, Larry Olsen, Richard Koennecke, Larry Lozipone, John Kearney, Sean Fitzsimmons, Ai Numata, Steven J. Kenyon, Zaven Arzoumanian, and Keith Gendreau. Performance of NICER flight x-ray concentrator. In Jan-Willem A. den Herder, Tadayuki Takahashi, and Marshall Bautz, editors, Space Telescopes and Instrumentation 2016: Ultraviolet to Gamma Ray, volume 9905, pages 1495 – 1501. International Society for Optics and Photonics, SPIE, 2016.
- [116] R. C. Olsen. Record charging events from applied technology satellite 6. Journal of Spacecraft and Rockets, 24(4):362–366, 1987.
- [117] R. C. Olsen and C. K. Purvis. Observations of charging dynamics. Journal of Geophysical Research, 88:5657–5667, July 1983.
- [118] Richard Christopher Olsen, Carl E. McIlwain, and Elden C. Whipple Jr. Observations of differential charging effects on ats 6. Journal of Geophysical Research: Space Physics, 86(A8):6809–6819, 1981.
- [119] Roberto Opromolla, Giancarmine Fasano, Giancarlo Rufino, and Michele Grassi. Uncooperative pose estimation with a lidar-based system. Acta Astronautica, 110:287 – 297, 2015.
- [120] Ahmet Ozkul, A. Lopatin, and Alex Shipp. Initial correlation results of charge sensor data from six intelsat viii class satellites with other space and ground based measurements. 2004.
- [121] Lucien Pages, Evelyne Bertel, Henri Joffre, and Laodamas Sklavenitis. Energy loss, range, and bremsstrahlung yield for 10-keV to 100-MeV electrons in various elements and chemical compounds. Atomic Data and Nuclear Data Tables, 4(C):1–27, 1972.
- [122] T. Paulmier, B. Dirassen, M. Belhaj, V. Inguibert, S. Duzellier, C. Pons, S. Rémaury, and D. Payan. Experimental test facilities for representative characterization of space used materials. In 14th Spacecraft Charging Technology Conference, Noordwijk, Netherlands, April 4 – 8 2016.

- [123] D. M. Perfetto, R. Opromolla, M. Grassi, and C. Schmitt. Lidar-based model reconstruction for spacecraft pose determination. In 2019 IEEE 5th International Workshop on Metrology for AeroSpace (MetroAeroSpace), pages 1–6, 2019.
- [124] C Pollock, T Moore, A Jacques, J Burch, U Gliese, Y Saito, T Omoto, L Avannov, A Barrie, V Coffey, et al. Fast plasma investigation for magnetospheric multiscale. Space Science Reviews, 199(1-4):331–406, 2016.
- [125] S. M. L. Prokopenko and J. G. Laframboise. High-voltage differential charging of geostationary spacecraft. Journal of Geophysical Research, 85(A8):4125–4131, Aug. 1980.
- [126] Carolyn K. Purvis, Henry B. Garrett, A. C. Whittlesey, and N. John Stevens. Design guidelines for ‘ assessing and controlling spacecraft charging effects. Technical Report 2361, NASA, 1984.
- [127] Hong Qin, Shuangxi Zhang, Jianyuan Xiao, Jian Liu, Yajuan Sun, and William M Tang. Why is boris algorithm so good? Physics of Plasmas, 20(8):084503, 2013.
- [128] Benjamin B. Reed, Robert C. Smith, Bo J. Naasz, Joseph F. Pellegrino, and Charles E. Bacon. The Restore-L Servicing Mission.
- [129] Ludwig Reimer. Scanning Electron Microscopy: Physics of Image Formation and Microanalysis, Second Edition. Springer-Verlag Berlin Heidelberg, 2 edition, 1998.
- [130] Scott Robertson, Zoltan Sternovsky, and Bob Walch. Reduction of asymmetry transport in the annular penning trap. Physics of Plasmas, 11(5):1753–1756, 2004.
- [131] Á. Romero-Calvo, G. Cano-Gómez, and H. Schaub. Electron beam expansion and deflection uncertainty for active spacecraft charging applications. In Proceedings of the 2021 AIAA SciTech Forum and Exposition, 2021.
- [132] Lois K. Sarno-Smith, Brian A. Larsen, Ruth M. Skoug, Michael W. Liemohn, Aaron Breneman, John R. Wygant, and Michelle F. Thomsen. Spacecraft surface charging within geosynchronous orbit observed by the van allen probes. Space Weather, 14(2):151–164, 2016.
- [133] Hanspeter Schaub, Christopher Hall, and John Berryman. Necessary conditions for circularly-restricted static coulomb formations. Journal of the Astronautical Sciences, 54(3–4):525–541, July-Dec. 2006.
- [134] Hanspeter Schaub and John L. Junkins. Analytical Mechanics of Space Systems. AIAA Education Series, Reston, VA, 4th edition, October 2019.
- [135] Hanspeter Schaub and Daniel F. Moorer. Geosynchronous large debris reorbiter: Challenges and prospects. In AAS Kyle T. Alfriend Astrodynamics Symposium, Monterey, CA, May 17–19 2010. Paper No. AAS 10-311.
- [136] Hanspeter Schaub and Daniel F. Moorer. Geosynchronous large debris reorbiter: Challenges and prospects. The Journal of the Astronautical Sciences, 59(1–2):161–176, 2014.
- [137] Hanspeter Schaub and Zoltán Sternovsky. Active space debris charging for contactless electrostatic disposal maneuvers. Advances in Space Research, 53(1):110–118, 2014.

- [138] Hanspeter Schaub and Daan Stevenson. Prospects of relative attitude control using coulomb actuation. Journal of the Astronautical Sciences, 60, 2013.
- [139] Robert (Lauchie) Scott and Alex Ellery. An approach to ground based space surveillance of geostationary on-orbit servicing operations. Acta Astronautica, 112:56 – 68, 2015.
- [140] Carl R. Seubert, Stephan Panosian, and Hanspeter Schaub. Attitude and power analysis of two-node multitethered coulomb structures. AIAA Journal of Spacecraft and Rockets, 48(6):1033–1045, Nov. – Dec. 2011.
- [141] Carl R. Seubert and Hanspeter Schaub. Closed-loop one-dimensional charged relative motion experiments simulating constrained orbital motion. AIAA Journal of Guidance, Control, and Dynamics, 33(6):1856–1865, Nov.–Dec 2009.
- [142] Carl R. Seubert and Hanspeter Schaub. One-dimensional testbed for coulomb controlled spacecraft studies. In AAS/AIAA Spaceflight Mechanics Meeting, Savannah, Georgia, Feb. 8–12 2009. Paper AAS 09–115.
- [143] Carl R. Seubert and Hanspeter Schaub. Electrostatic force model for terrestrial experiments on the coulomb testbed. In 61st International Astronautical Congress, Prague, CZ, Sept. 2010. International Astronautical Federation. Paper IAC-10.C1.1.9.
- [144] Carl R. Seubert, Laura A. Stiles, and Hanspeter Schaub. Effective coulomb force modeling for spacecraft in earth orbit plasmas. Advances in Space Research, 2014.
- [145] A. Sicard-Piet, S. Bourdarie, D. Boscher, R. H. W. Friedel, M. Thomsen, T. Goka, H. Matsumoto, and H. Koshiishi. A new international geostationary electron model: Ige-2006, from 1 keV to 5.2 MeV. Space Weather, 6(7), 2008.
- [146] Dmitry A. Sizov and Vladimir S. Aslanov. Space debris removal with harpoon assistance: Choice of parameters and optimization. Journal of Guidance, Control, and Dynamics, 0(0):1–12, 0.
- [147] Sofya Spiridonova and Ralph Kahle. Relative orbit dynamics in near-geostationary orbit. In International Symposium on Space Flight Dynamics, Munich, Germany, Oct. 19–23 2015.
- [148] Daan Stevenson and Hanspeter Schaub. Multi-sphere method for modeling electrostatic forces and torques. Advances in Space Research, 51(1):10–20, Jan. 2013.
- [149] Daan Stevenson and Hanspeter Schaub. Rotational testbed for coulomb induced spacecraft attitude control. In 5th International Conference on Spacecraft Formation Flying Missions and Technologies, München, Germany, May 29–31 2013.
- [150] Daan Stevenson and Hanspeter Schaub. Terrestrial testbed for remote coulomb spacecraft rotation control. International Journal of Space Science and Engineering, 2(1):96 – 112, 2013.
- [151] AZ Technology. Az-93 white thermal control, electrically conductive paint / coating. AZ Technology, 2004.
- [152] Jorge Trincavelli and Gustavo Castellano. The prediction of thick target electron bremsstrahlung spectra in the 0.25–50 keV energy range. Spectrochimica Acta Part B: Atomic Spectroscopy, 63(1):1 – 8, 2008.

- [153] Pavel Trivailo and Hirohisa Kojima. Dynamics of the net systems, capturing space debris. TRANSACTIONS OF THE JAPAN SOCIETY FOR AERONAUTICAL AND SPACE SCIENCES, AEROSPACE TECHNOLOGY JAPAN, 14, 01 2016.
- [154] M. Tuszewski, T. E. Cayton, J. C. Ingraham, and R. M. Kippen. Bremsstrahlung effects in energetic particle detectors. Space Weather, 2(10), 2004.
- [155] Harsh Vasavada and Hanspeter Schaub. Analytic solutions for equal mass four-craft static coulomb formation. Journal of the Astronautical Sciences, 56(1):17–40, Jan. – March 2008.
- [156] Shuquan Wang and Hanspeter Schaub. Nonlinear charge control for a collinear fixed shape three-craft equilibrium. AIAA Journal of Guidance, Control, and Dynamics, 34(2):359–366, Mar.–Apr. 2011.
- [157] Shuquan Wang and Hanspeter Schaub. Nonlinear feedback control of a spinning two-spacecraft coulomb virtual structure. IEEE Transactions on Aerospace and Electronic Systems, 47(3):2055–2067, July 2011.
- [158] Thomas P Wangler. RF Linear accelerators. John Wiley & Sons, 2008.
- [159] Gregor Wentzel. Über strahlungslose quantensprünge. Zeitschrift für Physik, 43(8):524–530, Aug 1927.
- [160] E. C. Whipple. Observation of photoelectrons and secondary electrons reflected from a potential barrier in the vicinity of ats 6. Journal of Geophysical Research, 81(4):715–719, Feb. 1976.
- [161] Phyllis L Whittlesey, Davin E Larson, Justin C Kasper, Jasper Halekas, Mamuda Abatcha, Robert Abiad, M Berthomier, AW Case, Jianxin Chen, David W Curtis, et al. The solar probe analyzers—electrons on the parker solar probe. The Astrophysical Journal Supplement Series, 246(2):74, 2020.
- [162] Kieran Wilson, Miles Bengtson, and Hanspeter Schaub. X-ray spectroscopic determination of electrostatic potential and material composition for spacecraft: Experimental results. Space Weather, 18(4), April 2020.
- [163] Kieran Wilson and Hanspeter Schaub. X-ray spectroscopy for electrostatic potential and material determination of space objects. IEEE Transactions on Plasma Science, 2019.
- [164] Kieran Wilson and Hanspeter Schaub. Environmental x-ray considerations for bremsstrahlung-based surface potential determination. In AIAA SciTech, Orlando, Florida, Jan. 6–10 2020.
- [165] Kieran Wilson and Hanspeter Schaub. Impact of electrostatic perturbations on proximity operations in high earth orbits. In AAS/AIAA Astrodynamics Specialist Conference, Lake Tahoe, CA, Aug. 9–13 2020.
- [166] Kieran T. Wilson, Miles Bengtson, and Hanspeter Schaub. Hybrid method of remote sensing of electrostatic potential for proximity operations. In IEEE Aerospace Engineering Conference, Big Sky, MO, March 7–14 2020.

- [167] Kieran T. H. Wilson, Miles Bengtson, Jordan Maxwell, 'Alvaro Romero Calvo, and Hanspeter Schaub. Characterization of the eclips space environments simulation facility. In AIAA SciTech Conference, Nashville, TN, Jan. 11–15 2021.
- [168] Gordon L. Wrenn. Conclusive evidence for internal dielectric charging anomalies on geosynchronous communications spacecraft. Journal of Spacecraft and Rockets, 32(3):514–520, 1995.
- [169] Wei Xu and Robert A. Marshall. Characteristics of energetic electron precipitation estimated from simulated bremsstrahlung x-ray distributions. Journal of Geophysical Research: Space Physics, 124(4):2831–2843, 2019.
- [170] Youngjin Choi and Jinsuk Wang. Design of solar cell array preventing electrostatic discharge for satellite use. In IECEC-97 Proceedings of the Thirty-Second Intersociety Energy Conversion Engineering Conference (Cat. No.97CH6203), volume 1, pages 416–421 vol.1, 1997.

## Appendix A

### Multi-Sphere Model Geometries

The development of the surface multi-sphere models in this work depend on the specific source geometry used. The models for both servicer and target are included here for reproducibility of this work.

#### A.1 Servicer MSM Model

The following table provides sphere positions and radii for the two-panel servicer MSM model.

Sphere X Pos [m]	Sphere Y Pos [m]	Sphere Z Pos [m]	Sphere Radius [m]
2.000	0.417	-1.250	0.425
1.000	0.833	-1.250	0.425
2.000	-0.833	-1.250	0.425
1.000	-0.417	-1.250	0.425
-0.000	0.833	-0.833	0.260
-0.000	0.417	-0.417	0.260
-0.000	0.833	0.417	0.260
0.000	-0.417	0.417	0.260
-0.000	0.417	0.833	0.260
0.000	-0.417	-0.833	0.260
0.000	-0.833	0.833	0.260
0.000	-0.833	-0.417	0.260

3.000	0.833	-0.833	0.260
3.000	0.417	-0.417	0.260
3.000	0.833	0.417	0.260
3.000	-0.417	0.417	0.260
3.000	0.417	0.833	0.260
3.000	-0.417	-0.833	0.260
3.000	-0.833	0.833	0.260
3.000	-0.833	-0.417	0.260
1.000	1.250	0.417	0.425
1.000	1.250	-0.833	0.425
2.000	1.250	0.833	0.425
2.000	1.250	-0.417	0.425
1.000	-1.250	0.417	0.425
1.000	-1.250	-0.833	0.425
2.000	-1.250	0.833	0.425
2.000	-1.250	-0.417	0.425
2.000	0.417	1.250	0.425
1.000	0.833	1.250	0.425
2.000	-0.833	1.250	0.425
1.000	-0.417	1.250	0.425
1.000	1.083	6.917	0.375
1.000	1.417	14.383	0.375
1.000	-0.917	6.917	0.375
1.000	0.417	14.383	0.375
1.000	1.417	3.183	0.375
1.000	0.083	9.717	0.375
1.000	1.417	8.783	0.375

1.000	1.083	4.117	0.375
1.000	-0.583	14.383	0.375
1.000	1.417	11.583	0.375
1.000	1.083	12.517	0.375
1.000	1.083	15.317	0.375
1.000	1.417	5.983	0.375
1.000	-0.583	8.783	0.375
1.000	0.417	11.583	0.375
1.000	1.083	9.717	0.375
1.000	-0.583	11.583	0.375
1.000	0.417	8.783	0.375
1.000	-0.917	15.317	0.375
1.000	0.083	12.517	0.375
1.000	0.083	15.317	0.375
1.000	-0.917	12.517	0.375
1.000	-0.917	9.717	0.375
1.000	0.083	4.117	0.375
1.000	0.083	6.917	0.375
1.000	-0.583	5.983	0.375
1.000	0.417	3.183	0.375
1.000	0.417	5.983	0.375
1.000	-0.583	3.183	0.375
1.000	-0.917	4.117	0.375
1.000	1.417	-9.717	0.375
1.000	0.083	-14.383	0.375
1.000	1.417	-6.917	0.375
1.000	1.083	-14.383	0.375

1.000	-0.917	-14.383	0.375
1.000	1.417	-15.317	0.375
1.000	0.417	-15.317	0.375
1.000	1.417	-12.517	0.375
1.000	0.083	-8.783	0.375
1.000	1.083	-11.583	0.375
1.000	1.083	-5.983	0.375
1.000	1.417	-4.117	0.375
1.000	0.083	-3.183	0.375
1.000	1.083	-8.783	0.375
1.000	0.417	-9.717	0.375
1.000	0.417	-6.917	0.375
1.000	0.417	-4.117	0.375
1.000	1.083	-3.183	0.375
1.000	-0.917	-5.983	0.375
1.000	-0.583	-4.117	0.375
1.000	-0.917	-3.183	0.375
1.000	-0.583	-6.917	0.375
1.000	0.083	-5.983	0.375
1.000	-0.583	-9.717	0.375
1.000	0.417	-12.517	0.375
1.000	-0.583	-12.517	0.375
1.000	0.083	-11.583	0.375
1.000	-0.583	-15.317	0.375
1.000	-0.917	-8.783	0.375
1.000	-0.917	-11.583	0.375

## A.2 Target MSM Model

The target MSM model is composed of the following spheres locations and radii.

Sphere X Pos [m]	Sphere Y Pos [m]	Sphere Z Pos [m]	Sphere Radius [m]
-1.017	-1.333	-2.000	0.520
-4.067	0.667	-2.000	0.520
-4.067	-1.333	-2.000	0.520
-5.083	-0.667	-2.000	0.520
-2.033	-0.667	-2.000	0.520
-1.017	0.667	-2.000	0.520
-5.083	1.333	-2.000	0.520
-2.033	1.333	-2.000	0.520
-0.000	-1.333	-1.333	0.416
-0.000	-0.667	-0.667	0.416
-0.000	-1.333	0.667	0.416
0.000	0.667	0.667	0.416
-0.000	-0.667	1.333	0.416
0.000	0.667	-1.333	0.416
0.000	1.333	1.333	0.416
0.000	1.333	-0.667	0.416
-6.100	-1.333	-1.333	0.416
-6.100	-0.667	-0.667	0.416
-6.100	-1.333	0.667	0.416
-6.100	0.667	0.667	0.416
-6.100	-0.667	1.333	0.416
-6.100	0.667	-1.333	0.416
-6.100	1.333	1.333	0.416

-6.100	1.333	-0.667	0.416
-1.017	-2.000	-1.333	0.520
-2.033	-2.000	-0.667	0.520
-1.017	-2.000	0.667	0.520
-4.067	-2.000	0.667	0.520
-2.033	-2.000	1.333	0.520
-4.067	-2.000	-1.333	0.520
-5.083	-2.000	1.333	0.520
-5.083	-2.000	-0.667	0.520
-1.017	2.000	-1.333	0.520
-2.033	2.000	-0.667	0.520
-1.017	2.000	0.667	0.520
-4.067	2.000	0.667	0.520
-2.033	2.000	1.333	0.520
-4.067	2.000	-1.333	0.520
-5.083	2.000	1.333	0.520
-5.083	2.000	-0.667	0.520
-1.017	-1.333	2.000	0.520
-4.067	0.667	2.000	0.520
-4.067	-1.333	2.000	0.520
-5.083	-0.667	2.000	0.520
-2.033	-0.667	2.000	0.520
-1.017	0.667	2.000	0.520
-5.083	1.333	2.000	0.520
-2.033	1.333	2.000	0.520
-1.500	0.278	9.667	0.429
-1.500	0.278	12.167	0.429

-1.500	-0.278	6.333	0.429
-1.500	-0.278	3.833	0.429
-1.500	1.389	11.333	0.429
-1.500	-1.944	3.833	0.429
-1.500	-1.944	6.333	0.429
-1.500	-0.278	8.833	0.429
-1.500	0.278	7.167	0.429
-1.500	-1.944	8.833	0.429
-1.500	-1.389	9.667	0.429
-1.500	-1.944	11.333	0.429
-1.500	-0.278	11.333	0.429
-1.500	-1.389	12.167	0.429
-1.500	1.944	7.167	0.429
-1.500	1.389	8.833	0.429
-1.500	1.944	9.667	0.429
-1.500	1.944	12.167	0.429
-1.500	-1.389	7.167	0.429
-1.500	-1.389	4.667	0.429
-1.500	0.278	4.667	0.429
-1.500	1.389	3.833	0.429
-1.500	1.389	6.333	0.429
-1.500	1.944	4.667	0.429
-0.000	-11.167	0.167	0.277
-0.000	-10.333	0.333	0.277
-0.000	-8.667	0.167	0.277
-0.000	-7.833	0.333	0.277
-0.000	-6.167	0.167	0.277

-0.000	-5.333	0.333	0.277
-0.000	-3.667	0.167	0.277
-0.000	-2.833	0.333	0.277